Template-assisted growth and characterization of ZnO-based nanowire arrays and 3D networks

Application of nanowire networks for photoelectrochemical water splitting

Templat-gestütztes Wachstum und Charakterisierung von ZnO-basierten Nanodrahtarrays und 3D Netzwerken

Zur Erlangung des Grades eines Doktors der Naturwissenschaften (Dr. rer. nat.) genehmigte Dissertation von **M.Sc. Liana Movsesyan** aus Jerewan (Armenien)

Tag der Einreichung: 19.07.2016, Tag der Prüfung: 06.10.2016

1. Gutachten: Prof. Dr. Christina Trautmann
2. Gutachten: Prof. Dr. Wolfram Jaegermann

Material- und Geowissenschaften, D17

Darmstadt - 2017

TECHNISCHE UNIVERSITÄT DARMSTADT

MATERIAL-WISSENSCHAFT

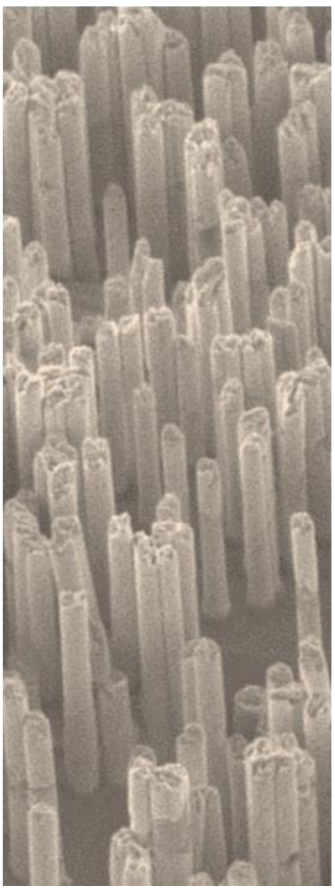

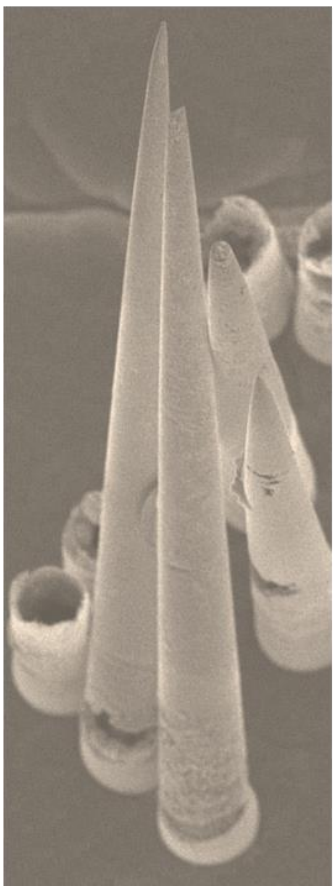

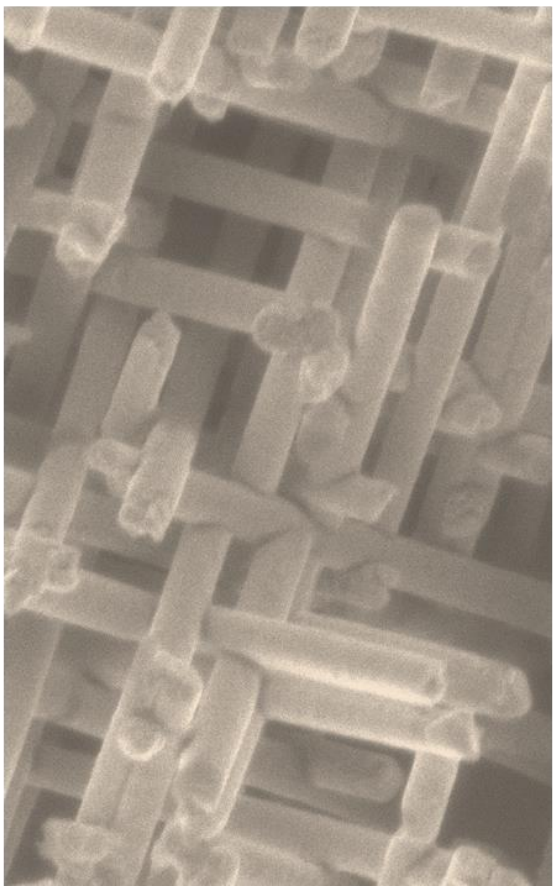

Template-assisted growth and characterization of ZnO-based nanowire arrays and 3D networks

Application of nanowire networks for photoelectrochemical water splitting

Liana Movsesyan

2016

Template-assisted growth and characterization of ZnO-based nanowire arrays and 3D networks: application of nanowire networks for photoelectrochemical water splitting

Templat-gestütztes Wachstum und Charakterisierung von ZnO-basierten Nanodrahtarrays und 3D Netzwerken: Anwendung der Nanodrahtnetzwerke für photoelektrochemische Wasserspaltung

Genehmigte Dissertation von M.Sc. Liana Movsesyan aus Jerewan (Armenien)

1. Gutachten: Prof. Dr. Christina Trautmann

2. Gutachten: Prof. Dr. Wolfram Jaegermann

Tag der Einreichung: 19. Juli 2016

Tag der Prüfung: 06. Oktober 2016

Darmstadt - D17

Erklärung zur Dissertation

Hiermit versichere ich, Liana Movsesyan, die vorliegende Dissertation ohne Hilfe Dritter und nur mit den angegebenen Quellen und Hilfsmitteln angefertigt zu haben. Alle Stellen, die aus den Quellen entnommen wurden, sind als solche kenntlich gemacht. Diese Arbeit hat in dieser oder ähnlicher Form noch keiner Prüfungsbehörde vorgelegen.

Datum: 19.07.2016 Unterschrift:

I herewith formally declare that I have written the submitted thesis independently. I did not use any outside support except for the quoted literature and other sources mentioned in the paper. I clearly marked and separately listed all of the literature and all of the other sources which I employed when producing this academic work, either literally or in content. This thesis has not been handed in or published before in the same or similar form.
In the submitted thesis the written copies and the electronic version are identical in content.

Date: 19.07.2016 Signature:

The work presented in this thesis has been conducted at the Materials Research group of the GSI Helmholtz Center for Heavy Ion Research and was sponsored by the scholarship program from Beilstein Institute for the Advancement of Chemical Sciences (Frankfurt), DFG-FOR 1583 and DFG SPP 1613 projects.

“We are visitors on this planet. We are here for one hundred years at the very most. During that period we must try to do something good, something useful with our lives. If you contribute to other people's happiness, you will find the true meaning of life.”

Dalai Lama XIV

Ես իմ դոկտորական աշխատանքը նվիրում եմ իմ ընկերներին և բոլոր այն զինվորներին, ովքեր ամուր կանգնած են դիրքերում և պաշտպանում են ընտանիքս ու իմ տունը՝ Հայաստանն ու Լեռնային Ղարաբաղը: Փա՛ռք ու պատիվ ձեզ:

Table of Contents

Abstract

In recent years, research on the fabrication of semiconductor nanowires has attracted increasing interest in various fields of research. Especially, the successful synthesis of ZnO micro- and nanoscale structures has paved the way to numerous applications for devices including nanogenerators, sensors, solar and fuel cells.

This work focuses on the synthesis of ZnO nanowire arrays and nanowire networks by means of electrochemical deposition in etched ion-track membranes. Three different geometries of nanowire-based structures are discussed: arrays of vertically aligned (1) cylindrical ZnO nanowires and (2) ZnO nanocones as well as (3) mechanically stable three-dimensional (3D) ZnO and ZnO/TiO_2 nanowire networks.

To establish a reproducible growth process of ZnO in track-etched membranes, the electrodeposition parameters of vertically aligned cylindrical ZnO nanowires are adjusted by independently varying the applied potential during the electrodeposition, the pore diameter of the membranes, and the concentration of the electrolyte ($Zn(NO_3)_2 \cdot 6H_2O$). The influence of these parameters on the morphological and crystallographic properties of the nanowires is analysed by means of high resolution scanning electron microscopy (HRSEM) and X-ray diffraction (XRD). ZnO nanocone arrays with µm-size bases and nm-size tips are fabricated applying two growth approaches: base-to-tip and tip-to-base. The arrays are analysed by SEM in terms of mechanical stability.

An important part of this thesis is the design and synthesis of 3D ZnO nanowire networks. The number density and diameter of the nanowires in the network are optimized in order to obtain mechanically stable 3D building blocks exhibiting a high surface area. The crystallographic properties are studied by XRD, high resolution transmission electron microscopy (HRTEM), selected area electron diffraction (SAED), and high-angle annular dark-field (HAADF) imaging. Knowledge drawn from these investigations is crucial for the implementation of these 3D nanoarchitectures into devices, including photodiodes and -electrodes.

Furthermore, the durability of ZnO-based nanowire networks in aqueous environment under applied potential and illumination is tested. In particular, they are employed as photoanode model systems for photoelectrochemical water splitting. The measurements are performed on pure ZnO and core/shell ZnO/TiO_2 nanowire networks and compared to those of their film counterparts. The role of the TiO_2 layer as a protection layer against photo(electro)chemical corrosion of ZnO as well as the efficient charge separation and transport from nanowires to the electrolyte is highlighted.

By using X-ray photoelectron spectroscopy (XPS) the contamination and chemical composition on the surface of the networks are quantified before and after photoelectrochemical measurements. Additionally, the Schottky barrier heights formed at the

ZnO-Au and TiO_2-Au contacts are theoretically determined from the values of the work function and the valence band position.

The work presented in this thesis shows how the outstanding flexibility of the ion-track technology combined with electrochemical deposition leads to new options for fabrication of complex ZnO-based nanowire structures. The possibility to tune the length, diameter and orientation allows the production of free-standing, high aspect ratio structures which are promising for a wide range of applications, including energy conversion and storage.

Zusammenfassung

In den letzten Jahren hat die Herstellung von Halbleiter-Nanodrähten zunehmendes Interesse in verschiedenen Forschungsgebieten geweckt. Insbesondere eröffnet die erfolgreiche Synthese von ZnO Mikro- und Nanostrukturen eine Vielzahl von Anwendungen, wie z.B. Nanogeneratoren, Sensoren, Solar- und Brennstoffzellen.

Die vorliegende Arbeit konzentriert sich auf die Synthese von ZnO Nanodrahtarrays und Nanodrahtnetzwerken mittels elektrochemischer Abscheidung in geätzten Ionenspurmembranen. Drei verschiedene Geometrien von Nanodraht-basierten Strukturen wurden abgeschieden und analysiert: vertikal ausgerichtete Arrays von (1) zylindrischen und (2) konischen ZnO Nanodrähten sowie (3) mechanisch stabile dreidimensionale (3D) ZnO und ZnO/TiO_2 Nanodrahtnetzwerke.

Um einen reproduzierbaren Wachstumsprozess von ZnO in Ionenspurmembranen zu erzielen, wurden die Abscheideparameter für vertikal ausgerichtete zylindrische ZnO-Nanodrähte sowie die angelegte Spannung, der Durchmesser der Poren in den Membranen, und die Konzentration des Elektrolyten ($Zn(NO_3)_2 \cdot 6H_2O$) unabhängig voneinander variiert. Der Einfluss dieser Parameter auf die morphologischen und kristallographischen Eigenschaften der Nanodrähte wurde mittels hochauflösender Rasterelektronenmikroskopie (HRSEM) und Röntgenbeugung (XRD) analysiert. Konische ZnO Nanodrahtarrays mit µm breiten Basen und nm großen Spitzen wurden mit zwei verschiedenen Wachstumsmethoden hergestellt: von der „Basis zur Spitze“ und umgekehrt von der „Spitze zur Basis“. Die Arrays wurden mit Hilfe von Rasterelektronenmikroskopie hinsichtlich ihrer mechanischen Stabilität untersucht.

Ein wichtiger Teil dieser Arbeit ist die Entwicklung und Synthese von 3D ZnO Nanodrahtnetzwerken. Die Anzahl und der Durchmesser dieser Nanodrähte wurden optimiert, um mechanisch stabile 3D Strukturen mit hoher Oberfläche zu erhalten. Die Kristallstruktur wurde mittels XRD, hochauflösender Transmissionselektronenmikroskopie (HRTEM), Feinbereichsbeugung (SAED) und Ringdunkelfeldabbildung (HAADF) untersucht. Die hierdurch erhaltenen Erkenntnisse sind wichtig für die Implementierung dieser 3D Nanoarchitekturen in komplexere Bauteile wie z.B. Photodioden und -elektroden.

Die Lebensdauer von ZnO-basierten Nanodrahtnetzwerken in wässriger Umgebung wurde bei angelegter Spannung und unter künstlichem Sonnenlicht (Solarsimulator, AM 1.5) getestet. Die Netzwerke dienten als Modellsystem für Photoanoden zur photoelektrochemischen Wasserspaltung. Die Messungen wurden für reine ZnO und Core/Shell ZnO/TiO_2 Nanodrahtnetzwerke durchgeführt und mit den entsprechenden Filmen verglichen. Die Rolle der TiO_2 Schicht als Schutzschicht gegen photo(elektro)chemische Korrosion von ZnO sowie für eine effiziente Ladungstrennung und -transport aus den Nanodrähten zum Elektrolyten wird erörtert.

Mittels Röntgenphotoelektronenspektroskopie (XPS) wird die Kontaminationen und die chemische Zusammensetzung der Oberfläche der Nanodrahtnetzwerke vor und nach photoelektrochemischen Messungen quantifiziert. Zusätzlich werden die Höhen der Schottkybarriere an den ZnO-Au und TiO_2-Au Kontakten aus den Werten der Austrittsarbeit und Valenzbandposition theoretisch bestimmt.

Die durchgeführten Arbeiten zeigen, wie die große Flexibilität der Ionenspurtechnologie in Verbindung mit elektrochemischer Abscheidung zu neuen Verfahren zur Herstellung komplexer ZnO-basierter Nanodrahtsysteme führen kann. Die Möglichkeit die Länge, den Durchmesser und die Orientierung dieser Nanodrähte frei wählen zu können, erlaubt die Herstellung freistehender Strukturen mit hohem Aspektverhältnis, die für ein breites Spektrum von Anwendungen, wie z.B. für Energieumwandlung und -speicherung, geeignet sind.

Introduction

Nanoscale engineering is one of the most prominent and actual research topics nowadays. The demand for more advanced and next-generation devices leads to extensive research effort in nanoscale technology. For miniaturization and increasing of the device efficiency, one-dimensional nanowires are of great interest. In particular, nanowires are excellent model systems for the investigation of size and geometry effects on physical characteristics such as optical,[1–6] electrical,[7–10] magnetic,[11–14] electronic,[15–17] and thermal[18–20] properties. In addition, the integration of nanowires into micro- and macro-devices requires the development of strategies to assemble them into three-dimensional (3D) building blocks with enhanced mechanical stability, flexibility and high surface area.

ZnO micro- and nanoscale structures have attracted tremendous interest for numerous applications. Studies on ZnO nanostructures are motivated by the technologically relevant properties of ZnO including transparency, piezoelectricity, natural n-type conductivity, high thermal stability, high electron mobility (>1000 $cm^2/(V \cdot s)$), a wide and direct band gap of 3.3-3.6 eV, as well as a large exciton binding energy of 60 meV.[21,22] Additional advantages of ZnO include its non-toxicity as bulk material, low cost, and the wide availability on the earth. These properties make ZnO nanowires promising for the integration in a wide range of devices including transistors,[23] sensors,[24,25] nanogenerators, piezoelectric devices,[26] solar cells,[23,27,28] and photoelectrodes for water splitting when protected and/or integrated in tandem cells.[29,30] The application of ZnO in photodetectors, light-emitting diodes, and laser diodes that operate in the blue and ultraviolet region of the light spectrum are also being studied.[31–33] ZnO nanowires embedded in membranes may for example serve as X-ray detectors.[34]

ZnO nanostructures are fabricated by top-down methods including electron beam and optical lithography,[35,36] as well as by bottom-up methods such as sol-gel synthesis,[37] metal organic chemical vapor deposition,[38] and electrodeposition from a seed layer.[39] However, a large scale production of ZnO wires with these techniques is limited by several factors, including time and cost efficiency or control and tuning of nanowire size and geometry. Template-assisted electrodeposition combines both approaches, top-down and bottom-up, and enables the synthesis of nanowires with simultaneous and precise control over length, diameter, and composition.[40–43] The template method has demonstrated to be very suitable for the fabrication of metal and semimetal nanostructures with tuned size and crystallinity. By adjusting the growth parameters Toimil-Molares *et al.* showed that it is possible to grow both single and polycrystalline Cu nanowires inside polycarbonate etched ion-track membranes.[44] Pan *et al.* reported the synthesis of single crystalline Ni and Co nanowires in anodic aluminum oxide (AAO) templates.[45] However, reports on the electrodeposition of semiconductor nanowires in polymer templates are rather limited, in particular for ZnO. Sima *et al.* reported the electrodeposition of ZnO nanowires in polymer membranes with large pores of few hundred nm diameter using a $Zn(NO_3)_2$-based electrolyte.[46] Lincot *et al.* studied

the electrochemical growth of ZnO nanowires from $Zn(ClO_4)_2$ electrolyte in AAO templates and compared the results to the growth of pure Zn nanowires.[47] The influence of the applied potential during pulsed electrodeposition on the morphology and crystallographic properties of ZnO films was studied by Manzano *et al.*[48] However, the influence of the potentiostatic deposition conditions on the structure and morphology of ZnO nanowires with various diameters, as reported in this thesis, has not been discussed before. This study is important in order to understand relevant properties such as electrical resistivity, charge carrier generation and transport, and photoluminescence of the wires, which play an important role in the efficiency of ZnO nanowire-based devices.

To date, the synthesis of nanowire- and nanorod-based 3D architectures continues being a challenge. The synthesis of tungsten oxide nanowire networks using a thermal evaporation approach was reported by Zhou *et al.*[49] and Ponzoni *et al.*[50] The growth of nanowires along six crystallographically equivalent directions resulted in the intersection of rectangular nanowires and the formation of a network with a junction angle of nearly 90˚. These structures showed good crystallinity, however the width of the wires was not controlled, ranging from several tens of nm to 200 nm. Moreover, the size of networks as a continuous system is only 1-10 µm. Wang *et al.* reported the synthesis of ZnO interconnected networks by a high temperature solid-vapor deposition process.[51] The network consisted of nanorods and nanowires with diameters of 20-100 nm. These mesh-like structures have a uniform height of 15-20 µm, however they exhibit an inhomogeneous distribution over the substrate. The main drawbacks of this technique are the limited and non-controlled interconnectivity between adjacent nanowires, the large diameter distribution, and the limited height up to 30 µm. Moreover, only a few compounds are endowed with an ability to self-organize in 3D building blocks.

These limitations and challenges can be circumvented by using template-based growth with pre-designed templates, including mesoporous silica, anodic alumina and track-etched polymer membranes. Lu *et al.* performed electrodeposition of different metal and semiconductor networks in 3D mesoporous silica templates.[52] The diameters of the network ligaments ranged from 2 to 20 nm. However, with this technique it is challenging to obtain large scale networks with well-controlled porosity and heights thicker than several microns. A successful fabrication of ordered 3D interconnected nanoarchitectures in anodic porous alumina was achieved by Martin *et al.*[53] These templates are prepared by a two-step anodization process and consist of well-defined nanotubular network in the sub-100 nm range. Although the position and amount of junctions can be precisely adjusted by the anodization parameters, the angle between the pores at the junctions is fixed to 90˚, and no optimization for this parameter has been reported yet. Additionally, a pore-widening is observed in these networks, which still needs to undergo optimization in order to obtain networks with monodisperse pore diameters.

Among the template-based techniques for fabrication of hierarchal structures, ion-track technology is very attractive because it allows for easy tuning the height (up to 100 μm) and area (up to ~20 cm^2 large) of the network, the diameter (20 to few hundreds of nm), number density (up to 10^{10} cm^2) and interconnectivity of the pores in the template as well as the angle between interconnected pores. 3D structured templates based on irradiation performed at the GSI Helmholtz Center for Heavy Ion Research have been successfully used for electrochemical deposition of Pt,[54] ZnO,[55] and Sb[56] nanowire networks, electroless plating of Au, Ni, Cu, Pt and Ag[57] and atomic layer deposition of Al_2O_3, SiO_2 and TiO_2 [58] nanotube networks as well as Pt, Cu and Ag superstructures consisting of interconnected nano- and microscale pores.[59] The compact design, mechanical stability and high surface area of these nanowire-based 3D hierarchical systems can be advantageous for example to facilitate efficient light absorption and charge carrier transport in photoelectrodes[30,60–63] and optical elements,[64,65] to enhance the performance of gas sensors,[50,66] batteries[67,68] and supercapacitors[69] or to achieve high electric field confinement and enhancement in 3D plasmonic hollow nanocavities,[70] as well as for computer and chip technologies.[71]

This thesis focuses on the synthesis and characterization of ZnO nanowire-based structures applying ion-track technology in combination with electrochemical deposition. The overall goal of this work has been to optimize ion irradiation, etching and electrodeposition parameters to achieve a reproducible and controlled growth of ZnO nanostructures. Detailed analysis of the shape, size, morphology and crystallinity of the wires is of prime importance for applications.

Three different geometries are studied, namely arrays of vertically aligned cylindrical nanowires and nanocones as well as nanowire networks. It is shown that applying a low concentration of the electrolyte leads to the growth of nanowires with a smooth surface. By varying the applied potential of the electrodeposition, the texture of ZnO wires changes. Also, the nanopore diameter is found to be a tool to vary the preferred orientation of the wires. The mechanical stability of cylindrical nanowire arrays after dissolution of the polymer is studied by altering the aspect ratio (length to diameter ratio) of the wires. Membranes with conical pores are employed as templates for the electrodeposition of conical ZnO wires. Two growth approaches are discussed, base-to-tip and tip-to-base. In both cases, the arrays are polycrystalline, but the morphology changes significantly depending on the growth direction.

ZnO nanowire networks with different nanowire diameters and number densities are synthesised, and these parameters are optimized to obtain reproducible, free-standing and stable structures. The growth homogeneity of these networks is improved by adding one more irradiation step to the standard network irradiation process and applying a mask with a pre-defined area. Additionally, photoelectrochemical performance of bare ZnO and core/shell ZnO/TiO_2 nanowire networks is tested and compared to their film counterparts, resulting in higher photocurrents for the network structures. The surface imaging before and after

photoelectrochemical measurements shows that the TiO_2 layer protects the ZnO network from corrosion and morphological changes.

The thesis is composed of six chapters. **Chapter 1** describes the theoretical background and working principle of the techniques used for this thesis as well as the characteristic parameters of ZnO relevant for the explanation of the results. **Chapter 2** introduces the methods of characterization and the measurement tools. **Chapter 3** depicts the preparation processes of membranes with vertically aligned cylindrical and conical channels as well as networks of interconnected nanochannels. The main results of the synthesis, growth optimization and characterization of ZnO cylindrical and conical wire arrays as well as nanowire networks are presented in **Chapter 4**. The characterization of crystallinity and composition of pure ZnO and ALD-coated ZnO/TiO_2 core/shell nanowires and networks is presented in **Chapter 5**. Lastly, **Chapter 6** sheds light on the photoelectrochemical measurements performed with bare ZnO and core/shell ZnO/TiO_2 nanowire networks in order to test their reliability and stability for future applications. The morphology and composition of their surface before and after the measurements is discussed.

1. Theoretical background

This chapter introduces the concepts of the ion-track technology and electrochemical deposition in polymeric membranes. The main properties of ZnO, relevant for this thesis, are elucidated. The working principle of photoelectrochemical water splitting and metal-semiconductor contacts are described.

1. Theoretical background

1.1. Ion-track technology

When passing through matter, heavy ions dissipate their energy mainly because of elastic and inelastic coulomb interactions with the atoms of the material. If the ion velocity is below 0.01 MeV per nucleon (MeV/u), elastic collisions (nuclear energy loss) dominate whereas at higher ion velocities the interaction is influenced by inelastic collisions that lead to ionization and electronic excitation processes (electronic energy loss). For the fabrication of ion-track membranes swift heavy ions of several MeV/u were used. Thus the energy loss per unit path length (dE/dx) is based on electronic stopping. The energy loss is related to the charge of the ion projectile and is described by the Bethe-Bloch formula:[72]

$$-\left(\frac{dE}{dx}\right)_e = \frac{4\pi n_e Z_t Z_p^2 e^4}{m_e v^2}\left(ln\frac{2m_e v^2}{I(1-\beta^2)} - \beta^2 - \delta - U\right), \quad (1)$$

where m_e is the mass of the electron, v is the velocity of the ion, $\beta = v/c$ (c is the speed of light), Z_p is the charge state of the ion, n_e is the number density of the electrons in the material, Z_t is the atomic number of the target material, and I is the mean ionization potential of atoms in the target medium, through which the particle is passing. δ and U are correction factors, which take relativistic effects into account. The main conclusions arising from the Bethe-Bloch formula are the following: the energy loss (also called stopping power) depends on the charge of the ion, the electron density in the material, and it is a function of the ion velocity, $dE/dx \sim n_e Z_p^2 f(\beta)$. In the case when stopping of the ions in the material is mainly derived from inelastic collisions, nuclear stopping is often ignored. The energy loss of Bi ions in polycarbonate as a function of the ion energy per nucleon calculated by means of the SRIM-2003 code (**S**topping and **R**ange of **I**ons in **M**atter) is shown in Figure 1a in a double logarithmic scale. The dashed green and red curves correspond to the electronic and nuclear energy losses, respectively, and the solid blue curve represents the total energy loss.

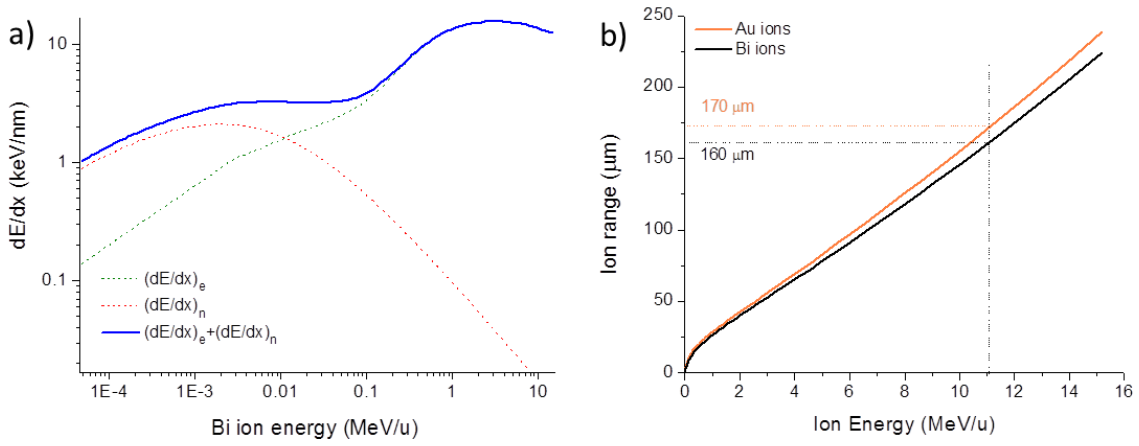

Figure 1: a) Energy loss of Bi ions and b) range of Au (orange) and Bi (black) ions in polycarbonate as a function of the specific ion energy according to the SRIM-2003 code simulation.

The complete penetration depth (R_p) of the ion with initial energy E_0 can be determined from the following expression:[73]

$$R_p = \int_{E_0}^{0} \left(\frac{dE}{dx}\right)^{-1} dE, \text{ with } \left(\frac{dE}{dx}\right) = \left(\frac{dE}{dx}\right)_e + \left(\frac{dE}{dx}\right)_n, \quad (2)$$

where $(dE/dx)_e$ and $(dE/dx)_n$ are the electronic and nuclear energy losses per unit path length, respectively. The range of Au and Bi ions (which were used in this work) in polycarbonate foils calculated using the SRIM-2003 code is presented in Figure 1b. The dashed lines correspond to the values of penetration range and energy of Bi (black) and Au (orange) ions, being 160 and 170 µm for Bi and Au ions with an energy of 11.1 MeV/u, respectively. Considering the penetration range of the ion, polymer foils which have thicknesses of few tens µm can be assembled in stacks so that several foils are irradiated in one step.

Depending on the ion energy and the charge state, the ion energy loss produces structural defects and compositional variations in the polymer. The radiation damage formed along the trajectory of each incident ion is called latent track. Tracks have commonly a cylindrical geometry and a diameter between 5 and 10 nm depending on ion energy loss and target material. In polymers, the energy loss of heavy ions leads to breakage of the chemical bonds, amorphization and outgassing of small volatile fragments.[74,75]

Schematic representation of the irradiation process is shown in Figure 2. The swift heavy ions used for irradiation at the UNILAC provide highly aligned parallel tracks. The beam incidence can be varied from normal to the sample surface down to grazing angles. In contrast to commercial ion-track membranes, those fabricated at the GSI are characterized by a very small angular spread.

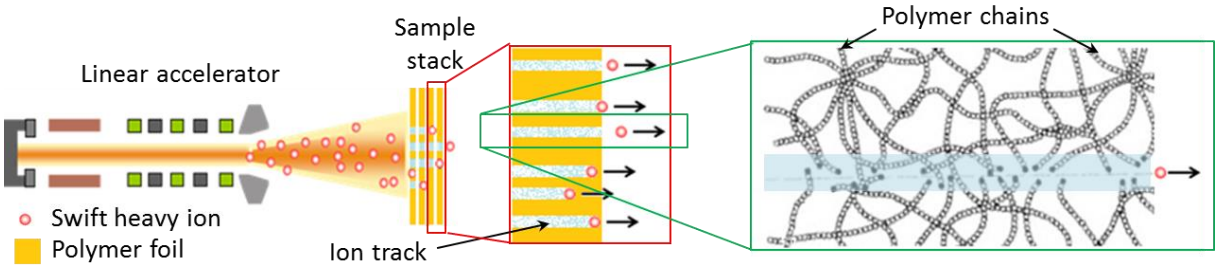

Figure 2: Schematic representation of the linear accelerator (UNILAC) at the GSI and the irradiation process of a stack of polymer foils under normal incidence. The zoomed-in images show schematically a single track consisting of broken bonds of polymer chains (adapted from [43,72]).

By means of chemical etching, the irradiated foils are converted to porous membranes by selectively removing the damaged material and thereby converting each ion track into an individual open pore. Since each ion creates one track, the number of the pores in the membrane is equal to the ion fluence (number of ions per cm^2). The size and homogeneity of the etched pores depend on the properties of the target material (e.g. density, composition, crystallinity), the energy loss of the ions, the etching time and etching solution. In addition, to

obtain pores with uniform diameter and well defined shape, the etching rate along the damaged ion track (v_t) should be much higher than the isotropic etching rate of the non-damaged bulk material (v_b). The v_t: v_b ratio will determine the opening angle of the pore.[76–78] If $v_t >> v_b$, the resulting pores have a cylindrical shape, whereas conical pores are achieved in the case of a smaller etching rate ratio. The fabrication processes of membranes with parallel cylindrical and conical pores as well as with interconnected nanopore networks are described in detail in Chapter 3. It is important to mention that, prior to etching, both sides of all irradiated polymer foils used for experiments in this thesis were exposed to UV light in air. It is known, that UV irradiation modifies the chain compounds inside the track without significant effects on the virgin PC thus improving the diffusion of the etching solution along the track. Besides, it triggers creation of new chain ends and acidic compounds which are highly sensitive to etchant. As a result, UV treatment affects the etching rate and improves its selectivity and the monodispersity of the nanopores.[79,80,81]

1.2. Electrodeposition

The template method, and in particular electrodeposition in etched ion-track membranes, combines both top-down and bottom-up approaches and has demonstrated to be a very appropriate technique for the growth of nanostructures with small size and high surface-to-volume ratio.[20,22] It enables the synthesis of nanowires and nanotubes with simultaneous and excellent control over length and diameter. The template method has demonstrated to be very suitable for the fabrication of metal and semimetal nanostructures with tuned size, composition, and crystallinity.[21,23] Besides continuous single component wires, also segmented as well as multicomponent[23,82] and alloy[83,84] structures can be fabricated.

Electrodeposition of micro- and nanowires is carried out using electrochemical cells consisting of two or three electrodes which are connected to a potentiostat for controlling and measuring the current and potential. The setup can be operated either in potentiostatic (constant applied potential) or galvanostatic (constant applied current) mode, as well as in pulsed electrodeposition conditions (pulsed applied potential). In this work, potentiostatic growth in a three-electrode configuration is applied. This method allows for a precise control of the composition of the deposit not only for one but also for multicomponent materials with a chosen stoichiometry.[84]

The thermodynamic potential needed for the electrochemical reactions is determined by the Nernst equation, which describes the redox potential E_{redox} of a redox couple by the following equation:[85]

$$E_{redox} = E_0 + \frac{RT}{zF} \ln \frac{a_{ox}}{a_{red}}, \tag{3}$$

where E_0 is the standard electrode potential of the redox couple with respect to the normal hydrogen electrode (NHE), and a_{ox} and a_{red} are the activities of the oxidized and reduced

species, respectively. R is the gas constant (8.3145 J/mol·K), T is the temperature, z is the number of electrons involved in the reaction, and F is the Faraday constant (96485 C/mol). Thermodynamically, when the potential applied to the working electrode is more negative than E_{redox} (in case of reduction), electrodeposition takes place and the ions in the electrolyte are reduced and may form a solid material on the working electrode.

In the simplest case of metals, electrodeposition is a process of reducing metal ions from an aqueous solution upon application of a potential. When the current flows from the counter electrode to the working electrode, the metal ions (M^{n+}) in the electrolyte that travel to the working electrode are reduced on the metallic substrate by capturing electrons. The corresponding reaction that takes place is as follows:[85]

$$M^{n+} + ne^{-} \rightarrow M_{solid}, \tag{4}$$

The schematic of the electrochemical cell with the three electrode (working, counter and reference electrodes) connected to the potentiostat is shown in Figure 3. The membrane with sputtered and electrodeposited metallic layers on one side always acted as a working electrode, which was in contact with the copper ring of the cell. As counter electrode a platinum wire and as reference electrode a Ag/AgCl (sat. KCl) were used. In this setup, the potential is applied to the working electrode with respect to the reference electrode. The fixed potential of the Ag/AgCl reference electrode (0.197 V vs. the standard hydrogen electrode at 25˚C)[86] allows reproducibility for all experiments.

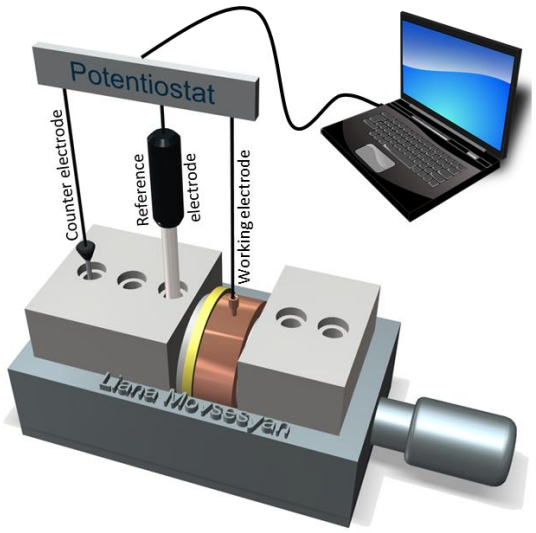

Figure 3: Schematic of electrochemical cell for nanowire growth by using three electrodes (working, counter, and reference) connected to a potentiostat, which is controlled via computer. The metallic layer sputtered and electrodeposited on one side of the membrane served as a working electrode.

The growth process was monitored and controlled by recording chronoamperometric (current vs. time) curves during electrodeposition, which enabled us to monitor the different growth steps during the synthesis process (Figure 4).

The charge and mass transfer of the deposited material are quantified with Faraday's law, which states that the mass (m) of the deposited material is directly proportional to the total amount of transferred charge:

$$m = \frac{M}{z \cdot F} \int_{t_0}^{t_n} I dt = \frac{M}{z \cdot F} \cdot Q, \tag{5}$$

where I is the current passing through the circuit during the time period between t_0 and t_n, M and z are the molar mass and valence of the deposited atoms, respectively, and F is Faraday constant. With this formula, the amount of deposited material can be calculated from the I-t curves recorded during electrodeposition process. Figure 4 presents a typical chronoamperometric curve for electrodeposition of ZnO in the cylindrical channels of a polycarbonate membrane with an average pore diameter of 250 nm and density of 10^9 pores/cm^2.

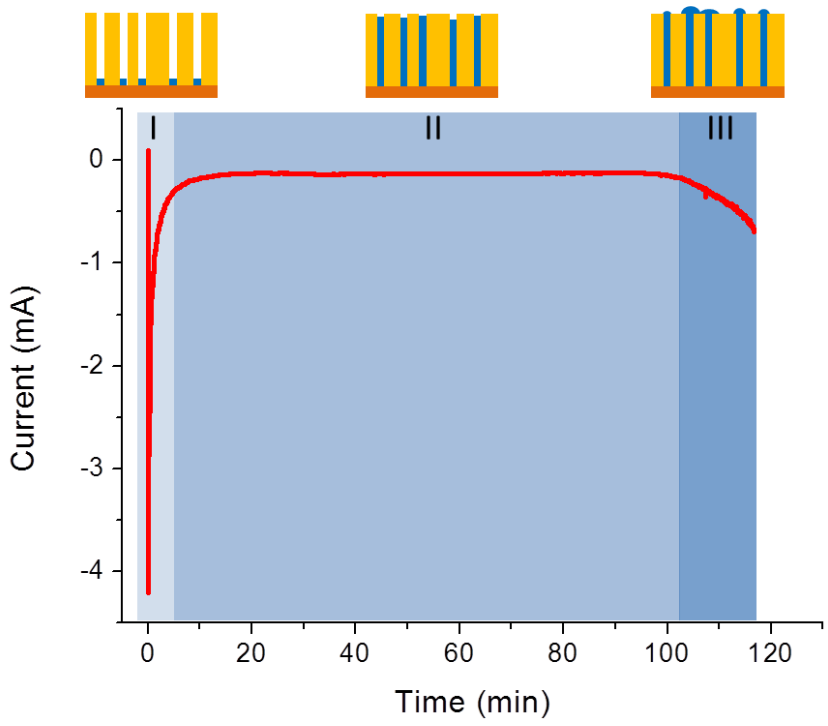

Figure 4: Representative chronoamperometric curve recorded during electrodeposition of ZnO nanowires, showing the dependence of the deposition current with respect to the time, and schematics of three regimes of nanowire growth.

At the beginning of the deposition process (region I), the current rapidly increases (in absolute value) and then decreases during the following few minutes. This effect is attributed to the charging of the double layer (Helmholtz plane) and formation of the diffusion layer, as well as to nucleation processes. As the growth of nanowires inside the membrane is continues (region II), the current remains almost constant. Finally, when the pores are completely filled, so called caps start to grow on top of the wires expanding on the surface of the membrane. Caps growth is indicated by an increase in current due to the increased effective area where the

growth takes place (region III).[87] By following this current behavior during nanowire growth, the deposition can be stopped at a defined time period, e.g. to obtain nanowires with desired length.

In the case of multicomponent materials, such as metal oxides, the growth takes place in more than one step depending on the electrolyte composition and pH. For the synthesis of metal oxides, electrodeposition from nitrate based solutions is one of the most common techniques. The driving force in this process is the nitrate reduction which leads to a local pH increase in the electrolyte due to formation of OH^- ions. In this work, an aqueous electrolyte of zinc nitrate hexahydrate ($Zn(NO_3)_2 \cdot 6H_2O$) was used for the growth of ZnO nanowires, which takes place in several steps. First, upon application of the potential, hydroxyl ions (OH^-) are formed at the cathode/electrolyte interface according to reaction 6. In the presence of Zn^{2+} ions in the solution hydroxylation reaction takes place forming $Zn(OH)_2$ (reaction 7). If the electrolyte is heated, at elevated temperature $Zn(OH)_2$ is dehydrated thus resulting in the formation of fully crystalline ZnO according to reaction 8. As mentioned before, the local pH in the bath close to the electrode as well as in the pores is increasing because of the formation of OH^- ions, leading to the preferential growth of ZnO inside the pores of the membrane. Depending on the ratio of the produced OH^- and Zn^{2+} ions and the supersaturation in the bath, the crystal growth will behave differently leading to different crystal orientations. Therefore, the crystallinity depends on the concentration of OH^- ions.[39,55,88]

$$NO_3^- + H_2O + 2e^- \rightarrow NO_2^- + 2OH^-, \quad (6)$$

$$2OH^- + Zn^{2+} \rightarrow Zn(OH)_2, \quad (7)$$

$$Zn(OH)_2 \xrightarrow{T\,^\circ C} ZnO + H_2O. \quad (8)$$

Previous studies reported the electrodeposition of ZnO nanostructures from $Zn(NO_3)_2 \cdot 6H_2O$ with pH values adjusted between 7 and 11 by adding NaOH to the electrolyte.[89–91] To avoid degradation of the polymer by high pH electrolytes during nanowire growth, an as-prepared electrolyte with pH 5 was used in this work. The growth process took place at 80˚C and 60˚C for parallel arrays and nanowire networks, respectively.

1.3. Structural and physical properties of ZnO

During the past few years, the research activities on zinc oxide (ZnO) have significantly increased. The history of the research on ZnO goes back to1930s reaching its peaks in the late 1960s due to the availability of single crystalline bulk ZnO produced by chemical vapor deposition (CVD).[92,93] Although ZnO is an “old” material, there are still numerous open questions about the structural and optical properties of this material. Particularly, nanoscale 1D structures, such as nanowires, nanobelts, nanoflowers, nanoribbons, nanorods, nanowalls, and nanotubes drastically attracted the attention of scientists due to their promising application in technology.[23]

1.3.1. Crystal structure

ZnO can crystallize in three possible polymorphs: wurtzite, rocksalt and zinc-blende. Thermodynamically, the most stable phase is the wurtzite crystal structure, where each Zn atom is surrounded by a tetrahedron of four oxygen atoms, and vice versa. The wurtzite structure has a hexagonal unit cell with two lattice constants a = 0.3249 nm and c = 0.52042 nm at ambient conditions, and belongs to the $P6_3mc$ space group.[94] The structure consists of interpenetrating hexagonal close-packed (hcp) bi-layers of zinc and oxygen displaced with respect to each other along the c-axis.[94] The schematic representation of the ZnO wurtzite lattice with the primitive cell is shown in Figure 5a. The crystallographic orientations of the a- and m-planes are highlighted in Figure 5b. The directions and planes for hexagonal structures are indexed either with three digit Miller indices (hkl) or four digit Bravais-Miller indices (hkil). For ZnO, it is more common to use the four axes a_1, a_2, a_3 and c, and therefore four indices, where h, k and i are related as follows: h+k = -i. This relation allows the transformation of Miller to Bravais-Miller indices, and vice versa. The c-axis is always referred to as the [0001] direction, and the planes perpendicular to this axis are the hexagonal (± 0001) planes. The latter are the most commonly observed facets and the main polar surface in wurtzite ZnO arising from the strong bond polarity of Zn^{2+} and O^{2-} ions, being either zinc or oxygen terminated. Other planes also often observed in wurtzite ZnO are $\{2\bar{1}\bar{1}0\}$ and $\{01\bar{1}0\}$, which are non-polar surfaces due to the equal amount of Zn and O.[23,27,94–96]

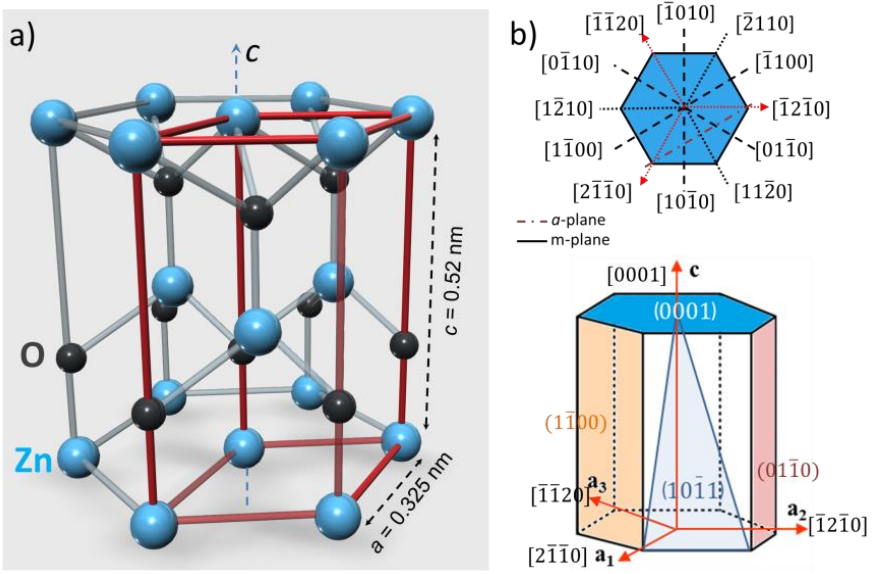

Figure 5: a) Schematic representation of the wurtzite ZnO structure with a primitive cell, b) crystallographic orientations of planes that are commonly present in the wurtzite phase.

1.3.2. Band structure

ZnO is a II-VI semiconductor with a wide band gap (E_g) of 3.37 ± 0.01 eV at room temperature, which is in the near UV-spectral range.[94] The first theoretical and experimental

studies of the electronic band structure of ZnO go back to the late 1960s and 1970s.[95,97,98] Energy bands of hexagonal ZnO are shown in Figure 6.[97] Both the valence band (VB) maximum and the conduction band (CB) minimum are positioned at the same Γ point with k = 0 wave vector, indicating that ZnO has a direct band gap. Several theoretical and experimental works have shown the presence of *d*-bands in ZnO at around 6 - 9 eV below the VB, which correspond to Zn*3d* orbitals. Due to the significant overlap of d orbitals, ZnO has broader *d* bands than any other II-VI compound.[97] The states closer to the VB maximum correspond to O*2p* orbitals, whereas the O*2s* bands are situated far below the VB (at ~ -20 eV). The CB is formed mainly by the empty Zn*4s* levels.[99,100] The bonds in wurtzite ZnO have sp^3 covalent nature.

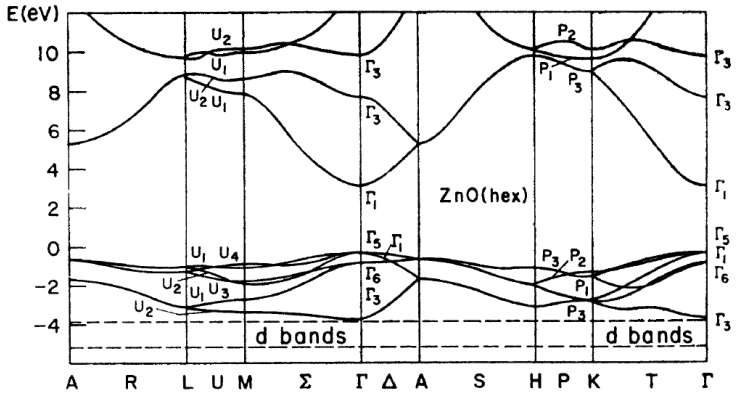

Figure 6: Energy band of hexagonal ZnO according to Rössler (1969).[97]

Among all II-VI compounds, ZnO has the largest excitation binding energy of 60 meV,[21,22] which makes ZnO a very interesting material for photonic devices due to its broad emission band.

1.3.3. Electrical properties

Both theoretical and experimental studies on the electrical properties of ZnO films and nanostructures have been reported since a few decades. Because of the oxygen vacancies in the structure, normally undoped ZnO has intrinsic n-type conductivity. The more oxygen vacancies are present, the higher is the electron density. As compared to other II-VI semiconductors, bulk ZnO has a very high electron mobility (~200 $cm^2V^{-1}s^{-1}$ at 300 K, ~2000 $cm^2V^{-1}s^{-1}$ at 50 K),[101] which is expected to improve the performance of electronic devices based on this material. A higher electron Hall mobility was reported in studies of ZnO/Mg:ZnO heterostuctures reaching up to 5500 $cm^2V^{-1}s^{-1}$.[102] For transparent conductive oxide devices, ZnO is often doped with group III metals like Al, Ga, and In, which enhances the n-type conductivity of ZnO.[103–105] For a long time, intensive efforts have been put in research on the synthesis of p-type ZnO, which is one of the main challenges of this material. p-ZnO is mainly obtained by doping with phosphorus[106] or nitrogen.[107,108] Despite the vast number of reports, the fabrication of p-type ZnO is hardly reproducible.

1.4. Photoelectrochemical water splitting

One of the most important but challenging technological issues of the century is the shift from fossil fuels to renewable energy sources, such as hydro- and wind power, solar energy, and biofuels. The main problems related to the use of fossil fuels such as coal, natural gas and oil products are the release of CO_2 gas to the atmosphere and the limited and quickly diminishing amount of fossil fuel sources on earth. Renewable energy sources have a great potential to substitute fossil fuels and serve as "infinite" and sustainable energy sources providing a clean environment. Large scale research has been performed and is ongoing worldwide in search of environmentally friendly energy sources. In 1883, the first solar cell based on selenium was made by Charles Fritts. However, this solar cell did not have a large scale use because of the sunlight to electricity conversion efficiency being less than one percent. In 1954, the first practical Si-based solar cell was demonstrated in the Bell laboratories by Daryl Chapin, Gerald Pearson and Calvin Fuller with an efficiency of about six percent. This was the highest reported value at that time. The efforts to produce photovoltaic devices with high efficiency still continue at present.

A new approach to obtain a clean, cost-efficient and domestically produced energy source was proposed by Akira Fujishima and Kenichi Honda in 1972.[109] They demonstrated the first successful experiment of light-assisted water splitting using an n-type TiO_2 photoanode connected with a platinum black electrode in a photoelectrochemical (PEC) cell for hydrogen production as a renewable energy source. Since then, many efforts have been devoted to this research field. More efficient water splitting systems have been obtained by combining several materials such as a tandem cell, adding co-catalysts, and applying different configurations of PEC cells.[110–113] Albeit increasing the efficiency of both photon-to-current conversion and generation and collection of hydrogen remain challenging, light-driven PEC water splitting for hydrogen production is one of the most promising and dominating fields of research today.

The principle of the PEC cell is based on the physics of semiconductor-light interaction. Important parameters to be considered during the choice of the materials are:

- the band gap of the semiconductor has to be small enough to absorb light in a relatively wide range of the solar spectrum,
- the position of the CB minimum and VB maximum with respect to the hydrogen and oxygen redox potentials for efficient hydrogen and oxygen evolution reaction (HER and OER, respectively): i.e. the CB minimum must be higher in energy than the standard redox potential of H^+/H_2 couple, and the VB maximum must be lower than the standard redox potential of the H_2O/O_2 couple,
- the stability against the (photo)electrochemical corrosion in aqueous electrolytes,

- efficient separation and transfer of minority charge carriers from the core of the photoelectrode to the semiconductor/electrolyte interface, and of the majority charge carriers to the counter electrode, with minimum recombination.

A vast variety of single-, bi- and multicomponent materials, such as ZnO, Al:ZnO, TiO_2, Cu_2O, Fe_2O_3, WO_3, GaP, GaN, Si, CdS, CdSe, $BiVO_4$, $NaTaO_3$:La and many others, have been studied.[114–118] The standard redox potential of the H_2O/O_2 couple is 1.23 V versus the reversible hydrogen electrode (RHE), which means that the band gap of the photoelectrode material must be larger than this thermodynamic minimum value of potential for splitting the water. The positions of several common semiconductors with respect to the redox potentials for water splitting are shown in Figure 7a.

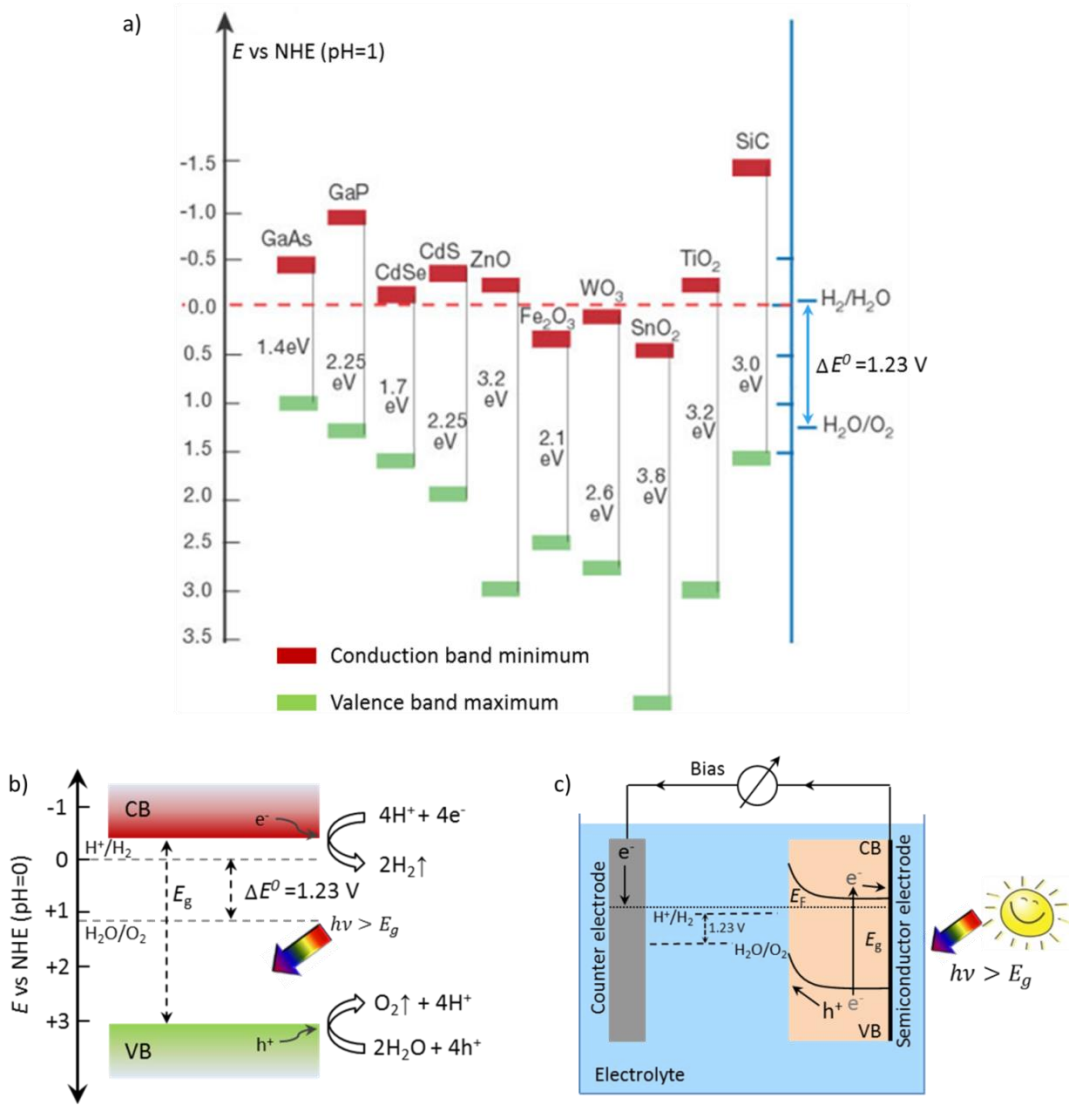

Figure 7: a) Relation between the band position of different semiconductors and redox potentials for water splitting (adapted from [119] with permission), b) schematic representation of the band structure of ZnO under illumination together with the hydrogen and oxygen evolution reactions, c) simplified schematic of a PEC cell with n-type photoanode and metallic counter electrode.

The basic principle of the overall water splitting process is schematically shown in Figure 7b. When a semiconductor photoelectrode is illuminated, the absorbed photons with larger energy than the band gap energy excite electrons into the CB thus forming electron-hole pairs, which are separated by the formed electric field in the depletion layer. If the semiconductor is immersed into a water-based electrolyte, the holes from the VB will drive the OER producing oxygen gas, and electrons from the CB will lead to the formation of hydrogen by the HER according to the following reactions:

$$2H_2O + 4h^+ \rightarrow O_2 \uparrow + 4H^+ \quad (OER) \tag{9}$$

$$4H^+ + 4e^- \rightarrow 2H_2 \uparrow \quad (HER) \tag{10}$$

The semiconductor serves as a photoanode in a PEC cell if it has n-type conductivity (electrons are the majority charge carriers) and as a photocathode if the conductivity is p-type (holes are the majority charge carriers). The schematic of a simple PEC cell with an n-type photoanode, like ZnO, is shown in Figure 7c. The cell consists of the semiconductor photoelectrode (working electrode), a metal counter electrode, which is typically Pt, and a reference electrode required to control the potential of the working electrode (not shown in the schematic). If a bias is applied, the photogenerated electrons and holes will separate and migrate through the semiconductor in opposite directions: the holes will travel to the surface of the n-type semiconductor, where the OER will take place at the electrode/electrolyte interface, and electrons will travel through the external circuit to the counter electrode driving the HER.[118] It is common to use a Ag/AgCl reference electrode for measurements, whereas for data analysis and for ease of comparison with other systems reported in literature, the Nernst equation is used to convert the potentials vs. reversible hydrogen electrode (RHE):

$$E_{RHE} = E_{Ag/AgCl} + 0.059 \cdot pH + E^o_{Ag/AgCl} \tag{11}$$

where E_{RHE} is the converted potential vs. RHE, $E_{Ag/AgCl}$ is the potential applied externally vs. the Ag/AgCl (sat. KCl) reference electrode used, and $E^o_{Ag/AgCl}$ = 0.197 V is the standard potential of a Ag/AgCl reference electrode at 25˚C.[86]

To improve the efficiency of PEC cells, the possible recombination of photogenerated charge carriers traveling to the semiconductor surface or counter electrode should be minimized. For this, nanowire-based photoelectrodes are of interest due to their one-dimensional shape and geometrical orientation which promise higher light absorption and more efficient charge carrier separation and transport to the surface of the electrode as compared to bulk materials.[120–122] The reduced nanowire diameter and large surface area of the photoelectrode/electrolyte interface facilitate rapid transport of photogenerated charge carriers to the wire surface and faster redox reactions, respectively. For example, the diffusion length of bulk ZnO at 25˚C is ~440 nm which increases with higher temperatures.[123] If a film photoelectrode is much thicker than the diffusion length of the minority charge carriers, in this case holes (L_p), not all holes (especially the ones generated in deeper layers of the

semiconductor) will reach the film surface (Figure 8a). In contrast to this, due to the more available surface area of nanowires, the holes will have a shorter path length to quickly diffuse to the electrode/electrolyte interface, thereby also opening a "highway" for electrons to reach the substrate and flow to the external circuit (Figure 8b). Hence, charge transport limitations can be circumvented by means of adjustment of nanowire diameter. Moreover, enhanced light absorption is expected for nanowires compared to films due to extensive light scattering.[124] The reflected light from one wire can be absorbed by the neighboring wire, and if the photon energy is larger than the band gap energy of the material, the reflected light can also excite electrons into the CB. For this approach, tilted nanowire geometry might be beneficial. Also, a composite structure with wide and narrow band gap materials is of interest. The photons which are not absorbed by the wide band gap material or those that are reflected at the surface can excite charge carriers in the narrow band gap material. Another important parameter that should be considered during the material choice is the optical thickness $1/\alpha$, where α is the absorption coefficient. For more efficient devices, the light penetration depth should be comparable with dimensions of the photoelectrode, e.g. film thickness or nanowire diameter.

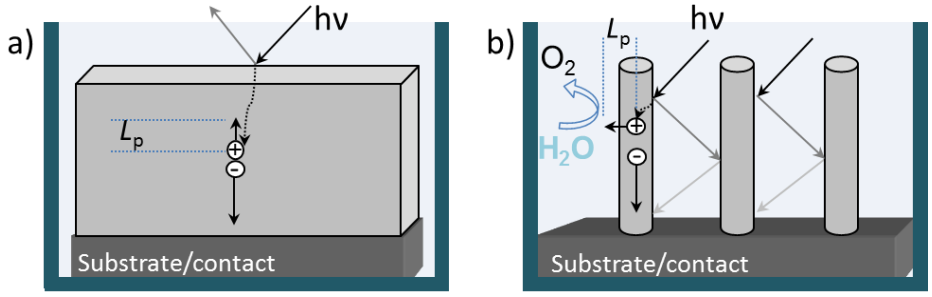

Figure 8: Schematic representation of two photoanodes showing long and short path lengths for photogenerated holes to the electrode surface in a) a film and b) a nanowire array. L_p is the diffusion length to the hole.

One further route to successful transport and collection of photogenerated charge carriers is the use of a photoelectrode with high crystallinity. Electron-hole recombination is less likely to occur in single crystalline structures, whereas the grain boundaries in materials with poor crystallinity are limiting aspects because they serve as traps and recombination centers for electrons and holes.[114,124]

Last but not least, the lifetime of the photoelectrodes should be mentioned. Even if the band position of the semiconductor perfectly matches the OER and HER potentials, the photo- and (electro)chemical corrosions should be taken into account, too. This is probably the most severe limitation for the choice of photo-active materials. For most non-oxide materials a decomposition or oxidation of the surface is typical, while for many oxide materials the thermodynamic instability is accompanied with hole oxidization.[124] In particular, ZnO tends to decompose in aqueous solution under illumination following the reaction below: [114,125,126]

$$ZnO + 2h^+ \rightarrow Zn^{2+} + \frac{1}{2}O_2\,, \tag{12}$$

Fortunately, there are several simple oxide semiconductors, such as TiO_2 or SnO_2, which have excellent stability against chemical and photocorrosion in a wide range of pH values of the electrolyte. Coating other photoactive electrodes with these materials can be a solution to extend the lifetime of the device. In this work, ZnO photoanodes were coated with TiO_2 layers of different thicknesses by atomic layer deposition (ALD). The protection role of the TiO_2 layer during PEC measurements is discussed in Chapter 6.

1.5. Metal-semiconductor contact

To describe metal-semiconductor contacts, band diagrams are usually built to visualize the alignment of the bands at the interface of two materials. This section introduces several characteristic parameters for semiconductors used to describe the band diagrams.

A schematic of the band of a metal and an n-type semiconductor (e.g. ZnO, TiO_2) before and after bringing them into contact are shown in Figure 9 (a) and (b), respectively. The band structure of the metal is characterized by its work function W_m. On the diagram, it is the distance between the Fermi level (the highest occupied electron energy level at absolute zero temperature) of the metal and the vacuum level E_{vac}, and represents the amount of the energy that is required to transport an electron from the Fermi level to the vacuum level. The characteristic parameters shown on the diagram for a semiconductor are the following:

- band gap E_g - distance between the minimum of the conduction band (E_c) and the maximum of the valence band (E_v),
- work function W_{sc} - the distance of the Fermi level (E_F) from the vacuum level,
- ionization energy I_{sc} - the distance of the valence band maximum from the vacuum level.

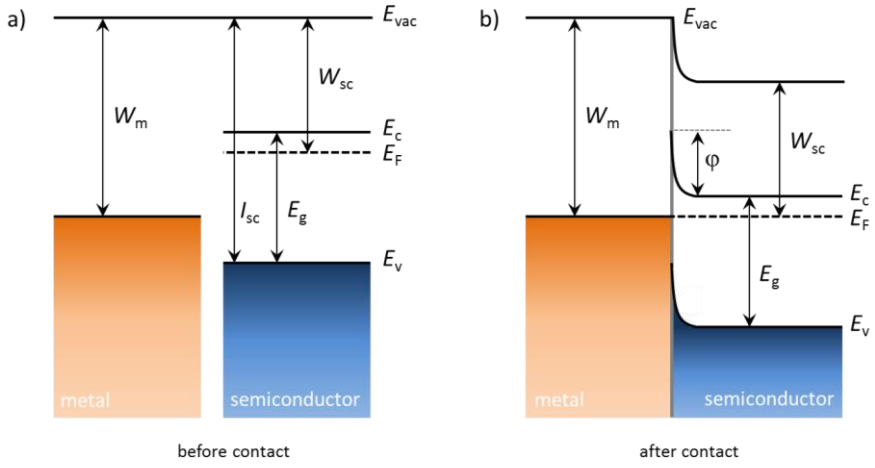

Figure 9: Energy bands for a metal and an n-type semiconductor (a) before and (b) after bringing them into contact. The Fermi level of the metal is lower than that of the semiconductor, i.e. $W_m > W_{sc}$.

Figure 9 shows the case of an n-type semiconductor-metal contact without a bias for which $W_{sc} < W_m$, as for ZnO-Au or TiO_2-Au contacts discussed in detail in Section 6.3. When the two materials are brought into a contact, electrons start to flow from the semiconductor to the metal and vice versa. For the condition $W_{sc} < W_m$ more electrons will "fall down" into the metal, and consequently the metal will become negatively charged. This process will continue until the system reaches the thermodynamic equilibrium, i.e. the Fermi energies are equal (Figure 9b), and the diffusion currents of the electrons flowing in both directions will be identical. The height of the potential barrier, which is formed at the interface of the two materials due to band bending, for electrons flowing from the semiconductor to the metal is defined by their work functions as $\varphi = W_m - W_{sc}$. This potential difference is denoted as contact potential, and the barrier and the contact (for mentioned conditions) are known as Schottky barrier and Schottky contact, respectively.[127]

By means of e.g. X-ray or ultraviolet photoelectron spectroscopy (XPS or UPS), the work function and the distance of the valence band from the Fermi level can be determined. The band gap of the semiconductor is measured using ultraviolet-visible (UV-Vis) light spectroscopy. These three parameters provide information about the positions of E_c, E_F, and E_v versus the vacuum level. Examples of band alignment based on XPS and UV-Vis measurements for Au-TiO_2 and Au-ZnO are shown in Section 6.3.

2. Methods and sample preparation for characterization

In this chapter, the characterization methods are presented. The morphology, crystallinity and composition of the nanowires-based structures were analysed using high resolution scanning electron microscopy (HRSEM), energy dispersive X-ray spectroscopy (EDX), X-ray diffraction (XRD), high resolution transmission electron microscopy (HRTEM) with high-angle annular dark-field imaging (HAADF), selective area electron diffraction (SAED), electron energy loss spectroscopy (EELS), and X-ray photoelectron spectroscopy (XPS). The general process and parameters used for the atomic layer deposition (ALD) and photoelectrochemical (PEC) measurements are described.

2. Sample preparation and characterization methods

2.1. High resolution scanning electron microscopy (HRSEM)

Scanning electron microscopy (SEM) is a widely used technique for characterization of the morphology of nanomaterials and nanostructures. It makes use of focused beam of accelerated electrons to scan the surface of the specimen and obtain a raster image. As an electron hits the surface of the sample, a number of interactions occur between the beam electrons and the atoms of the specimen resulting in emission of different types of electrons (secondary, backscattered, Auger) and X-rays (Bremsstrahlung, characteristic X-rays). By collecting the emitted secondary electrons on a cathode ray tube, topography image of the specimen is obtained. Collection of backscattered electrons emitted from deeper levels of the sample allows for contrast imaging of multicomponent structures when the atomic numbers of components differ widely.

In this study a high resolution scanning electron microscope (HRSEM, JEOL JSM-7401F) equipped with two secondary electron detectors at different positions with respect to the sample stage was used to image the fabricated membranes and nanostructures.

Prior to the SEM analysis the polymer membranes were sputter-coated with a ~8 nm thick Au layer (20 s) using an Edwards Sputter Coater S150B, by applying a pressure of 10^{-1} Torr and a potential of 1.5-1.6 kV resulting in a current varying between 15 and 20 mA. By the sputtered conductive layer the charging effects in SEM were avoided. The microscope was operated at an accelerating voltage of 4 kV in SEM mode. The topography and the pore size were analyzed with low secondary electron imaging (LEI) at a working distance of 8 mm.

To investigate the pore geometry inside the polycarbonate membranes produced by heavy ion irradiation and subsequent chemical etching, the cross section of the membranes was imaged. The samples were prepared in collaboration with Dr. Loïc Burr (Materials Research department, GSI) by irradiating pre-etched membranes with high fluence of 5×10^{10} ions/cm^2 using Au ions with energy of 5.6 MeV/u followed by a 24 h UV treatment on each side of the samples. Due to the severe beam-induced embrittlement the membranes easily break in liquid nitrogen which allows for imaging the cross section of the membranes. Alternatively, the embrittlement of the polycarbonate membranes was obtained by immersing the samples in Aqua Regia solution for ~2 month at room temperature. More details about this process can be found in the doctoral thesis of Dr. Loïc Burr.[128] After breaking the membranes, the samples were glued onto a specially designed SEM sample holder with a cut of 90˚ to image the cross section. Prior to the SEM analysis the samples were coated with ~8 nm Au, as described above. For these samples SEM was operated at 10 kV with LEI detector.

For SEM investigation of the nanowire arrays and networks, the polymer membranes were dissolved in dichloromethane (CH_2Cl_2 for analysis, Merck) in several steps. The nanowire arrays/networks embedded in the polymer membranes were placed horizontally in sample

holders in such a way, that the edges were fixed to avoid folding of the sample which can cause damage to the wires. CH_2Cl_2 was dropped continuously on top of the samples until the level of dichloromethane (with polymer residues) reached the sample holder but did not cover the sample. If the solution covers the sample, it might contaminate the surface of the sample with the dissolved polymers residues. A continuous flow of CH_2Cl_2 was found to be an important step. If the sample with partially dissolved polymer was exposed to air for a relatively long time (a minute or more), it seemed to harden resulting in broken the wires. After repeating this step twice, the samples were immersed in a fresh CH_2Cl_2 bath and left for 1h. This latter step was repeated three to four times. Finally, the free-standing nanowire arrays and 3D nanowire networks with the metallic electrode were dried in air and inspected by SEM. Both ZnO and ZnO/TiO_2 nanowire arrays, networks and films were characterized by using SEM in gentle beam-low mode (GB-Low) with an upper secondary electron detector imaging (SEI) at 2 kV accelerating voltage at a distance of 6 or 8 mm.

For nanowire diameter and length analysis, single nanowires were transferred onto Si wafers, pre-cleaned with acetone and deionized water. The following two methods were applied: (i) after dissolution of the membrane, some of the wires were detached from the back-electrode by exposing the samples immersed in CH_2Cl_2 to an ultrasonic bath (Elma, Transsonic T460/H) for a few seconds. The released nanowires were then transferred onto a Si wafers by drop-casting the nanowire/CH_2Cl_2 mixture. (ii) The wires still embedded in the membrane were immersed in dichloromethane in centrifuge tube. After an ultrasonic treatment for 15-20 s, the tube was centrifuged three to five times at 4000 rpm for 20-30 min using Heraeus Biofuge primo R Centrifuge. In between these steps, the dichloromethane bath was replaced with a fresh one. Before each step of centrifugation, the nanowires with the fresh dichloromethane were mixed on a shaker for 2-5 min to disperse the wires in the solution for better cleaning. Finally, the solution containing the wires was drop-casted onto Si wafers. The samples were analyzed by operating the SEM at the same conditions as for nanowire arrays and networks attached to their substrates.

Core-shell nanowires and small pieces of nanowire networks were transferred onto Au-TEM grids (Plano GmbH) by drop-casting the wires with CH_2Cl_2 onto the grid. To analyze the samples in transmission mode by SEM, 10 kV accelerating voltage was applied, and the wires were imaged with LEI detector at a working distance of 8 mm. To study the dispersity of the nanowires, which were transferred onto TEM grid by rubbing the grid on the surface of the network, GB-Low mode at 2 kV and probe current of 7 at a distance of 8 mm was used.

2.2. Energy dispersive X-ray spectroscopy (EDX)

Characteristic X-rays emitted from the sample depend on the atomic number of elements in the structure and are mainly used for quantitative and qualitative chemical analysis.

The composition of the nanowire arrays, networks and single wires was studied by energy dispersive X-ray spectroscopy (Bruker) in the SEM. Multipoint spectra and line scans were recorded by applying an accelerating voltage of 10 or 20 kV and a probe current of 10-12 depending on the amount of material present, at a fixed distance of 8 mm. The acquisition time was ~8 min for multipoint scans and ~10 min for line scans. The analysis of the spectra was done by using the Quantax software from Bruker.

2.3. X-ray diffraction (XRD)

XRD is a nondestructive technique that uses collimated beam of X-rays to investigate the arrangement of atoms within a crystal. When X-ray beam strikes the sample it diffracts in different directions from the atoms of crystal planes. If the wavelength λ of X-rays, the incident radiation angle θ and the crystal lattice *d*-spacing satisfy Bragg's law ($n\lambda=2d\sin\theta$) constructive interference is produced and the diffracted X-rays can be detected. The recorded diffractogram provides information about crystal phase, crystallographic orientation and lattice parameters of the crystal, defects, stresses, etc.

The crystallographic structure of the cylindrical and conical nanowire arrays still embedded in the membrane was analyzed by using an X-ray diffractometer (XRD, Seifert X-Ray generator, HZG-4 goniometer in Bragg-Brentano geometry) with a generator voltage of 40 kV and a current of 30 mA using Cu Kα radiation (λ=1.54056 Å). The device was operated by the Rayflex software. The scan rate and integration time were 0.02˚ and 20 s, respectively.

The XRD patterns of networks after dissolution of the membrane were recorded with a D2 PHASER diffractometer (Bruker), which was operated at a generator voltage of 30 kV and a current of 10 mA (Cu Kα radiation). With this device the scan rate and integration time were 0.05˚ and 20 s, respectively, and the measurement was controlled with DIFFRAC.SUITE™ software.

2.4. High resolution transmission electron microscopy (HRTEM)

Transmission electron microscopy (TEM) is one of the techniques allowing for analysis of material structure on an atomic scale. It enables the analysis of the crystal structure, chemical composition and contaminations through diffraction pattern, X-ray and electron-energy loss analysis. In TEM accelerated electrons are projected onto a thin specimen and penetrate the sample undergoing either elastic or inelastic scattering with its atoms. The transmitted and elastically scattered electrons are used to build a high resolution TEM image and/or record selected area electron diffraction (SAED) pattern. Inelastically scattered electrons that lose energy are detected by a high-angle annular dark-field (HAADF) detector for mass contrast imaging and/or by a spectrometer for electron energy-loss spectroscopy (EELS) allowing for chemical mapping and composition profile analysis.

To analyze the crystallinity and purity of ZnO and ZnO/TiO_2 wires, as well as the homogeneity and phase of TiO_2 layers coated on top of ZnO wires by atomic layer deposition

(ALD), the wires from arrays and networks were transferred onto Au-TEM grid as explained in Appendix E. In collaboration with Dr. Wilfried Sigle from the MPI for Solid State Research in Stuttgart the wires were inspected by using a high resolution transmission electron microscope (HRTEM, JEOL-ARM200CF) together with high-angle annular dark field (HAADF) imaging and electron energy loss spectroscopy. Selected area electron diffraction was used for analysis of the crystallographic structure of the wires in micron-scale. The device was operated at an accelerating voltage of 200 kV and an emission current of 15 μA.

2.5. Photoelectrochemical (PEC) measurements

The photoelectrochemical (PEC) measurements presented in the thesis were performed at the GSI in Darmstadt and Univeristy of Twente (The Netherlands) in the group of Prof. Dr. Guido Mul.

The setup at the GSI consisted of a LS0108 solar simulator from LOT Quantum Design GmbH (AM 1.5G), a Reference 600^{TM} potentiostat (GAMRY Instruments) and a PECC-2 photoelectrochemical cell (ZAHNER-elektrik GmbH & Co. KG) with a 8 mm O-ring defining the photoactive area of the sample.

For the PEC measurements at the University of Twente a setup consisting of a 300 W Xe lamp with AM 1.5 filter (Newport corporation), a potentiostat (VERSASTAT4, Pinceton applied reserach), and PECC-2 photoelectrochemical cell (ZAHNER-elektrik GmbH & Co. KG) with a 7 mm O-ring were used.

All measurements were performed in 0.1 M K_2SO_4 (Sigma Aldrich) aqueous solution with a pH of 5.6. The distance of the PEC cell was calibrated with a Si solar cell (Newport Oriel, P/N 91150V) to obtain an illumination of 1 sun on the sample.

2.6. X-ray photoelectron spectroscopy (XPS)

X-ray photoelectron spectroscopy (XPS) is a surface sensitive technique employed for analysis of chemical composition and electronic states of a material within a depth of ~10 nm on the surface of a specimen. When an incident photon (X-ray) hits the surface of the sample with energy higher than the ionization energy of the material, electrons are ejected from the samples. The kinetic energy E_{kin} of the released electrons can be detected by a photoelectron spectrometer. It related to incident photon energy $h\nu$ by $E_{kin}=h\nu-(E_b+\Phi_s)$, where E_b is the binding energy required to transfer the excited electron to the Fermi level, and Φ_s is the work function of the spectrometer. A spectrum revealing the number of ejected electrons vs. kinetic energy provides information about the energy levels in the inner electron shells of the specimen atoms.

XPS was applied to analyze the surface of nanowire networks to identify modifications and/or corrosion of the surface after PEC measurements as well as to estimate possible contaminations on the wires (e.g. residues from polymer or dichloromethane) which might

affect the PEC performance. XPS was also used to determine the work function and the valence band positions for visualization of the band alignment of Au-ZnO and Au-TiO_2 Schottky contacts. The measurements were performed at the DAISY-FUN (DArmstadt's Integrated SYstem for FUNdamental research) of the Surface Science group of Prof. Dr. Wolfram Jaegermann at the TU Darmstadt in collaboration with Dr. Florent Yang. The spectra were recorded by using a PHOIBOS 225 (Specs GmbH) analyzer and a monochromatic Al Kα radiation with excitation energy of 1486.74 eV. Before each measurement, the system was calibrated with a high purity Ag sample (freshly sputter cleaned under Ar atmosphere) with a very high purity to calibrate the Fermi level. For determination of the work function, a negative bias of 3 V was applied between the analyzer and the sample for distinguishing the signal from the sample.

3. Fabrication of etched ion-track membranes

Ion irradiation and etching processes required for the fabrication of etched ion-track polymer membranes are described in this chapter. Three main geometries are discussed: **vertically aligned cylindrical and conical channels** and well as **interconnected channel networks**. Superstructures consisting of both vertically aligned and interconnected channels are introduced.

3. Fabrication of etched ion-track membranes

Etched ion track membranes were prepared by chemical etching of ion irradiated foils. During this process the damaged material in the tracks is selectively removed converting the ion track into channels (pores). By adjusting the ion fluence (number of ions per area), the number of pores in the membrane can be controlled, since each ion passing through the polymer foils creates one track. Using different irradiation and etching conditions (e.g. concentration of the etchant, temperature, and etching time and setup configuration), polycarbonate membranes were fabricated with parallel cylindrical, parallel conical and interconnected cylindrical nanochannels (Figure 10). Irradiation and etching conditions employed for the fabrication of these three types of templates are presented in the following section.

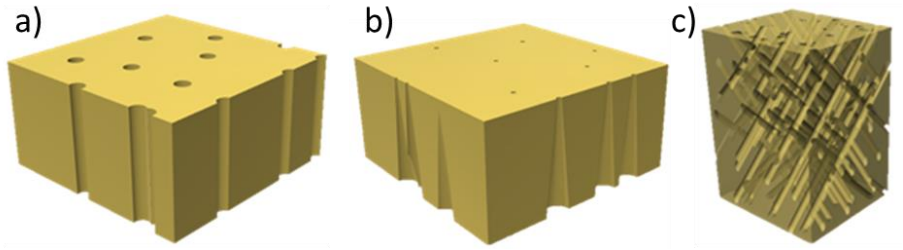

Figure 10: Schematic representations of membranes with a) parallel cylindrical, b) conical and c) interconnected cylindrical pores.

3.1. Parallel cylindrical pores by symmetric etching

Polycarbonate (PC) foils with a thickness of 30 µm (Makrofol N, Bayer AG) were irradiated with ~2 GeV Au and Bi ions at the X0-beamline of the universal linear accelerator (UNILAC) at GSI. In order to fabricate membranes with parallel nanochannels, the irradiation was performed under normal beam incidence (perpendicular to the foil surface), typically applying a fluence of 10^9 ions/cm^2. Prior to etching, both sides of the irradiated polymer foils were exposed to UV light (30 W, 312 nm, T-30M, Vilber Lourmat) in air to improve the homogeneity of the pore diameter distribution over the whole sample. [81,129] By immersing the irradiated foils in a 6 M sodium hydroxide (NaOH, Sigma Aldrich, > 97 %) solution at 50˚C, the tracks were selectively dissolved and converted into cylindrical channels. Given by the general etching of the bulk polymer the total thickness of the membrane slightly decreases (Figure 11a).[76] Symmetric etching was performed in a double-walled cylindrical pot connected to a heating water circuit (Figure 11b). In this configuration the etching solution had an access to the tracks from both sides of the irradiated foils. In order to improve the convection and to keep the bath temperature constant, the etching solution was stirred at ~250 rpm. To produce multiple membranes with identical pore diameter, four samples were etched at the same time. Various etching times were employed between 1.5 and 8 min. The schematic of the evaluation of the track etching and the channel opening with the increase of time are shown in Figure 11c. Under these etching conditions, the pore diameter increased linearly with etching time. However, the etching rate varied depending on the aging of the

polymers, i.e. the time period between irradiation and etching processes. Longer aging periods led always to higher etching rates. The values usually varied between 20 and 30 nm/min. After etching, the membranes were rinsed with deionized (DI) water by immersion in multiple water baths, and finally dried in air.

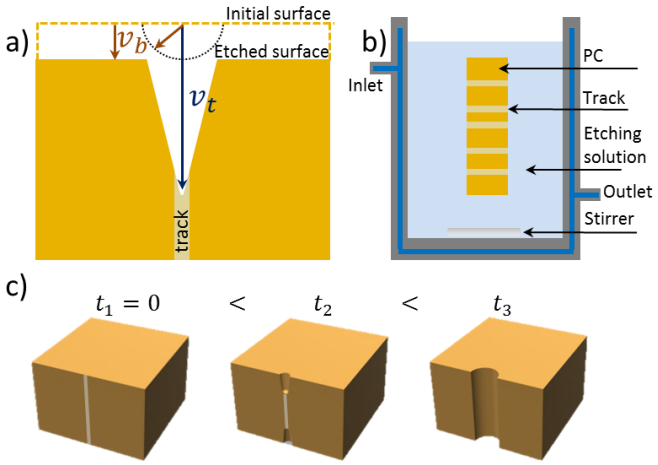

Figure 11: Schematic representations of a) etching of single. Nanochannel formation requires a higher track etch rate compared to the bulk etch rate, b) thermostated pot for symmetric etching, c) the nanochannel opening process for different etching times.

Pore size and size distribution were analyzed by HRSEM. For membranes etched without UV treatment an inhomogeneous size distribution of the pores was observed (Figure 12a). The areas marked with red and orange circles in Figure 11a show smaller and larger pores with average diameters of 170±2.22 and 350±5.74 nm, respectively, as compared to the mean diameter of the majority of the pores being 300±79 nm. A pre-sensitization step with 1h UV light on each side of the irradiated foils before etching yielded a more homogeneous etching and size distribution (Figure 12b). The average pore diameter of this sample was 220±1.9 nm.

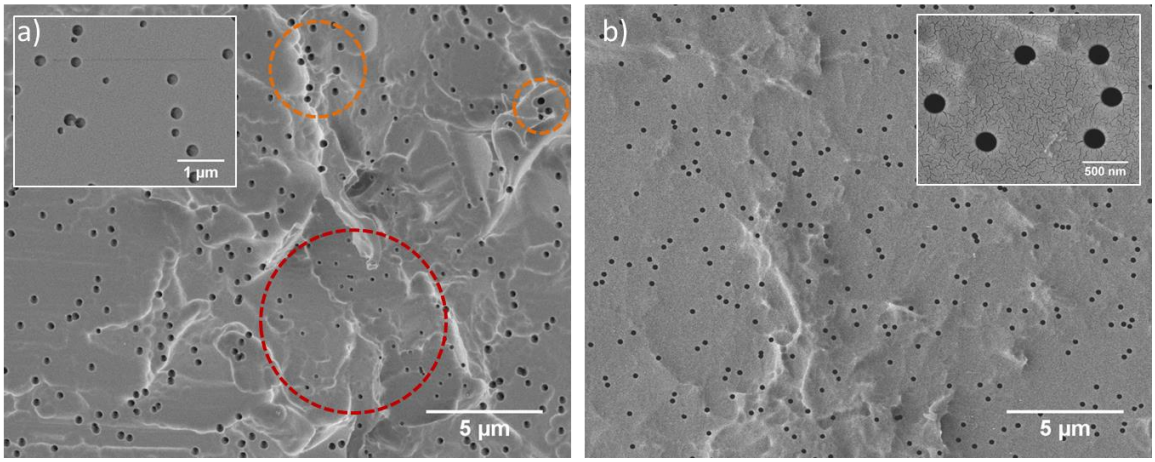

Figure 12: Representative SEM images of the surface of track-etched membranes etched under identical conditions a) without and b) with UV pre-treatment showing a broad (a) and an uniform (b) distribution of the pore diameters.

Figure 13 shows the average pore diameters and standard deviation of samples etched for different etching times. All samples were sensitized with UV light prior to the etching. However, the ion type and the aging periods for these foils were different, which resulted in diverse etching rates. The black and green curves show a perfect linear dependence. However, the aging times are different, being 4.5 months for the black curve, and 19 months for the green curve. Additionally, they were irradiated with different ions: Bi ions (black curve) and Au ions (green curve), both with an energy of 11.1 MeV/u. Since the energy loss for both ions in the PC foils is comparable, the difference in etching rates (22±0.34 and 25±0.37 nm/min for black and green curves, respectively) is assigned to the aging of irradiated foils. The etching rate was deduced from the slope of the linear fit to the data points. The inset in Figure 13 shows the etching rate values as a function of the age of the irradiated foils. The red curve corresponds to samples which were irradiated with Au ions and had the longest aging period of 44 months. Despite the deviation of the point corresponding to 5 min etched sample, assuming the linear behavior, the etching rate was calculated from the slope to be 28±4.6 nm/min.

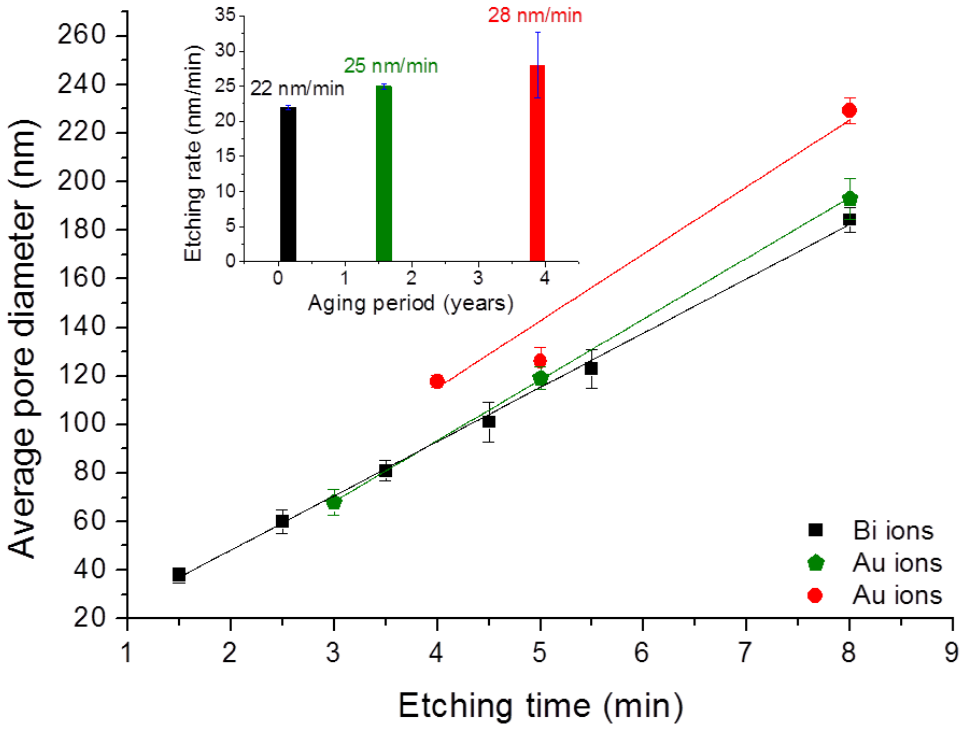

Figure 13: Average pore diameters measured with SEM as a function of etching time and aging periods: 4.5 month (black), 19 month (green), 44 months (red).

Last but not least, the variation of the etching rate from sample to sample can also arise from the concentration of the etching solution and the temperature in the bath: higher pH and temperature will result in faster etching, and vice versa.

3.2. Vertically aligned conical pores by asymmetric etching

To fabricate membranes with conical channels, the etching of the irradiated PC foils with a thickness of 30 µm and parallel tracks with a number density of 10^7 tracks/cm^2 was performed in a specially constructed electrochemical cell under asymmetric etching conditions. The schematic of the setup is shown in Figure 14a. The foils were introduced in between the two compartments of the cell. One compartment was filled with the etching solution containing a mixture of 9 M NaOH and methanol in a 60:40 volume ratio, while the other compartment was filled with deionized water which served as a stopping solution. In such a configuration, the etching took place only from one side. Due to the addition of methanol to the NaOH etchant a conical pore geometry with a large base and reduced tip diameters was achieved. During the etching process, the temperature of the cell and solution was kept at 30˚C and a potential of 1 V was applied between two gold electrodes that were immersed in the etching and stopping solutions. The potential difference between the two electrodes prevented the flow of OH^- ions of the etching solution into the pores, thereby slowing down the etching process and allowing the formation of conically shaped channels. The current as a function of etching time was monitored and recorded. Once the tracks were etched through, the current started to flow and increased with time (Figure 14b). The breakthrough point is indicated by a sharp current increase occurring after ~140 s. The samples were etched for 12 min resulting in base and tip diameters of 2 - 2.5 µm and 70 - 90 nm, respectively.

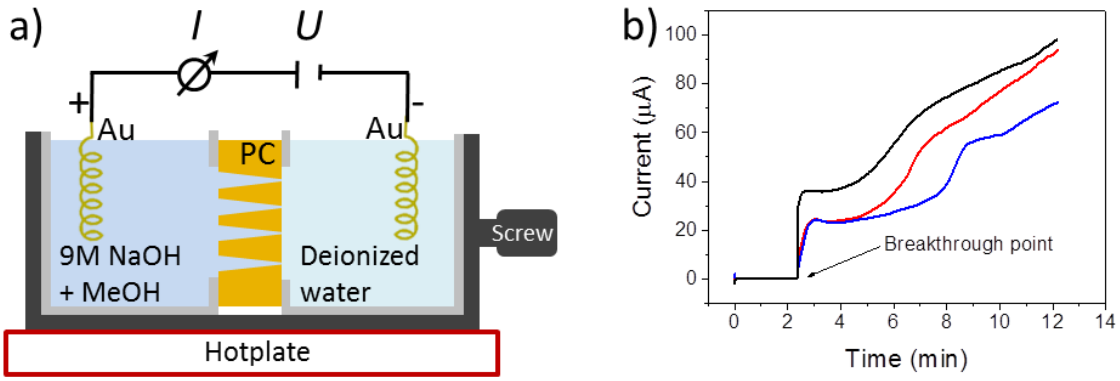

Figure 14: a) Schematic of asymmetric etching setup consisting of two compartments filled with etching and stopping solutions, and the membrane fixed in between the two compartments. b) Current vs. time curves of chemical etching of conical pores with a similar breakthrough point for three similar samples.

3.3. Membranes with networks of interconnected pores

Membranes with interconnected nanopore networks were prepared by chemical etching of PC foils with tilted intersecting ion tracks. The network were obtained by irradiating the foils four times in consecutive steps, each time from a different direction under an angle of 45˚ with respect to the surface normal of the polymer foil (Figure 15). At each position, the foils were irradiated with a fluence of 5×10^8, 10^9 or 2×10^9 ions/cm^2, resulting in a total fluence of

2×10^9, 4×10^9 and 8×10^9 ions/cm^2, respectively. The irradiated foils were symmetrically etched for 5-10 min in 6M NaOH at 50˚C (as described in Section 3.1), which resulted in networks of nanochannels with defined channel diameter. It was found that the etching rate is slightly slower than that in case of parallel cylindrical pores, which is probably due to the complex and dense structure of interconnected pores. According to a systematical SEM analysis of series of 5, 7 and 9 min etched samples, the etching rate was ~22 nm/min (Appendix A). The total inner surface of the nanopore networks depends on the ion fluence and channel diameter.

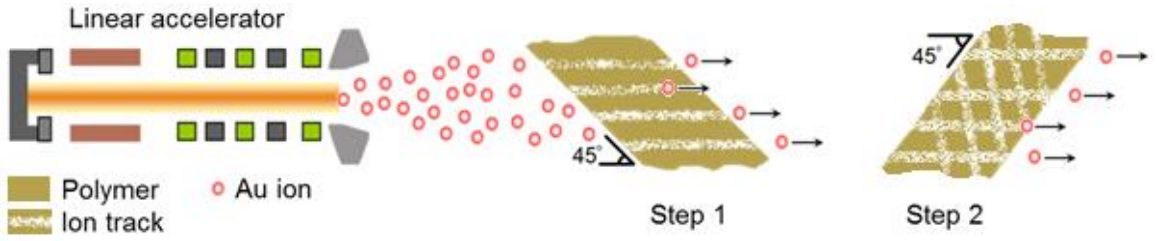

Figure 15: Irradiation scheme for obtaining nanochannel networks (only two out of four irradiation directions are shown).

Figure 16a shows the schematic of the cross-section of the simplest configuration of a network structure irradiated in four steps. Unfortunately, long term etching of high-fluence networks (e.g. more than 7 min etching of networks with a track total density of 8×10^9 cm^{-2}) led to dissolution of the membranes because of severe overlap of etched pores. This seemingly inevitable problem was circumvented by irradiating the network samples additionally from a fifth position under normal incidence of the beam (perpendicular to the surface of the foils) instead of increasing the fluence of ions for irradiation under an angle. In other words, to obtain the same total track-number density of 8×10^9 cm^{-2} (2×10^9 ions/cm^2 from 4 directions) the foils are irradiated with 1.6×10^9 ions/cm^2 from 5 directions. The cross-section of such network structure is shown in Figure 16b, where the parallel vertical pores correspond to the fifth step of irradiation with ions. This fifth step also has a positive influence on the homogeneous growth and mechanical stability of the network electrodeposited in such membranes. Another approach to increase the surface area was irradiation of pre-etched membranes with conical or cylindrical pores (Figure 16 c,d). First, the 30 and 60 µm thick PC foils were irradiated with heavy ions using a rather low fluence varying between 10^5 and 10^6 ions/cm^2 under normal incidence of the beam. After symmetric or asymmetric etching, vertically aligned cylindrical and conical pores were obtained. As a second step, these membranes were irradiated with higher fluences under 4 tilted beam incidences to obtain a network configuration. The etching process after the second irradiation resulted in a network combined with vertically aligned cones or parallel cylinders with significantly increased surface area. Last but not least, reverse network-tree structures were fabricated, where the network had a height of 1/3 or 2/3 of the length of the cylindrical and conical channels (Figure 16 e,f). These structures may be useful for the synthesis of very long

wire arrays. They will allow stabilization of the array at the base of the wires, whereas the tips of the wires will stay free of network while being vertically aligned without assembling bunches. This property is especially important e.g. for nanowire array-based emitters.

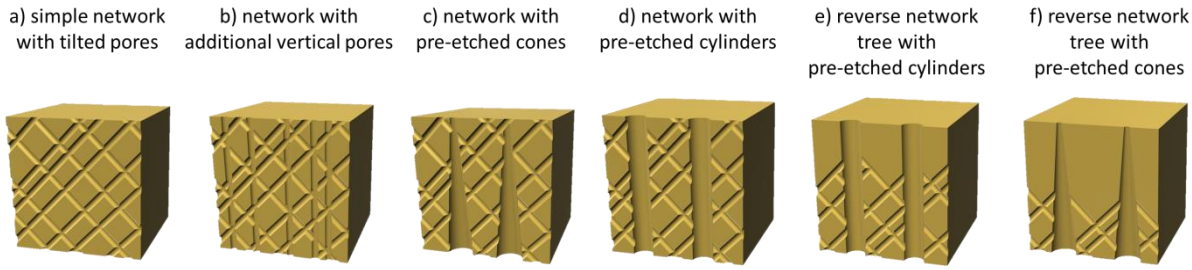

Figure 16: Schematics representation of cross-sections of a) the simplest and b) advanced configurations of a network structure obtained after etching of PC foils irradiated under 45° angle in a) four and b) five steps; networks combined with pre-etched vertical c) conical and d) cylindrical arrays, e,f) reverse network tree structures showing pre-etched cylindrical or conical pores supported with network at the base.

Figure 17 shows representative SEM images of a network membrane surface (a) and cross-sections (b-d) of different types of network structures. In Figure 17a, a typical porosity of the surface of a network membrane is shown (here the total pore number density is $2x10^9$ pores/cm^2). The inset presents a higher magnification image of 210 nm pores formed by irradiation from four different directions (marked with arrows) under an angle of 45° and etched for 10 min. The cross-section of a similar membrane with pores of 150 nm diameter (etched for 7 min) is shown in Figure 17b. The roughness at the edge of the polymer arose from the breaking of the membrane. Three of the four irradiation directions are indicated by arrows in the zoomed-in image. For the fourth direction, only the pore openings can be identified from this image. Figures 17c and 17d show the cross-sections of networks combined with pre-etched vertically aligned conical and cylindrical channel arrays, respectively. The inset in Figure 17c shows the cross-section of the tip of a cone with the network channels penetrating through the cones. The two insets in Figure 17d present the cross-section (top inset) and surface (bottom inset) of a membrane with pre-etched cylinders (20 min etching, density of 10^6 cm^{-2}) and post-etched nanochannel-network (5 min etching).

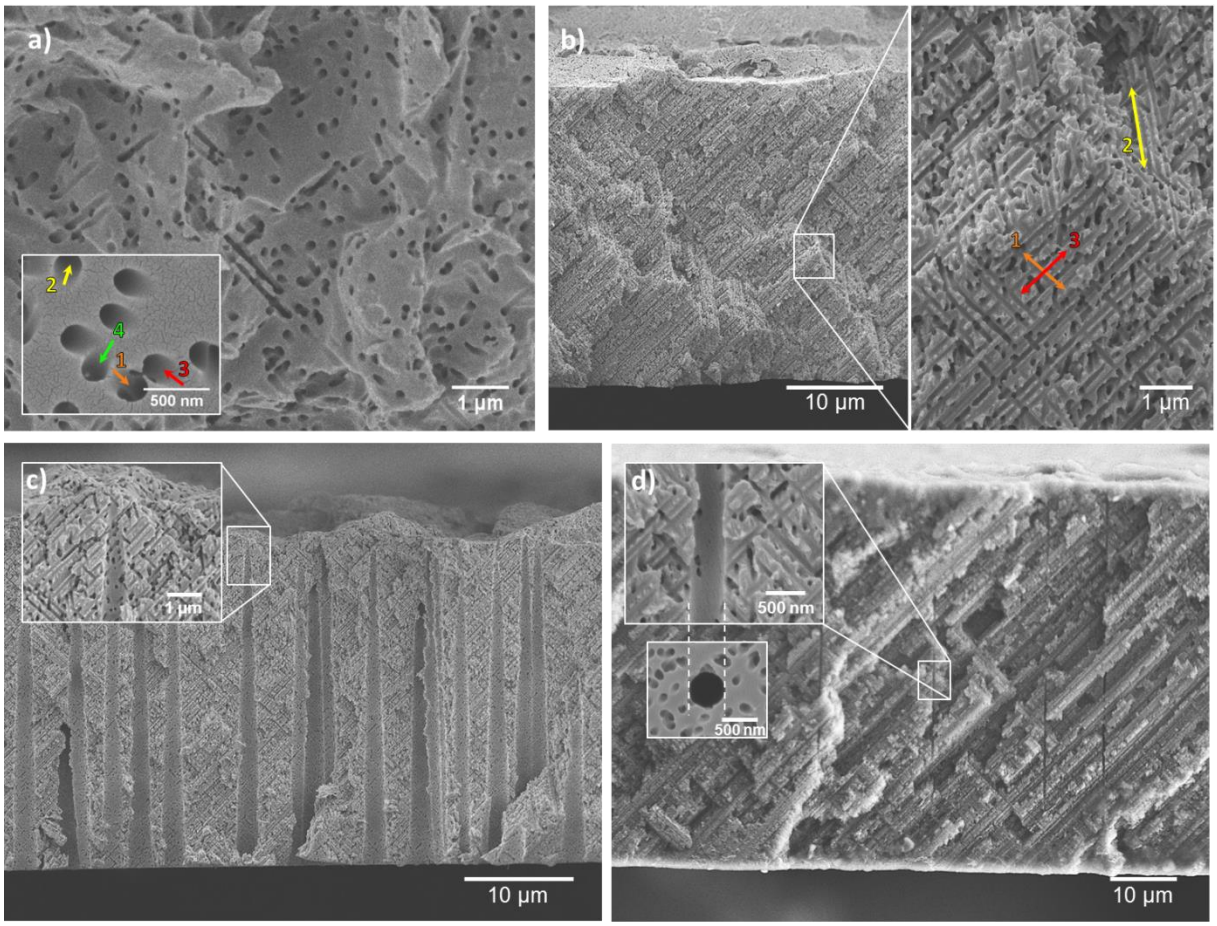

Figure 17: SEM images of a) the surface of a network membrane with an inset showing the pores formed by irradiation from four different directions under an angle of 45°; b) cross-sections membranes with high aspect ratio network channels indicating three out of four directions of intersecting pores; networks combined with vertically aligned pre-etched c) conical or d) cylindrical channel arrays. The inset in (c) presents the cross-section of the tip of a cone with the network. The two insets in (d) show the cross-section (top inset) and surface (bottom inset) of a membrane with a pre-etched cylinder and post-etched channel network.

Additionally, series of PC foils were irradiated with an Al placed mask in front of the foil stack. These masks, which had a pre-defined circular opening in the center with a diameter of 5, 7, or 15 mm, prevented the penetration of the heavy ions through the mask, and only the open area to the foil was irradiated. This resulted in the formation of channel-networks with a confined area, which improved the efficiency of the electrodeposition process (see Section 4.3.1).

The synthesis of ZnO cylindrical, conical nanowires and interconnected nanowire networks inside track-etched membranes is discussed in Chapter 4.

4. Electrodeposition and characterization of ZnO micro- and nanowires

This chapter deals with the reproducible growth of ZnO nanowire based structures in a controlled manner. The electrodeposition conditions, such as the applied potential, electrolyte concentration and electrodeposition time as well as the membrane-pore diameter were varied to study their influence on the morphology and the crystallographic properties of the parallely aligned cylindrical nanowire arrays. Additionally, vertically aligned conical ZnO nanowire arrays are presented. A nanowire network system consisting of tilted intersecting ZnO cylindrical wires is highlighted. The growth conditions and parameters of the wires (e.g. diameter, density and length) in the networks are adjusted in order to obtain homogeneous and stable 3D structures.

4. Electrodeposition and characterization of ZnO micro- and nanowires

Etched ion-track membranes are being used since decades as templates for the electrochemical deposition of nanostructures inside the channels.[40,42] In general, electrodeposition of micro- and nanowires can be carried out using either a two- or a three-electrode setup in potentiostatic or galvanostatic mode, as well as by pulsed electrodeposition conditions. In this work, a two-electrode setup was used for electrodeposition of a so-called back-electrode, which is deposited on one side of the membrane to close the pores and to serve as a working electrode for the membrane during the growth of the wires. In contrast, the synthesis of ZnO nanowires was performed in a three-electrode configuration in potentiostatic mode, as described in Section 1.2. The process for the synthesis of ZnO nanostructures is schematically shown for the case of networks in Figure 18, and consists of the following steps: a) irradiation of polycarbonate (PC) foils with heavy ions (e.g. Au or Bi), b) chemical etching for transformation of the ion tracks into channels, c) sputtering and electrodeposition of metallic layer (back-electrode) as an electrical contact, d) electrodeposition of nanowires, e) removal of the polymer by dissolution in dichloromethane. The same steps were employed for the synthesis of the arrays of the cylindrical and conical nanowires.

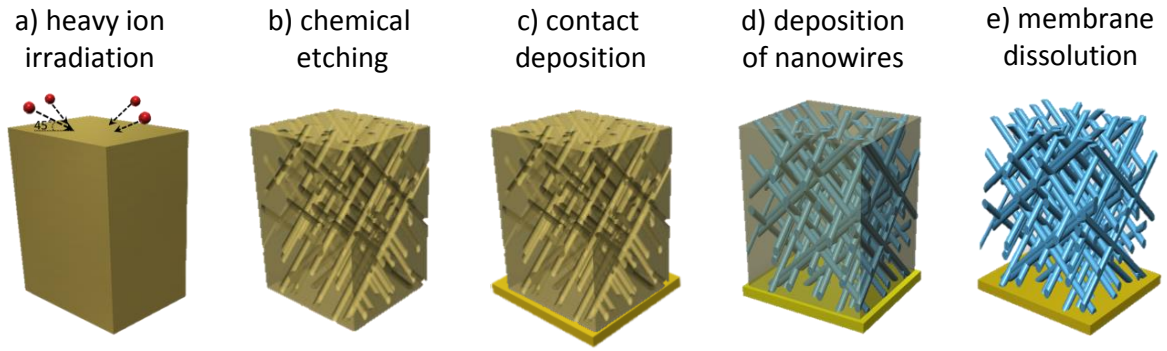

Figure 18: Schematic view of different steps of nanowire synthesis: a) heavy ion irradiation, b) chemical etching in 6M NaOH, c) gold sputtering and electrochemical deposition of metallic (Au or Cu) back-electrode as a back contact, d) electrochemical deposition of nanowires/nanowire network inside the membrane, e) dissolution of the polymer.

4.1. Cylindrical micro- and nanowires

For electrodeposition of parallel cylindrical nanowires, 30 μm thick membranes with pore number density of 10^9 cm^{-2} were used. Different parameters and conditions, such as the applied potential, size of the pores in the membranes, electrodeposition time, and concentration of the electrolyte were varied in order to observe changes of morphology, composition and texture of the wires depending on deposition conditions. The electrodeposition and characterization of ZnO nanowires are presented in the following sections.

4.1.1. Preparation of the back-electrode

Prior to the electrodeposition of the back-electrode, a ~120 nm thick Au layer was sputtered (Edwards Sputter Coater S150B, 10^{-1} torr, 1.5-1.6 kV, 15-20 mA) on one side of the PC membrane to provide an electrical contact to the polymeric sample. This sputtered layer was then reinforced with either a gold or copper back-electrode, which closes the channels on one side of the membrane, and thereby prevents flow of the electrolyte through the pores to the back side of the sample. Additionally, the back-electrode acts as a working electrode during electrodeposition of the nanowires. Both Au and Cu layers serving as back-electrodes were electrochemically deposited in a two electrode setup as shown in Figure 19 for the case of Au deposition. The PC membrane was introduced in the cell between the two Teflon compartments in such a way that the sputtered side was in contact with a Cu ring, which was used to electrically contact the sample. The Au layers were grown at a constant potential of -0.7 or -0.8 V, resulting in a current of ~1 mA. A commercial gold sulphite bath (AuSF, 15 g/L Au, METAKEM) was used as electrolyte, and a Au rod was the anode. Cu back-electrodes were deposited at a constant potential of -0.5 V using a solution of 238 g/L $CuSO_4 \cdot 5H_2O$ (Sigma Aldrich, >98%) and 21 g/L H_2SO_4 (Merck, 95-97%) and a Cu rod as anode, which resulted in a current of ~20 mA during the electrodeposition.

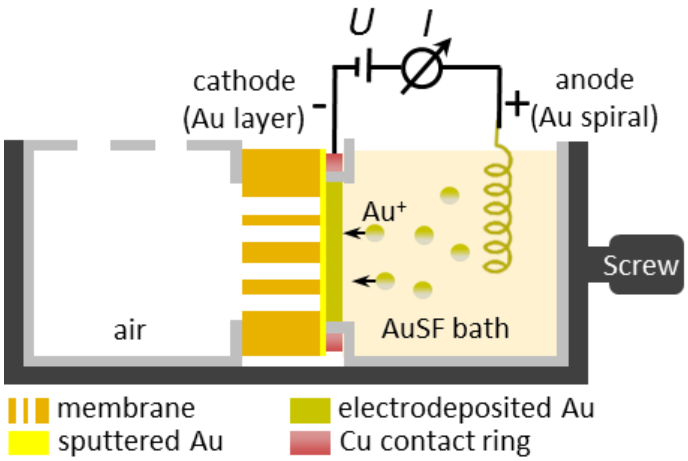

Figure 19: Schematic representation of a two-electrode setup for electrodeposition of a Au layer on the sputtered gold of the membrane by applying a constant potential of -0.7 or -0.8 V.

Depending on the pore size of the membranes, the deposition time for the back-electrode was increased to assure the complete coverage of the pores. For pores with a diameter up to 300 nm Cu and Au layers were deposited for 45 min and 3.5 h, respectively, which corresponds to a thickness varying between ~7 and ~10 µm in both cases. After deposition of the back-electrode, the samples were rinsed with deionized water and dried with a stream of nitrogen gas.

4.1.2. Synthesis of arrays with parallel cylindrical ZnO wires

Figure 20 schematically presents the three-electrode configuration of the setup employed for electrochemical deposition of the nanowire arrays. The electrodeposition was performed using a potentiostat (GAMRY Instruments, Reference 600TM) with the Au or Cu layer on the membrane acting as a working electrode, a Pt spiral wire (Good- fellow, 99.99+%) as a counter-electrode, and a Ag/AgCl reference electrode (Sensortechnik Meinsberg GmbH, sat. KCl). The membrane was fixed in between two Teflon cell compartments so that the metallic layer was in contact with the copper ring serving as a contact between the membrane and the external circuit.

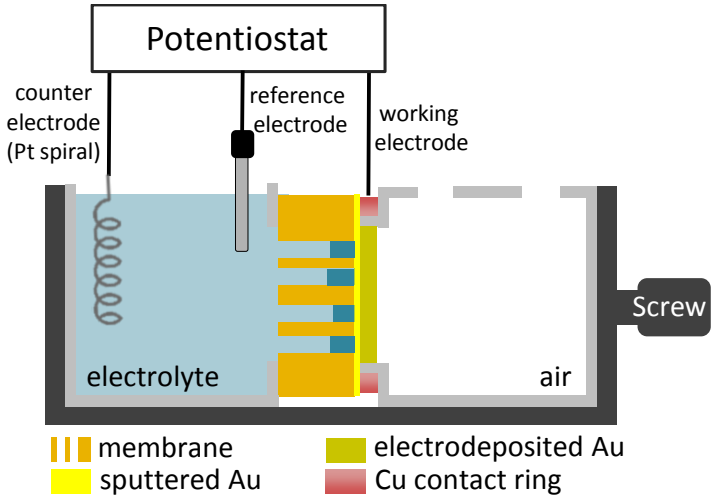

Figure 20: Schematic representation of a three-electrode setup consisting of working, counter and reference electrodes and connected to a potentiostat.

30 µm thick etched ion track membranes with various pore diameters between 40 and 300 nm were employed as templates. An aqueous solution containing a 0.1 or 1 M zinc nitrate hexahydrate $Zn(NO_3)_2 \cdot 6H_2O$ was used as an electrolyte. To wet the pores of the membrane completely, the electrolyte was filled in the cell 1 h before applying a potential. Different potentials ranging between -0.5 and -1 V vs. Ag/AgCl and a temperature varying between 60˚C and 80˚C were applied and adjusted for reproducible growth of these wires. The influence of the deposition parameters (such as deposition time, electrolyte concentration and potential) on the morphology, composition and crystallographic properties of these nanowires was investigated by using scanning electron microscopy (SEM), energy dispersive X-ray spectrometry (EDX), and X-ray diffraction (XRD), respectively. The sample preparation processes for the measurements are described in detail in Chapter 2. Novelty was the study on the influence of the pore diameter on the crystallographic properties of ZnO nanowires. The results are summarized in the following sections.

4.1.3. Influence of the electrolyte concentration on the morphology of the wires

30 µm PC foils with pore diameter of ~200 nm and density of 10^9 pores/cm^2 were employed as templates to grow ZnO nanowires using 0.1 and 1 M $Zn(NO_3)_2 \cdot 6H_2O$ electrolytes at a fixed temperature and potential being 80˚C and -0.8 V vs. Ag/AgCl, respectively. As an initial step, the parameters for the temperature and potential were adapted from Sima *et.al*.[46] After the electrodeposition, the polymer matrix was removed by immersing the samples into a dichloromethane bath and washing in several steps. The morphology of the clean wires was studied by using SEM.

Figure 21 shows SEM images of the resulting nanowires deposited from a) 0.1 M and b) 1 M electrolytes. The wires grown using a lower concentration electrolyte display a smother surface (Figure 21a) as compared to the wires which were deposited from a high concentration electrolyte bath (Figure 21b). The deposition rate was slower for the sample grown from the 0.1 M electrolyte due to the lower concentration of the ions, which led to the growth of continuous and smooth wires, while very rough and brittle wires were obtained at a faster deposition rate from the higher concentrated bath (1 M). For this reason, further studies of different ZnO wires were performed by using 0.1 M electrolyte.

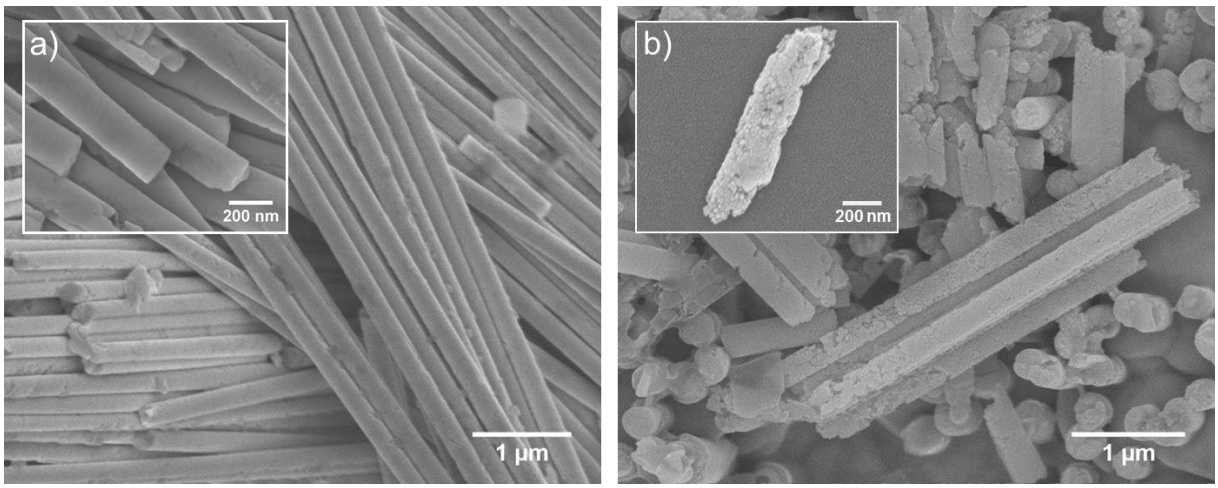

Figure 21: SEM images of ZnO wires with a) smooth and b) rough morphology, grown at temperature of 80˚C and potential of -0.8 V vs. Ag/AgCl using 0.1 and 1 M $Zn(NO_3)_2 \cdot 6H_2O$ electrolytes, respectively.

4.1.4. Influence of the applied potential on the morphology and texture of the wires

To study the influence of the electrodeposition potential on the morphology and crystallinity of the nanowires, series of identically etched ion-track membranes with channel diameter of 250 nm and Cu back-electrodes were prepared. Potentials between -0.5 and -0.8 V vs. Ag/AgCl were applied using a 0.1 M $Zn(NO_3)_2 \cdot 6H_2O$ electrolyte at 80˚C. Cyclic voltammetry previously performed using similar membranes with a Cu back-electrode, applying negative potentials from 0 to -2 V vs. Ag/AgCl at a scan rate of 10 mV/s, revealed a reduction peak at -0.8 V, which was assigned to the reduction of NO_3^-.[130] The chosen applied

potentials are thus less negative than the reduction peak. Figure 22a shows representative chronoamperometric (*I-t*) curves of three electrodeposition processes at applied potentials of -0.5, -0.7, and -0.8 V. The deposition current increases with the increase of applied potential, which is a related to a larger amount of deposited charge.[87] At various potentials different ratios of Zn^{2+} and OH^{-} ions are produced: higher potentials lead to the creation of more ions, so in this case more charge is deposited on the same area of the working electrode than in the case of lower potential.

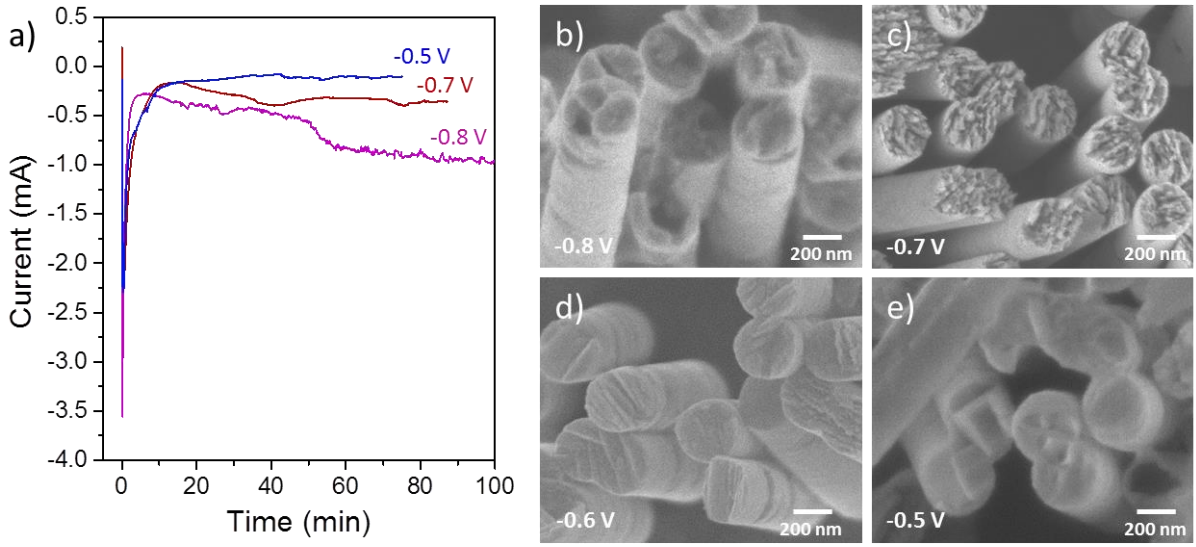

Figure 22: a) Chronoamperometric curves of electrodeposition of ZnO nanowire arrays at applied potentials of -0.5 (blue), -0.7 (red) and -0.8 (purple) V vs. Ag/AgCl at 80˚C; SEM images (top view) of nanowires with 250 nm diameter synthesized at different potentials of b) -0.8 V, c) -0.7 V, d) -0.6 V, and e) -0.5 V vs. Ag/AgCl.

Figure 22 (b-e) show top views of four nanowire samples deposited at a potential of -0.8 V (a), -0.7 V (b), -0.6 V (c), and -0.5 V (d) vs. Ag/AgCl. The images indicate a clear change in wire morphology depending on the applied potential. Nanowires deposited at -0.8 V display tips with a poorly defined shape, whereas the tips of the wires deposited at -0.7 V exhibit small spike-like grains. At a potential of -0.6 V, the tips show platelet like grains parallel to the surface normal indicating a possible change of crystal orientation. Wires deposited at -0.5 V display tips which look smoother and seem to consist of larger grains. The different tip morphologies are an indication that the applied voltage has an influence on the grain size and crystallographic structure of the wires.

Furthermore, the crystallographic orientation of the nanowire arrays deposited at various potentials was investigated by XRD. Figure 23a displays the XRD patterns normalized to the $(10\bar{1}0)$ reflection. At 2θ values of 31.74˚, 34.44˚, 36.23˚, and 56.58˚, respective reflections of the $(10\bar{1}0)$, (0002), $(10\bar{1}1)$, and $(11\bar{2}0)$ planes were observed, corresponding to known values of hexagonal wurtzite ZnO with cell constants of a = 3.24 Å and c = 5.19 Å. All samples show the presence of several ZnO reflections indicating that the nanowires are either polycrystalline, i.e. each wire consists of grains with different orientations or the array

consists of single crystalline nanowires where each wire has a different orientation. No reflections at higher Bragg angles were detected. Neither pure Zn nor any impurities were found. The two intensive peaks at 43.34° and 50.45° belong to the Cu (111) and Cu (200) reflections from the back-electrode. The Au (111) reflection at 38.19° originates from the sputtered Au layer.

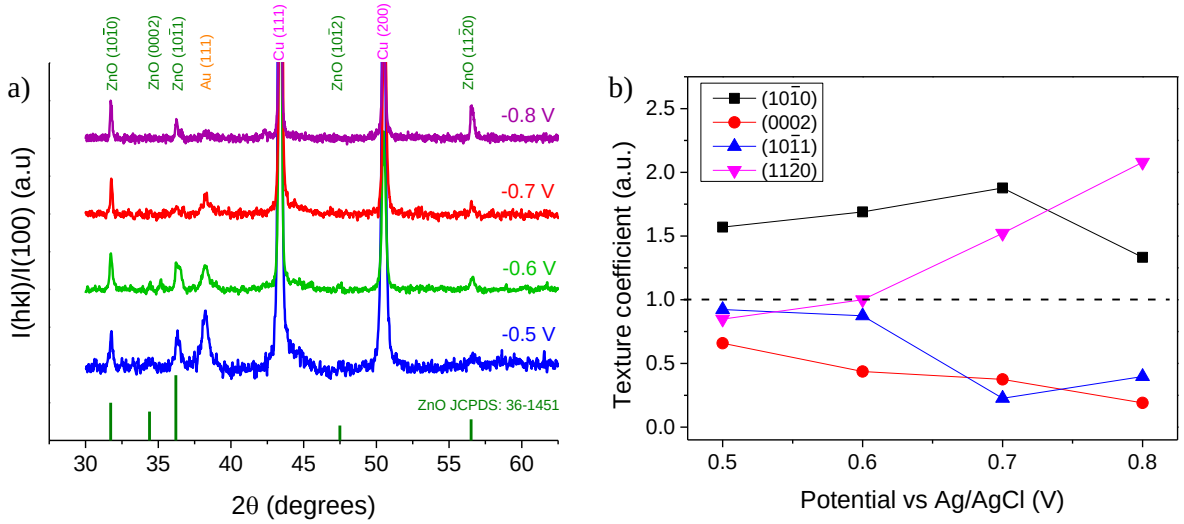

Figure 23: a) Normalized XRD patterns of ~250 nm ZnO nanowire arrays deposited at -0.8 V (purple), -0.7 V (red), -0.6 V (green), and -0.5 V (blue) vs. Ag/AgCl. The bars in green correspond to the values from JCPDS card Nr. 36-1451; b) corresponding texture coefficients of the $(10\bar{1}0)$ (black), (0002) (red), $(10\bar{1}1)$ (blue), and $(11\bar{2}0)$ (pink) reflections.

Compared to the ZnO reflections expected for diffraction of a standard polycrystalline powder (JCPDS 36-1451, vertical lines in Figure 23a), all spectra exhibited an enhanced ZnO $(10\bar{1}0)$ reflection. This is in contrast to most electrodeposited ZnO films and nanowires reported in literature, where the growth perpendicular to the (0002) planes is more favorable.[47,48] For these nanowire arrays, the relative intensities of the (0002) and $(10\bar{1}1)$ reflections decrease and the intensity of the $(11\bar{2}0)$ reflections increases with the increase of the applied potential. This may indicate that at higher voltages more $(11\bar{2}0)$ planes are formed, while at lower voltages the growth of $(10\bar{1}1)$ planes predominates. This effect can also be related to the different morphology of the wire tips shown in Figure 22.

To investigate the preferred orientation of the nanowire arrays, the texture coefficients (TC) of given (hkl) planes for all relevant orientations were calculated using the following equation,

$$TC(hkl) = \frac{\frac{I_{nw}(hkl)}{I_0(hkl)}}{\frac{1}{n}\sum_{i=1}^{n}\frac{I_{nw,i}(hkl)}{I_{0,i}(hkl)}}, \qquad (13)$$

where n is the number of peaks (here n=4), $I_{nw}(hkl)$ is the intensity of the (hkl) reflection measured from the nanowire array (given in Miller indices), and $I_0(hkl)$ is the intensity of the

corresponding peak of a ZnO powder reference. In the case of polycrystalline samples, TC is one for all $(hkl)_i$ planes, whereas TC > 1 indicates a preferential orientation of the grains in the sample, and TC = n would mean that the structure is single crystalline. The calculated texture coefficients are shown in Figure 23b. The texture coefficients of $(10\bar{1}0)$ planes increase from ~1.6 to ~1.9 for the nanowire arrays deposited at potentials between -0.5 and -0.7 V, and decreases to ~1.3 for U = -0.8 V. The TC values above one for the $(10\bar{1}0)$ planes indicate that the preferred orientation is set perpendicular to the wire axis. The values in Figure 23b also reveal an increase of the TC $(11\bar{2}0)$ at more negative potentials for all samples. In particular, for nanowires prepared at -0.8 V, the increase of TC $(11\bar{2}0)$ is accompanied by a small decrease of TC $(10\bar{1}0)$. Moreover, for nanowire arrays deposited at higher potentials, the TCs of the (0002) and $(10\bar{1}1)$ planes diminish. However, given that n = 4, the samples do not exhibit a strong texture, but rather the presence of crystals oriented with various directions, and a moderate $(10\bar{1}0)$ preferred orientation ($(11\bar{2}0)$ for U = -0.8V).

4.1.5. Relation between nanowire diameter and crystallographic properties

In order to investigate how the diameter of nanochannels in the membrane influences the crystallographic orientation of the wires, series of PC membranes with nanochannel diameters of 45, 65, 85, 110, and 160 nm and Au back-electrodes were fabricated and used as templates for the electrodeposition of ZnO. First, potentials ranging between -0.5 and -0.8 V at 80˚C from 0.1 M $Zn(NO_3)_2 \cdot 6H_2O$) were applied. Successful growth was observed for membranes with a pore diameter of 160 nm at -0.8 V vs. Ag/AgCl whereas no effective deposition occurred for smaller diameters at none of between -0.5 and -0.8 V. The filling in these small pores was either very poor or missing. Therefore a more negative potential as compared to the wires discussed above was applied. Efficient depositions were performed at -1 V vs. Ag/AgCl for all membranes with pore diameters between 45 and 160 nm. The need for a higher deposition potential can be due to limited diffusion and/or mass/charge transport processes. When the diameter is decreased, the aspect ratio of the pores increases. Because the metal ion concentration in the electrolyte is relatively low (0.1 M $Zn(NO_3)_2 \cdot 6H_2O$), diffusion limitation results in a higher resistance of the electrolyte in the pores, and thus a higher electric driving force is needed for efficient deposition. It is also worth mentioning, that this set of samples had a Au substrate, while the wires mentioned in Section 4.1.4 were deposited on Cu substrate, which might also influence the nucleation and growth of ZnO, however for this assumption no proof is available yet.

The chronoamperometric curves of the set of samples with different diameters are shown in Figure 24. The constant potential (-1 V vs. Ag/AgCl) was applied for 1, 2, 3, 4, and 5 h for membranes with a pore diameter of 160, 110, 85, 65, and 45 nm, respectively. The time was chosen according to the diameter on the one hand to avoid overgrowth and formation of caps, and on the other hand to fill the pores with sufficient amount of material for XRD analysis. As the diameter of the pores and hence the effective area of the working electrode is decreasing,

the absolute value of the current is also decreasing, although the current density should remain the same for all samples.

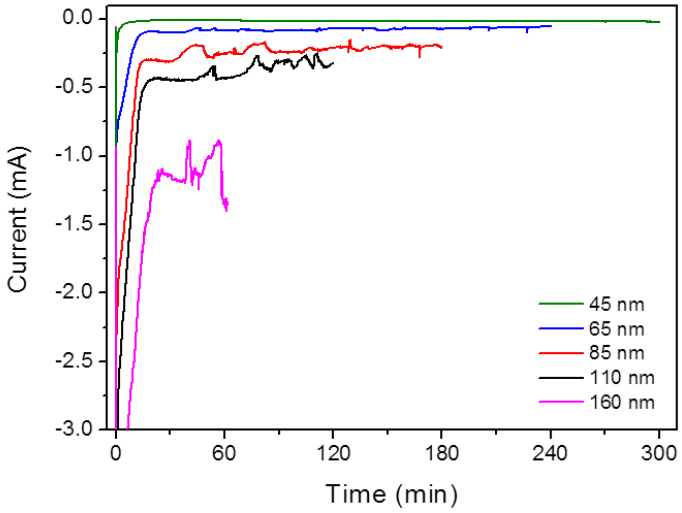

Figure 24: Chronoamperometric curves of ZnO nanowire electrodeposition in membranes with diameters of 45 nm (green), 65 nm (blue), 85 nm (red), 110 nm (black), and 160 nm (pink). The deposition was carried out using 0.1 M $Zn(NO_3)_2 \cdot 6H_2O$ electrolyte at a constant potential of -1 V vs. Ag/AgCl at 80˚C.

To analyze the nanowires by SEM, the polymer matrix was removed with dichloromethane. The detailed processes of the sample cleaning and preparation for measurements are described in Chapter 2. Nanowires transferred onto Si wafers were analyzed individually with respect to their morphology and diameter. The mean diameter and the standard deviation of ~50 individual nanowires from different parts of the same sample were determined. The dependence of the average diameter on etching time is shown in Figure 25a. The error bars represent the standard deviation values. The diameter values of pores and wires are in good agreement and in both cases show a linear dependence on the etching time between 1.5 and 4.5 min. However, as it was observed earlier, the diameter values measured for the channels are slightly (6±1 nm) smaller than the diameters measured for the wires grown in the pores.[80] This small difference is attributed to the thin (~8 nm) Au layer that was sputtered on the polymer surface for SEM investigations, slightly reducing the pores size by a few nm. Figure 25 (b-f) display nanowires with an average diameter of 160±6, 110±4, 85±6.6, 65±4 and 45±1.5 nm, respectively. All analyzed wires exhibit a relatively rough morphology resembling voids, but no clear dependence between the morphology and wire diameter was observed. Since it is known from deposition of different kind of materials that the walls of the pores in the polymer membrane are smooth, the roughness is ascribed to the high deposition rate of wires.[43] EDX analysis of single nanowires (area and line scans) showed the presence of zinc and oxygen in a ratio close to 1:1, and the absence of any impurities. A representative line scan is included in Figure 25b (inset). The Si signal originated from the substrate.

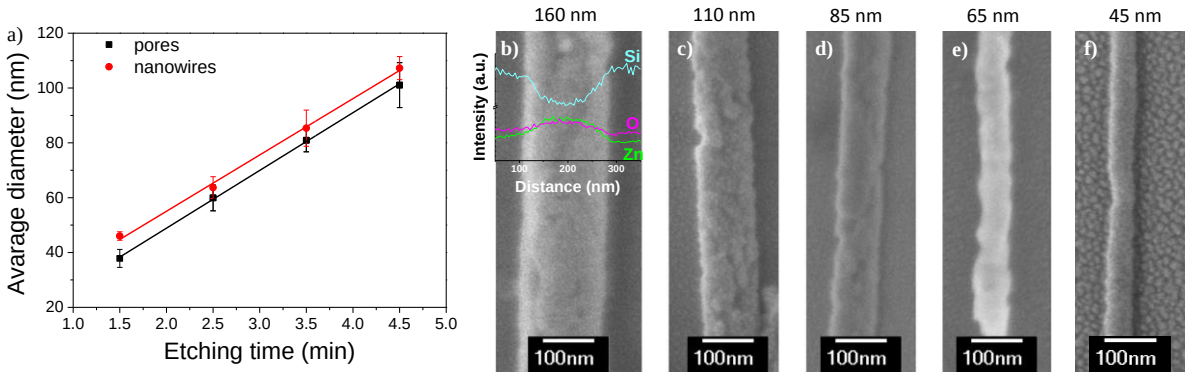

Figure 25: a) Average diameter measured by SEM for pores (black) and wires (red) as a function of etching time. Individual nanowires with an average diameter of b) 160, c) 110, d) 85, e) 65, and f) 45 nm on Si wafers. Inset in (b) shows a representative EDX line scan.

For XRD characterization the nanowires were kept embedded inside the membranes. The XRD patterns measured on these samples are presented in Figure 26a. The diffractograms are normalized to the $(10\bar{1}0)$ reflections. Four ZnO reflections corresponding to the wurtzite phase, namely $(10\bar{1}0)$, (0002), $(10\bar{1}1)$ and $(11\bar{2}0)$ were observed, whose relative intensities varied for the different samples. The mentioned reflections are stronger pronounced for the wires with smaller diameters, namely 45 and 65 nm, and slightly for 85 nm wires. For nanowire arrays with wire diameter of 110 and 160 nm the reflections (0002) and $(10\bar{1}1)$ are almost negligible. However, for TC calculations all 4 reflections were taken into account for a comparison of all samples. These patterns can also explain the morphology difference of the wires. Apparently, wires with smaller diameters tend to be more polycrystalline, which means that the random growth of the crystals can result in the formation of voids and rough surfaces, as it was shown in Figure 25. The two high-intensity peaks at 38.19° and 44.39° belong to the Au reflections originating from the back-electrode. The XRD spectra confirm that the nanowires are pure ZnO and that there is no Zn co-deposition under the applied conditions. The calculated TC data are presented in Figure 26b. The array of nanowires with the largest diameter, namely 160 nm, displays the highest texture, i.e. TC $(10\bar{1}0)$ with a maximum TC value of 2.5. The texture coefficient for this preferred $(10\bar{1}0)$ orientation decreases for smaller wire diameters, while the TC value for the $(11\bar{2}0)$ orientation increases slightly for 85 and 110 nm wires, and decreases again for thinner nanowires. In contrast, for diameters below 80 nm the TC (0002) slightly increases. The tendency for having a preferred orientation and better crystallinity is higher for thicker wires, while the thinner nanowires have no defined preference of a certain orientation.

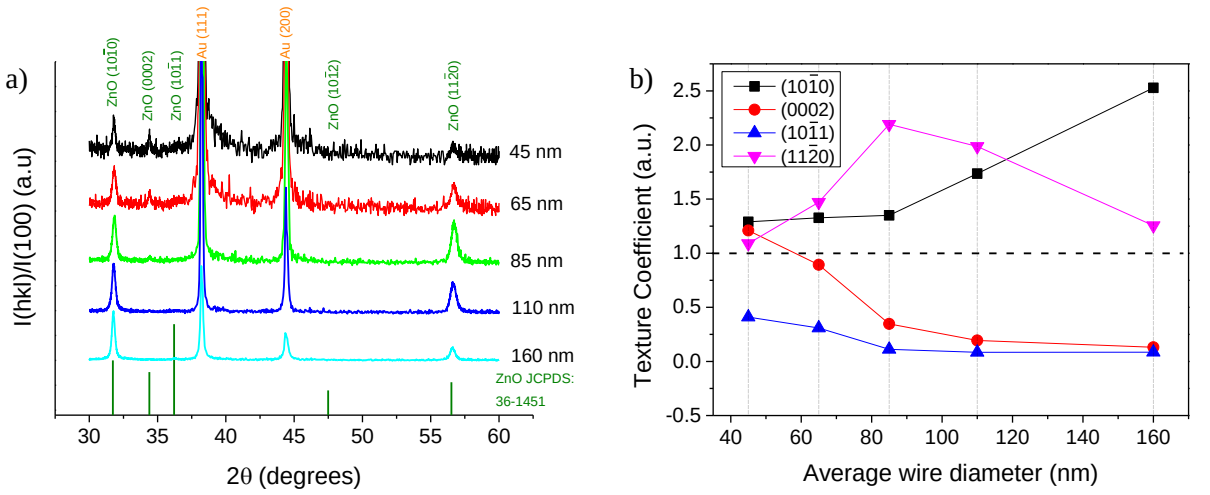

Figure 26: a) XRD diffractograms measured for arrays of nanowires with diameter of 45 (black), 65 (red), 85 (green), 110 (blue), and 160 nm (cyan) grown at -1 V vs Ag/AgCl, and b) texture coefficients of the $(10\bar{1}0)$ (black), (0002) (red), $(10\bar{1}1)$ (blue), and $(11\bar{2}0)$ (pink) reflections.

4.1.6. Crystallographic properties and composition depending on wire length

ZnO nanowires were grown for 1, 2, and 3.5 h in 30 µm thick membranes with pores having a diameter of 200 nm and a number density of 10^9 cm^{-2}. The electrodeposition was carried out using 0.1 M zinc nitrate hexahydrate electrolyte under a potential of -0.8 V vs. Ag/AgCl at 80˚C. The crystallographic orientations of the nanowire arrays embedded in the membrane were analyzed using XRD. Figure 27a shows the configuration of the sample and measuring setup. The diffractograms measured for the three samples are shown in Figure 27b. In all cases, reflections at 2θ of 31.74˚, 34.44˚, 36.23˚ and 56.58˚were observed, which respectively correspond to the $(10\bar{1}0)$, (0002), $(10\bar{1}1)$ and $(11\bar{2}0)$ planes of hexagonal wurtzite ZnO, matching well with the values available from the ZnO JCPDS card Nr. 36-1451 (shown with black lines in Figure 27b). For all three samples, only these four reflections were present indicating that the crystallinity of the ZnO wires does not change along the nanowire length and does not depend on the deposition time. The reflection marked with an asterisk at the 2θ angle of 38.25˚ is assigned to the Au (111) arising from the sputtered gold layer. The copper signal arises from the electrodeposited back-electrode. Wires produced under identical conditions exhibited very similar XRD spectra confirming the reproducibility.

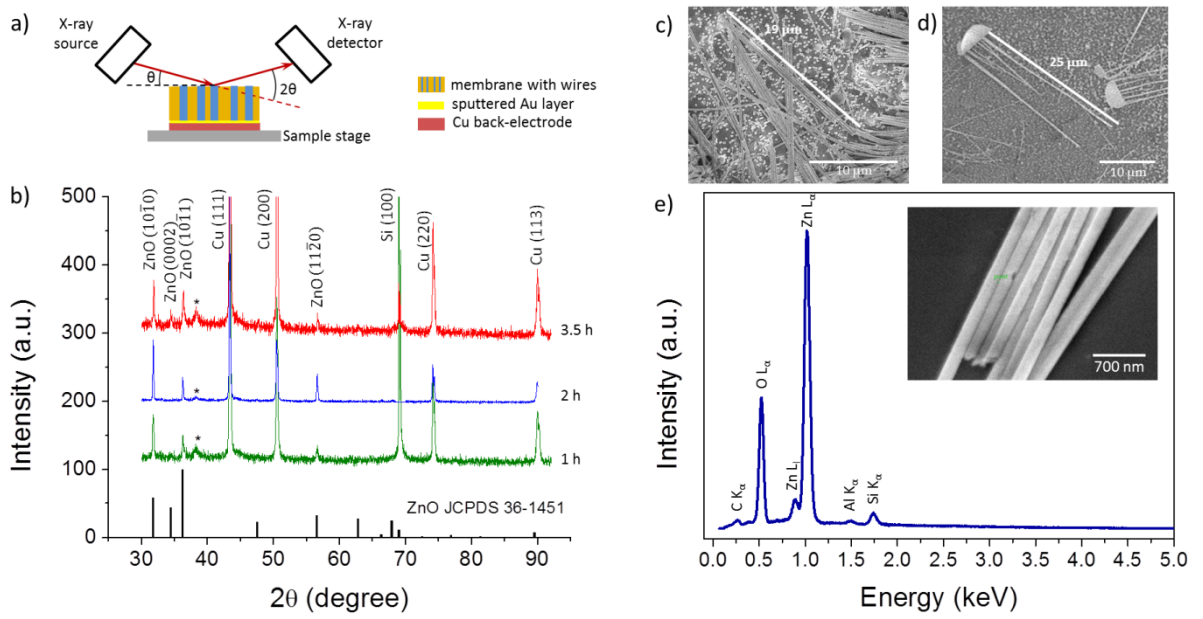

Figure 27: a) Schematic representation of the XRD setup and the adjustment of the sample relative to the X-ray beam, b) XRD diffractograms of ZnO nanowire arrays with wire length of ~10, ~20 and ~30 µm grown at -0.8 V vs. Ag/AgCl and 80°C for 1 h (green), 2 h (blue) and 3.5 h (red) using 0.1 M $Zn(NO_3)_2 \cdot 6H_2O$ electrolyte. The black lines represent the 2θ values known from the ZnO JCPDS card Nr. 36-1451. SEM images of c) ~20 µm and d) ~25 µm long ZnO nanowires. In (d) the wires are still attached to the cap, e) representative EDX spectrum of ZnO nanowires transferred onto a Si wafer (inset).

To measure the length of the wires deposited at different time periods as well as the chemical composition along the wires, the polymer was dissolved in dichloromethane. During polymer dissolution some of the long wires broke and remained lying on the substrate, allowing for measuring their length (Figure 27 c,d). The average lengths for the samples grown for 1, 2 and 3.5 h were 7-10, 18-20 and 27-30 µm, respectively. For the sample grown for 3.5 h, caps were observed on top of several wires (Figure 27d). Wires transferred onto a Si wafer were analyzed by energy dispersive X-ray (EDX) spectrometry. For each wire, three points along the length (two at the edges and one in the middle) were measured. A representative EDX spectrum is shown in Figure 27e. The L lines of Zn and O are assigned to the wires. The K line of C probably originates from residual polymer on top of the wires. The signals from Al and Si correspond to the SEM sample holder and Si wafer, respectively. The inset if Figure 27e shows the SEM image of ZnO wires for which the presented EDX spectrum was recorded. For the majority of the measurements, the ratio of zinc and oxygen in the structures showed a stoichiometry close to 1:1. No other signals were detected, suggesting that the wires consist only of Zn and O, without any significant impurities.

4.1.7. Mechanical stability of the arrays

For implementation of nanowire arrays as electrodes, e.g. for solar cells and/or photoelectrodes for photoelectrochemical water splitting, free-standing wires are required. For the comparison of the mechanical stability of nanowire arrays, three samples were prepared

by electrodeposition of ZnO a -0.8 V vs. Ag/AgCl at 80˚C using 0.1 M $Zn(NO_3)_2 \cdot H_2O$ in templates with pore number density of 10^9 cm^{-2}. The two samples had a similar wire diameter of ~250 nm, but different length being ~7 and ~20 µm. The third sample consisted of wires with diameter of ~125 nm and length of 20 µm. SEM was employed to study the mechanical stability of ZnO nanowire arrays on their metallic substrate after polymer dissolution. Figure 28 (a) and (b) show SEM images of arrays of ZnO nanowires with a diameter of 250 nm and length of ~7 and ~20 µm, respectively. After dissolution of the membrane, the short wires (Figure 28a) are free-standing and have a perfectly parallel alignment, whereas the longer nanowires (Figure 28b) tend to bend and agglomerate forming bunches of nanowires with attached tips. This effect became even more crucial when decreasing the diameter of 20 µm long nanowires to 125 nm (Figure 28c). These wires showed the least stability not only by bending but also by detaching from the back-electrode during the cleaning process. In Figure 28c, the white dots on the substrate are the bases of broken wires.

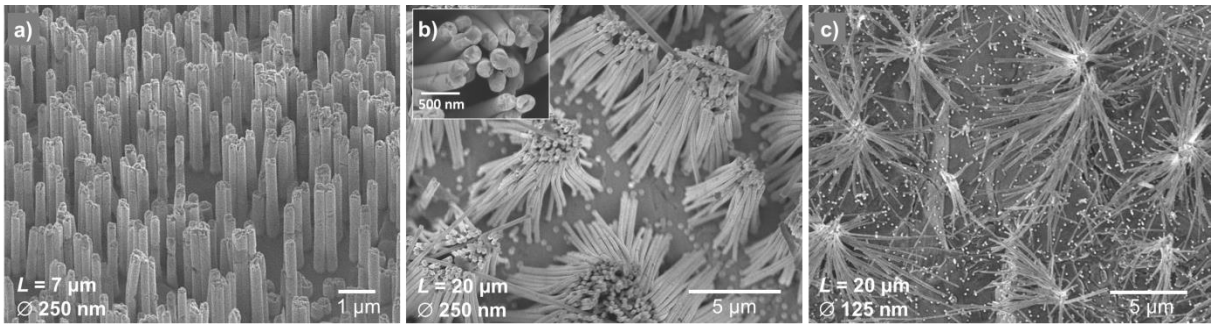

Figure 28: SEM images of a a) ~7 µm long freestanding nanowire array (wire diameter of ~250 nm), b) ~20 µm long nanowires array (diameter ~250 nm), showing low mechanical stability, and c) ~20 µm long nanowire array (diameter ~125 nm), having the poorest mechanical stability.

By increasing the wire diameter and decreasing their length, relatively stable wire array can be obtained. To enhance the stability and maintain the high aspect ratio of the nanowires, conical ZnO wires were studied.

4.2. Vertically aligned conical ZnO wires

For the fabrication of conical nanowires, asymmetrically etched 30 µm thick membranes with 10^7 pores/cm^2 were employed. As for cylindrical pores, also in this case the membranes were first sputtered with a thin gold layer which was reinforced with an electrodeposited Cu layer. The potentiostatic growth of ZnO cones was carried out using the same setup and electrolyte as for the cylindrical nanowires with largest pores (~200 - 250 nm), namely 0.1 M $Zn(NO_3)_2 \cdot 6H_2O$, applying a constant potential of -0.8 V vs. Ag/AgCl at a temperature of 80˚C. Two different approaches of the growth process were employed: base-to-tip and tip-to-base* growth.[128] In the first case, the back-electrode was deposited on the side of membrane with the large diameter (2 - 2.5 µm) of the conical pores (referred to as base) for ~1.5 h. This

* The tip-to-base approach was proposed by Dr. Loïc Burr and is discussed in more details in [128].

resulted in a Cu layer thickness of ~12 - 15 µm, which was expected to completely close the pores. For the growth of the conical wires inside such membranes, the samples were placed in the electrochemical cell in between Teflon compartments in such a way that the open side of the conical pores with diameters below 100 nm (tips) was in contact with the $Zn(NO_3)_2 \cdot 6H_2O$ electrolyte (Figure 29a). In the case of the tip-to-base growth, the back-electrode was deposited on the membrane at the side where the tips were, and the electrolyte for the ZnO deposition entered into the pores from the base of the conical pores. The latter arrangement provided a faster filling and wetting and improved the ion diffusion inside the pores (Figure 29b).

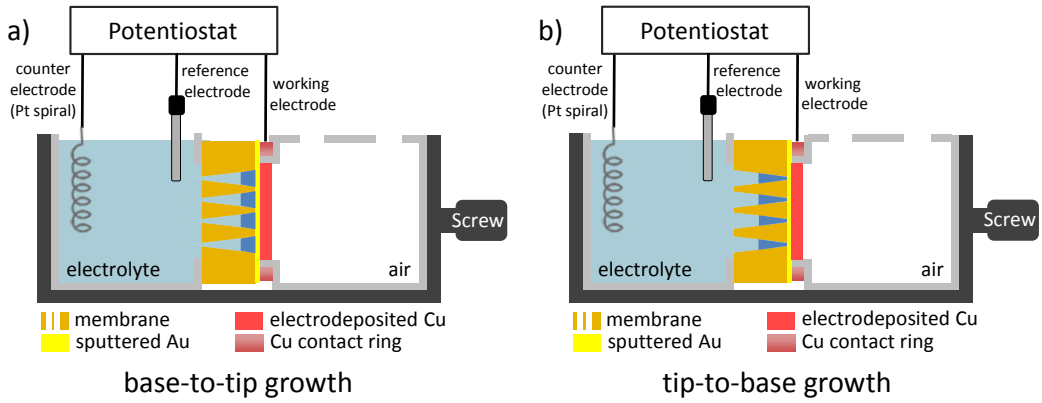

Figure 29: Schematic representations of the three-electrode setup for electrodeposition of conical ZnO nanowires with a) base-to-tip and b) tip-to-base approaches.

ZnO conical nanowire arrays were analyzed by SEM to determine the size of the base and tip, as well as to study their surface morphology. Figure 30 shows SEM images of nanocones deposited by the base-to-tip method. Figure 30 (a) and (b) show low and high magnification SEM images of a cone array on a substrate. At first sight, the cones look smooth with homogeneously grown walls. However, some of the cones exhibited a hollow structure near the base (marked with arrows in Figure 30b) which is typical for metals and metal oxides electrodeposited at a constant potential in pores of sizes larger than a few hundred nm.[46,131] The hollow bases of the cones weaken their mechanical stability and lead to their breaking. However, broken wires lying on the substrate allow measuring the diameter and length of the cones (Figure 30c). Systematic analysis of different samples with identical preparation conditions yielded tip diameters in the range between 70 and 90 nm (Figure 30d). The diameter of the base close to the back-electrode was between 2 and 2.5 µm. The length of the cones after complete filling of the membrane was in the range between 25 and 27 µm. For all measured cones, the base diameter at the point where the cone broke was between 1.2 and 1.9 µm (Figure 30e). The zone where the wires typically broke was found to be ~5 µm away from the back-electrode. The hollow structure continued for the majority of the cones until the diameter of the conical channels in the membranes decreased to ~1 µm or less (up to a cone length of ~15 µm). The schematic representation of the tubular structure of the cones is shown in Figure 30f. The formation of a tubular-shaped base of the cone results from the deposition

of the gold back electrode by sputtering. During this step the sputtered gold not only covers the surface of the membrane but it partly enters and coats the walls of the pores with a depth of up to several hundreds of nm. This coated area serves as a first nucleation center for electrodeposition, and the deposited material replicates the geometry of the sputtered Au tube at the base resulting in a further growth of ZnO tubular cones.

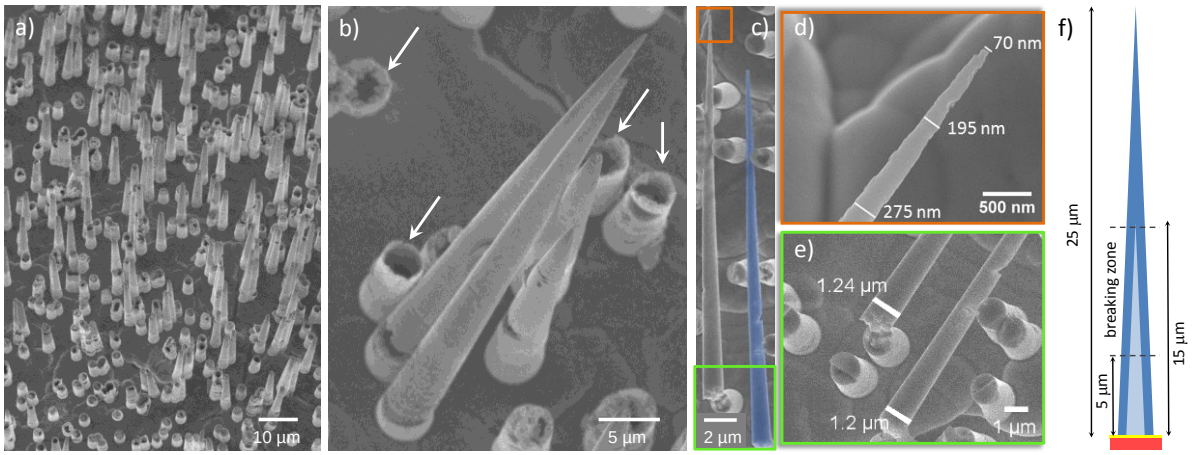

Figure 30: SEM images of a ZnO conical nanowire array in low (a) and high (b) magnification showing free-standing and broken cones, c-e) 23 µm long individual ZnO conical nanowires with a tip diameter varying between 70 and 90 nm and a base diameter at the breaking point being ~1.2 µm, f) schematic representation of the tubular structure of a cone with a breaking zone at a length between 5 and 15 µm.

The crystallographic orientation of ZnO nanocone arrays embedded in the PC membrane was investigated using XRD. Figure 31a displays a representative XRD pattern measured on ZnO conical wires with ~2 µm base and ~90 nm tip diameters. The spectrum shows the reflections at 2θ values of 31.76˚, 34.38˚, 36.27˚, 47.44˚, 56.43˚, 62.63˚, 67.88˚ and 68.99˚ which correspond to the $(10\bar{1}0)$, (0002), $(10\bar{1}1)$, $(10\bar{1}2)$, $(11\bar{2}0)$, $(10\bar{1}3)$, $(11\bar{2}2)$, and $(20\bar{2}1)$ planes of wurtzite ZnO. The presence of almost all possible crystallographic planes indicates that these cones are polycrystalline. The small reflection at 38.12˚ belongs to Au (111) and originates from the thin sputtered gold layer. The signals at 43.34˚ and 50.47˚ are assigned to the Cu substrate and correspond to the (111) and (200) planes. The vertical lines shown in the graph correspond to the values known from the JCPDS cards of ZnO (green, No. 36-1451), Cu (purple, No. 04-0836) and Au (yellow, No. 89-3697). Figure 31b shows the alignment of the sample relative to the X-ray beam. A schematic of ZnO hexagon together with the main crystallographic orientations and several planes which are present in nanocones are shown in Figure 31c.

To better understand the significant difference of the crystallographic structure of cones as compared to cylindrical wires, namely the presence of almost all reflections typical for ZnO powder, a closer look was taken at the hollow structure of these cones by investigating them with SEM. The typical morphologies of the inner structure of cones observed on the same sample are presented in Figure 32.

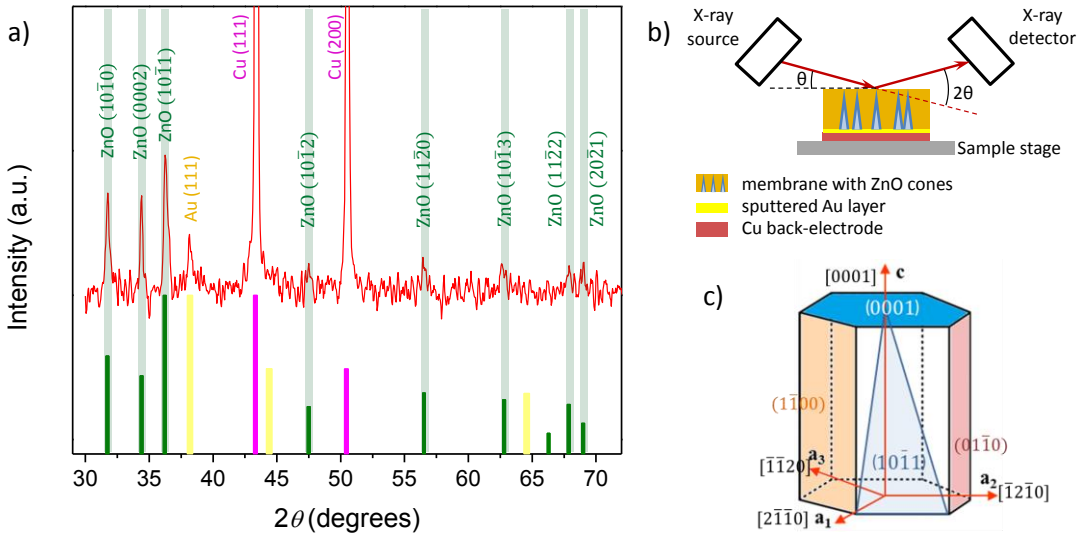

Figure 31: a) XRD pattern of a conical nanowire array grown from base to tip, and schematic representations of b) the XRD setup and the adjustment of the sample relative to the X-ray beam and c) the ZnO hexagonal crystal with marked crystallographic orientations and several planes which are commonly present in the ZnO wurtzite phase.

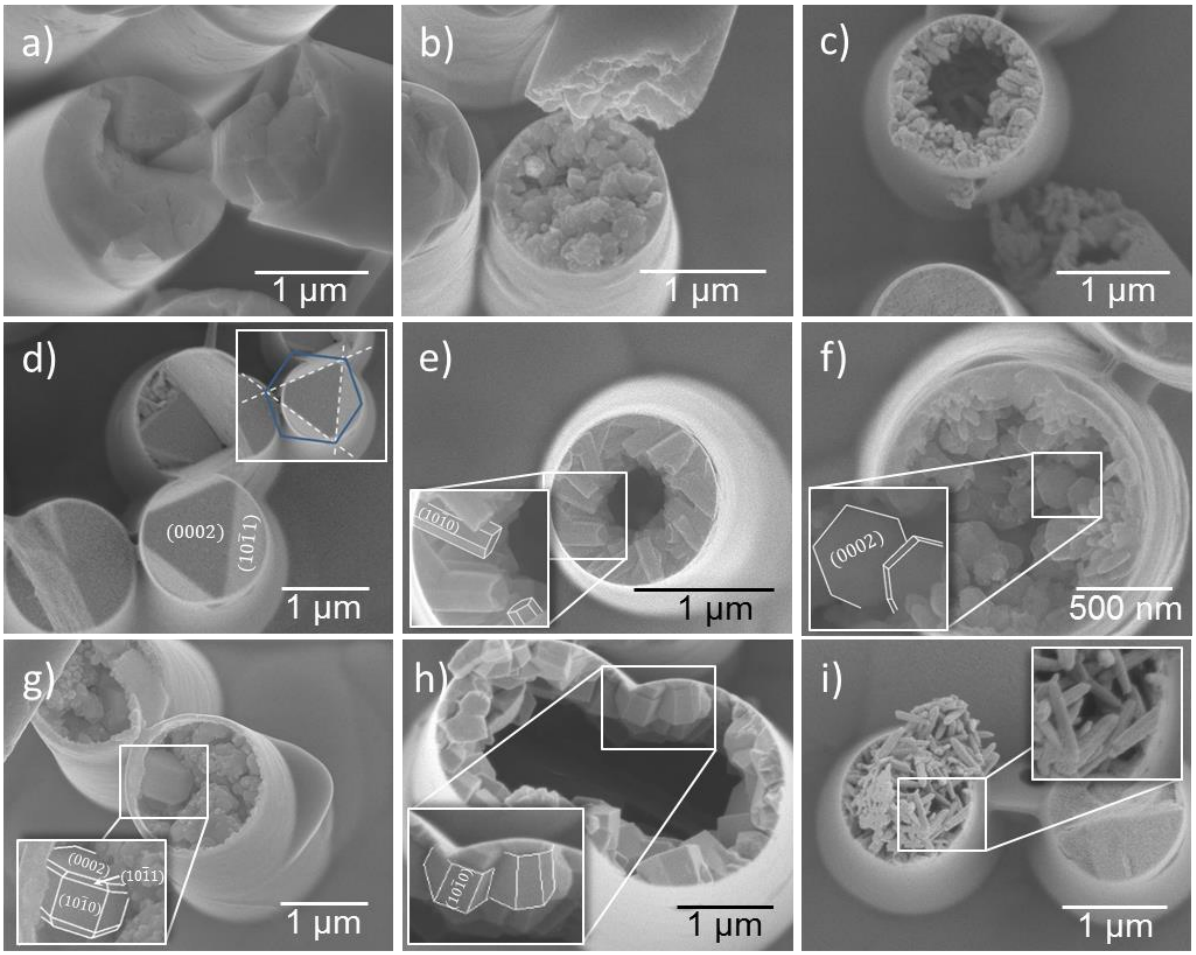

Figure 32: SEM images of typical morphologies of the inner structure of cones observed on the same sample electrodeposited at -0.8 V vs. Ag/AgCl at 80˚C from base to tip, revealing the individual nature of the growth and crystallization of ZnO inside different channels of the same membrane.

The breaking points of several cones of the same sample are shown in Figure 32a-c. In all cases, the inner structure looks completely different. In Figure 32a the broken cone obviously consists of large, faceted grains which can be detected at the breaking point from both edges of the cone. Figure 32b shows another broken cone with a completely filled base. However, in this case, the cone consists of features with a smaller size and undefined shape. A tubular cone consisting of an inner nanorod-based wall and a smooth outer wall is shown in Figure 32c. The wall of the tube, which was formed by non-uniform nanorods, had a thickness of ~400 nm at the point where the cone broke. A very typical structure that was observed for many cones is shown in Figure 32d. Here, the bases of the cones are almost completely filled and consist of very large grains having (0002) and $\{10\bar{1}1\}$ conspicuous facets. The inset in this image shows the top view of the hexagon (0002) plane (in blue) and the $\{10\bar{1}1\}$ planes (with dashed lines). Another hexagonal structure observed inside the cones was a hexagonal tube (Figure 32e). These tubes, which had a length varying between 200 and 300 nm and diameter between 100 and 150 nm (mainly with a 2:1 aspect ratio), formed the inner wall of the tubular base of the cone and were oriented randomly with respect to each other but parallel to the substrate. These structures are expected to have a strong reflection of $\{10\bar{1}0\}$ family planes in the XRD pattern. Some other cones were filled with non-uniform short nanorods and small hexagons, as shown in Figure 32f. Since these hexagons looked to be nicely positioned perpendicular to the wire growth axis, an enhancement of the (0002) reflection signal during XRD measurement can arise also from these structures. The mentioned three main reflections may be due to the structures shown in Figure 32g, where the cone was filled with grains consisting of all three planes. Solid hexagons forming a conical tube are shown in Figure 32h. In this case, the hexagons exhibited very diverse sizes and were oriented randomly. Last but not least, another common structure, which is shown in Figure 32i, was a cone filled with uniform nanorods with a length of ~400 nm and a diameter of ~70 nm.

Such a large variety of cone-shapes made the complete array of the cones (grown from base to tip) behave as a polycrystalline system. The non-homogeneity of the growth, which can be a result of poor diffusion and wetting processes through the small opening of the conical pores, leads to a rather poor mechanical stability. For this reason, the synthesis proves was inverted by growing the ZnO cones from tip to base. The applied conditions, namely the temperature, electrolyte and the potential were the same as for the cones grown from base to tip. A typical XRD pattern of a tip-to-base grown cone array embedded in the membrane is shown in Figure 33a. As in the previous case, these cones also see to be polycrystalline with prominent $(10\bar{1}0)$, (0002) and $(10\bar{1}1)$ and relatively lower $(10\bar{1}2)$, $(11\bar{2}0)$, and $(10\bar{1}3)$ reflections. The main difference compared to the base-to-tip grown samples is the dominating (0002) reflection instead of $(10\bar{1}1)$. No signal was detected from the planes of ZnO at higher Bragg

angles. The inset in Figure 33a shows the schematic of the XRD setup and the alignment of the membrane with cones relative to the X-ray beam.

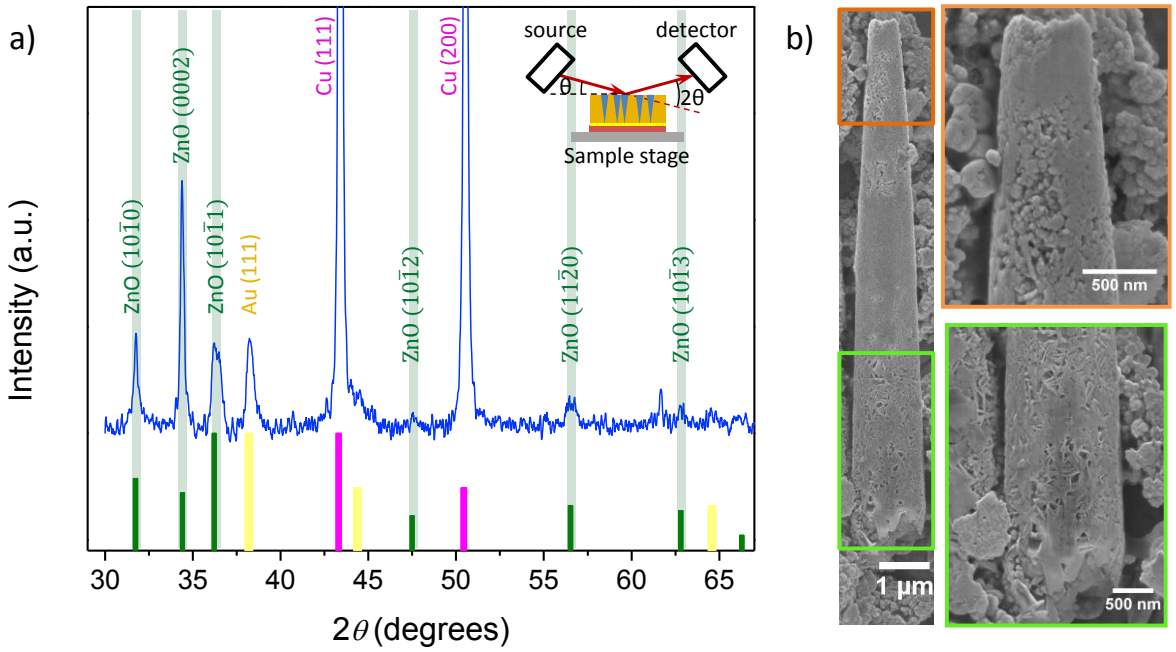

Figure 33: a) XRD pattern of a conical nanowire array grown from tip to base, the inset shows the schematic representation of the XRD setup and the alignment of the sample relative to the X-ray beam, b) SEM images of a typical ZnO cone grown from tip to base, the highlighted zoomed-in images show the edges of the cone close to the tip (orange) and base (green).

The SEM image of a typical cone grown from tip to base is shown in Figure 33b. The zoomed in images of the two edges of the cone close to the tip (orange) and the base (green) show a very rough morphology. The wires consist of arbitrarily oriented grains and nanowalls which explains the polycrystalline character revealed by XRD.

To measure the tip and base diameters, individual cones were analyzed with SEM. These cones were mechanically very unstable and tended to fragment onto pieces with a length between 5 and 15 µm (Figure 34a), thereby making it impossible to measure the diameters accurately. However, a closer look at these wires allowed the study of their morphology. Figure 34b shows a high magnification SEM image of two cones which consist of randomly oriented flakes, while the cone in Figure 34c is mainly composed of very small sized features resulting in a very rough morphology. Figure 34d shows the edge of a cone closer to the base. The inset clearly reveals small hexagonal plates „building“ the complete cone. However, it was unexpected that this vast amount of hexagons with randomly oriented (0002) planes could increase the reflection of the corresponding peak in the XRD pattern. Since XRD measurements were performed on the cones still embedded in the membranes, the top view of the membrane with the cones inside was also studied. SEM images are shown in Figure 34 (e-g). Some of the wires developed caps while the surrounding pores remained not completely filled (Figure 34e). The diffusing ions might preferentially reduce on the caps rather than in

the pores. This means that the faster diffusion of ions from the electrolyte into the pores through the large opening of the cone (compared to the base-to-tip growth) does not improve the homogeneity of these cones. Instead, due to the availability of a higher concentration of ions, a faster and preferential growth of hexagonal crystals in the form of caps takes place which spread over the membrane as the wires reach the surface (Figure 34f, g). Some of the hexagons can be single caps themselves, however, the size of the majority of the single hexagons was smaller than the base diameter of the cones, so probably those are extracted from the larger caps. These hexagons detached from the caps lying on the membrane are probably the main reason of the enhanced (0002) signal in the XRD pattern. Figure 34h shows a high resolution SEM image of an individual pore with very inhomogeneous ZnO filling. All SEM images shown in Figure 34 belong to the same sample.

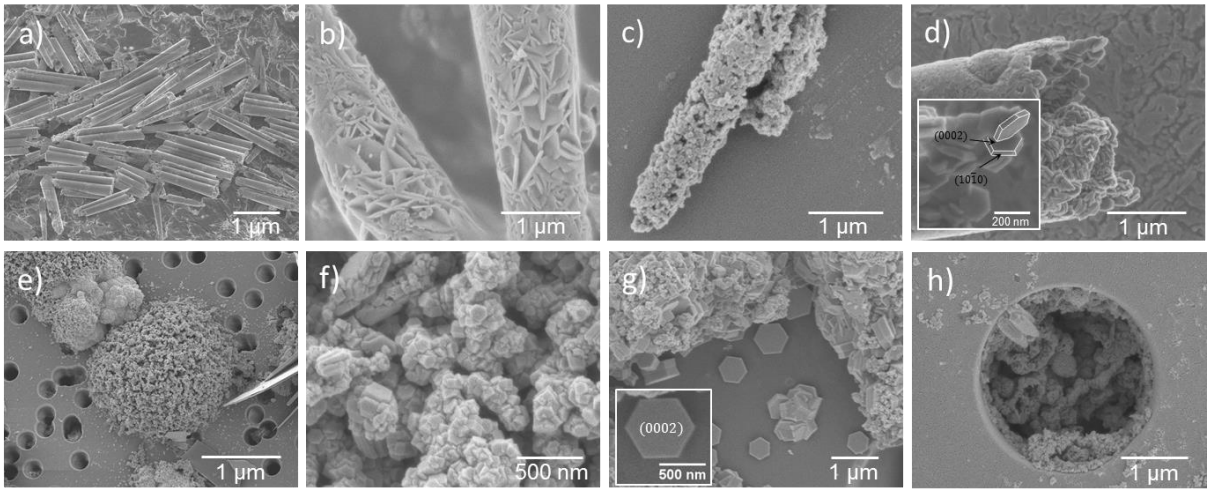

Figure 34: SEM images of a-d) conical nanowires grown from tip to base at -0.8 V vs. Ag/AgCl at 80˚C, consisting of randomly positioned pellets, grainy features and hexagons, e-h) top view of the sample before polymer dissolution showing the membrane with embedded ZnO cones. The overgrowth of the cones resulted in the formation of caps consisting mainly of hexagonal pellets with (0002) orientation.

Conical structures seemed to be promising for the synthesis of mechanically stable nanowire arrays due to the increased diameter of their base serving as a supporting fundament. However, the expectations were met neither for base-to-tip nor for tip-to-base growth method, probably because of the complex wurtzite structure of ZnO. To enhance the mechanical stability of the cones, a reverse tree-like network structure with pre-etched conical pores, as shown in Section 3.3, might be a solution. The network would serve as a reinforced fundament to obtain free-standing cones. Another alternative for mechanically stable nanowire-based structures is a network of wires, which is presented in the next section.

4.3. Nanowire networks

Compared to thin films, nanowire arrays possess a significantly higher surface area. Though, there is a limit in the number density given by the overlap of the pores in the membranes due

to the random distribution of the ion tracks. This restricts the further increase of the surface area of nanowire arrays. Alternatively, the length of the wires can be increased by fixing the number density. However, as mentioned for cylindrical and conical nanowire arrays in Sections 4.1.7 and 4.2, the mechanical stability becomes a crucial issue when increasing the length or decreasing the diameter of the wires. This problem was avoided by using of network structures. Because of the complex matrix of the nanochannel networks, the electrodeposition of ZnO inside these templates had to be optimized. The synthesis and characterization of 3D nanowire and nanotube networks are presented in this section.

4.3.1. Optimization of growth conditions for ZnO nanowire networks

For the fabrication of ZnO 3D nanowire networks, symmetrically etched templates with a total nominal pore-density of 2×10^9, 2.5×10^9, 4×10^9, 8×10^9, and 10^{10} cm^{-2} were employed. Throughout this thesis, the total pore density is referred to as the sum of the fluences applied at different irradiation direction, e.g. if the PC foil was irradiated four times with a fluence of 2×10^9 cm^{-2}, the total fluence will be $4\times2\times10^9$ cm^{-2} which is given as 8×10^9 cm^{-2}. After etching, on side of the membranes was first sputtered with a thin gold layer, and then reinforced with either a Cu or a Au layer via electrodeposition (Section 4.1). All deposition conditions employed for the growth of parallel nanowire arrays on a Cu substrate (potential between -0.5 and -0.8, 80˚C) were subsequently applied to grow ZnO in membranes with interconnected nanochannels with pore diameters varying between 150 and 300 nm. The deposition potential of -0.8 V vs. Ag/AgCl at 80˚C yielded reproducible and homogeneous growth in parallel channels, led to very low filling rates of the interconnected pores with a Cu back-electrode (as shown later in Figure 36a). No filling was observed when more positive potentials were applied. The complex channel geometry obviously has an influence on some of the processes involved in the electrodeposition, for instance, diffusion and/or migration of the Zn^{2+} and OH^- ions inside the pores towards the working electrode.[131] To adjust suitable deposition parameters for homogeneous and reproducible ZnO nanowire network growth, cyclic voltammetry was applied using a 0.1 M electrolyte at 80˚C in membranes with a pore diameter of 220 nm, a density of 2×10^9 pores/cm^2 and a Cu back-electrode. Compared to templates with vertically oriented channels, a shift of the reduction peak to more negative potentials, namely around -1.4 V vs. Ag/AgCl occurred. For nanochannel networks with a Au back-electrode, the reduction peak was close to -1 V vs. Ag/AgCl, as in the case of parallel wires with a Au substrate. Among series of samples electrodeposited at 60, 70, and 80˚C, electrodeposition at 60˚C yielded the best filling for both substrates. Lower temperature resulted in a reduced deposition rate and thus in a more homogeneous filling of the highly interconnected network channels.

Representative chronoamperometric curves for successful electrodepositions in network templates are shown in Figure 35. Both depositions were carried out in identical membranes with a Au substrate and pore diameter and density of 150 nm and 8×10^9 cm^{-2}, respectively.

Also the deposition conditions were the same, namely -1 V vs. Ag/AgCl at temperature of 60˚C. Upon application of the potential, the measured current shows a sharp "peak" within the first few seconds, which is assigned to the charging of the double layer and formation of the diffusion layer, as explained in Section 1.2. Within the following 15 min, a second bread "peak" is recorded. The width of this peak changes from sample to sample, and seems to depend on the pore density. This second peak was never observed for vertical wires and is probably related to the different growth mechanism inside network channels. Mass *et.al*. have reported a similar behavior for the electrodeposition of vertically aligned ZnO wires, explaining the second hump by the independent growth of ZnO nuclei that are smaller than the pore dimensions and the increasing surface area available for the nitrate reduction.[131] After 15 min the curve in Figure 35a continues to oscillate showing several "peaks" with decreasing width as the growth inside the template proceeds. In contrast, the curve shown in Figure 35b stabilizes with time and shows the typical behavior known from the deposition of vertical wires. The oscillation effect was often observed, and might be related to stepwise wetting with the electrolyte and hence with the increase of the nitrate reduction and charge deposition with time.

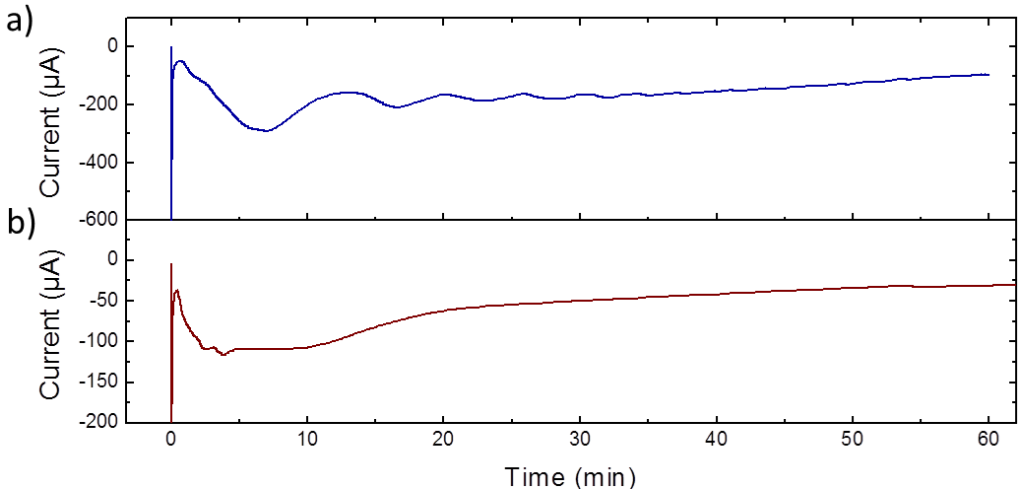

Figure 35: Two types of characteristic chronoamperometric curves of electrodeposition of ZnO in membranes with nanochannel networks with a pore diameter of 150 nm and density of 8×10^9 pores/cm^2, grown at -1 V vs. Ag/AgCl and 60˚C.

To inspect the networks by SEM, the polymer matrix was dissolved in CH_2Cl_2. Figure 36 (a) and (b) show two networks with a nominal wire diameter of 200 nm and density of 2×10^9 cm^{-2} grown on a Cu substrate at different conditions shown in a) U = -0.8 V, T = 80˚C and b) U = -1.4 V, T = 60˚C. The network grown at high temperature (80˚C) and low potential (-0.8 V) looks sparse and incompletely filled, so that the substrate is still visible through the network (Figure 36a). The inset reveals that the wires in the network possess undefined shape probably due to poor filling of the pores. A homogeneous network grown at lower temperature (60˚C) and higher potential (-1.4 V) is shown in Figure 36b.

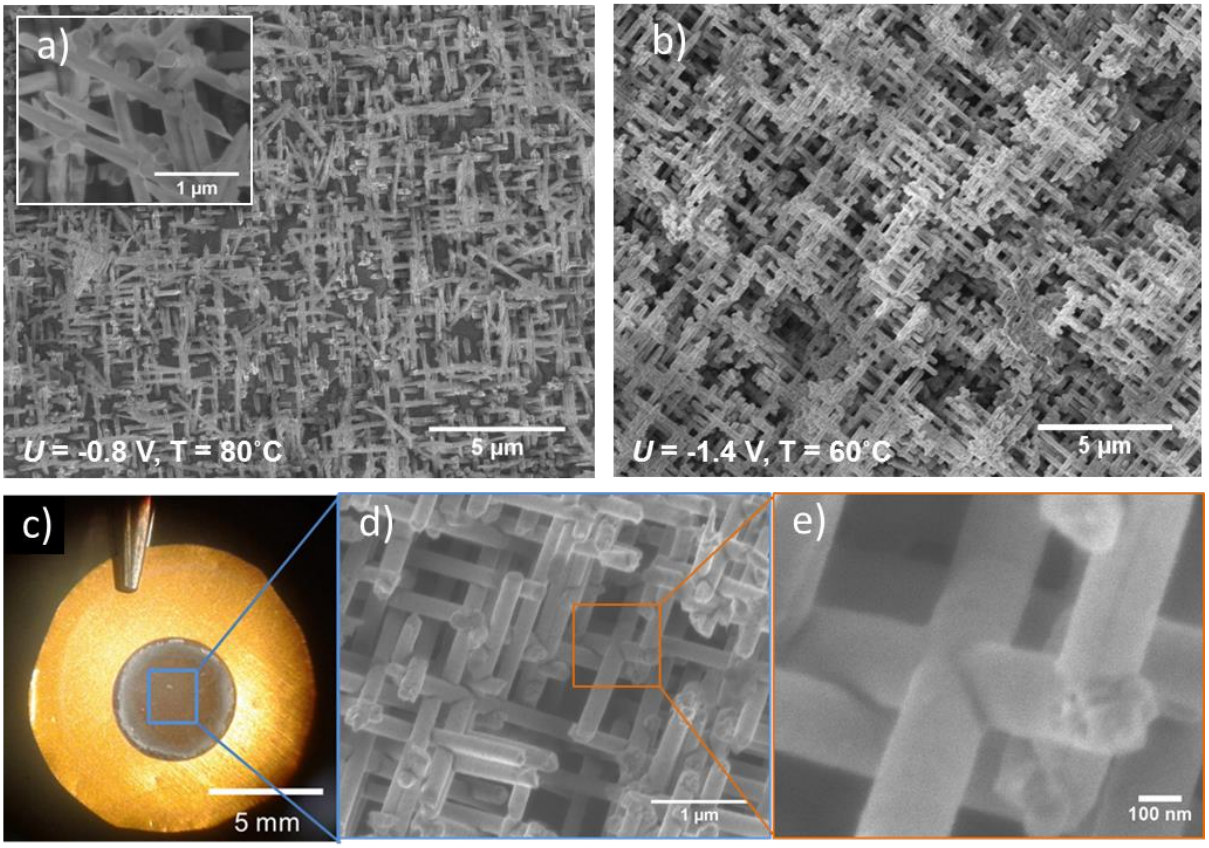

Figure 36: SEM images of two nanowire networks with a nominal wire diameter of 220 nm and density of 2×10^9 wires/cm^{-2}, deposited at different conditions: a) -0.8 V vs. Ag/AgCl at 80˚C, showing sparse filling and poorly shaped wires, b) -1.4 V vs. Ag/AgCl at 60˚C, showing a good filling and well-defined cylindrical wires. c) Photograph of ZnO nanowire network on a Au substrate, with wire diameter of 190 nm and density of 2×10^9 cm^{-2}, grown at -1 V vs. Ag/AgCl and at 60˚C, and the corresponding SEM images of the network at d) low and e) high magnification.[55]

Figure 36c presents a photograph of a ZnO nanowire network on a Au back-electrode after dissolution of the polymer membrane. The sample can be easily handled with tweezers without damaging the network due to its high mechanical stability. The wire density and diameter in the network were in total 2×10^9 cm^{-2} and 190 nm, respectively, and the deposition was carried out at -1 V vs. Ag/AgCl and at 60˚C. The corresponding SEM images in Figure 36 (d) and (e) show this network at low and high magnification, respectively, displaying an excellent interconnectivity between the wires. The connections serve both as points for enhanced mechanical stability of the whole network and as electrical connection between several wires. It is worth mentioning, that this network was deposited in a membrane which was irradiated with a mask where the ion irradiation was limited by a mask to 5 mm in diameter. The role of the mask is to limit the network area and to avoid leakage of electrolyte through the network pores at the edges of the membrane where no back-electrode is deposited. To explain this principle, Figure 37 shows the schematic of two cells with membranes irradiated without (a) and with (b) a mask with a 5 mm aperture in the center. The regions marked with R correspond to areas of possible leakage through the pores at the

interface of the sample and the copper contact-ring. The leakage of electrolyte is observed for membranes irradiated without mask (a), while it is not possible for case (b) since all pores are confined by the back-electrode. Another disadvantage of using the network templates without mask irradiation is that the wires are being deposited outside of the area defined by the opening (diameter) of the Teflon cell, whereas for the samples irradiated with mask the active area of the nanowire network after deposition is defined by the diameter of the irradiation mask. Figure 37 (c) and (d) show photographs of etched membranes irradiated without and with 5 mm mask, respectively. Alternative to mask irradiation, the electrochemical cell can be redesigned. However, this would cause more technical issues, e.g. providing a homogeneous temperature in the solution bath.

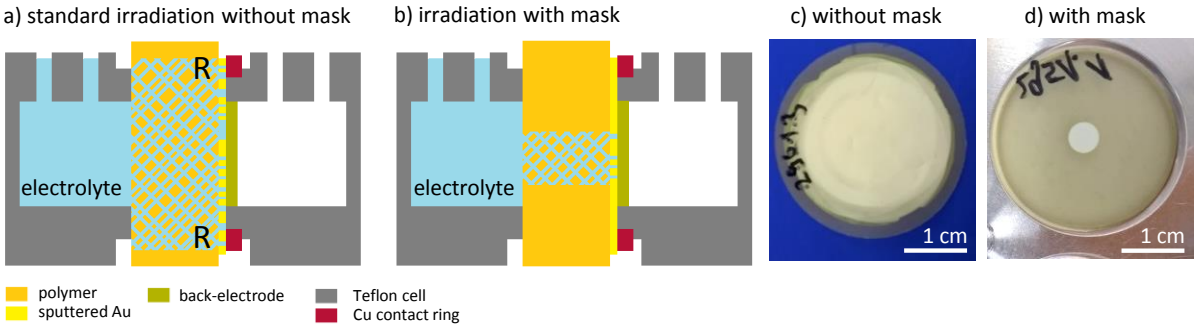

Figure 37: (a, b) Schematic representation of two electrodeposition cells with membranes irradiated a) without and b) with mask. The areas marked with "R" are the regions where the electrolyte can leak thought the pores. Photographs of etched membranes irradiated c) without and d) with 5 mm mask.

The optimization of the wire density in the networks for improved mechanical stability is discussed in the next section.

4.3.2. Enhancement of the mechanical stability of the networks

Figure 38 shows two nanowire networks deposited in membranes with a pore diameter of 90 nm and total density of a) 2×10^9 and b) 8×10^9 cm^{-2} (these PC foils were irradiated from four directions, each with a fluence of a) 5×10^8 and b) 2×10^9 ions/cm^2). The electrodepositions were carried out at -1.4 V vs. Ag/AgCl at 60°C on a Cu back-electrode. The low magnification image in Figure 38a reveals an unstable network with interconnected wires being collapsed and forming bundles of wires. The high magnification image shown as inset elucidates the lack of interconnections between the wires which explains the stability of this network. In contrast, the network with higher number density of wires seems to be very stable (Figure 38b). The vast number of interconnections stabilizes the whole network structure and makes it free-standing. The inset in Figure 38b shows several crossing wires yielding a dense matrix. At very high number densities the network will become too dense losing the advantage of the one-dimensionality due to the significant overlap of wires along their length resulting in unfavorable transport properties.

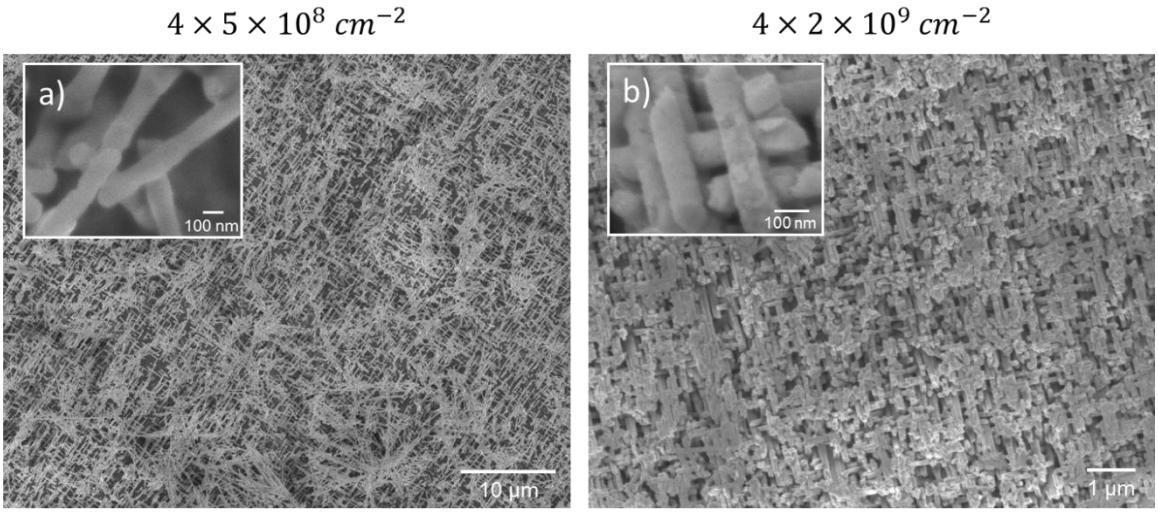

Figure 38: SEM images of nanowire networks with a wire diameter of 90 nm and number density of a) $4\times5\times10^8$ cm^{-2}, and b) $4\times2\times10^9$ cm^{-2}, showing an enhanced mechanical stability for the network with a higher density.

The space between the wires (inter-wire spacing) strongly depends on the density of wires and well as the wire diameter. Figure 39 (a) and (b) show SEM images of networks having an identical density (2×10^9 cm^{-2}) but different diameters of wires being 150 and 210 nm. A stable network with dense but individual wires with a diameter of 150 nm is revealed in Figure 39a, whereas the nanowires with larger diameter (210 nm) overlap and merge significantly (Figure 39b).

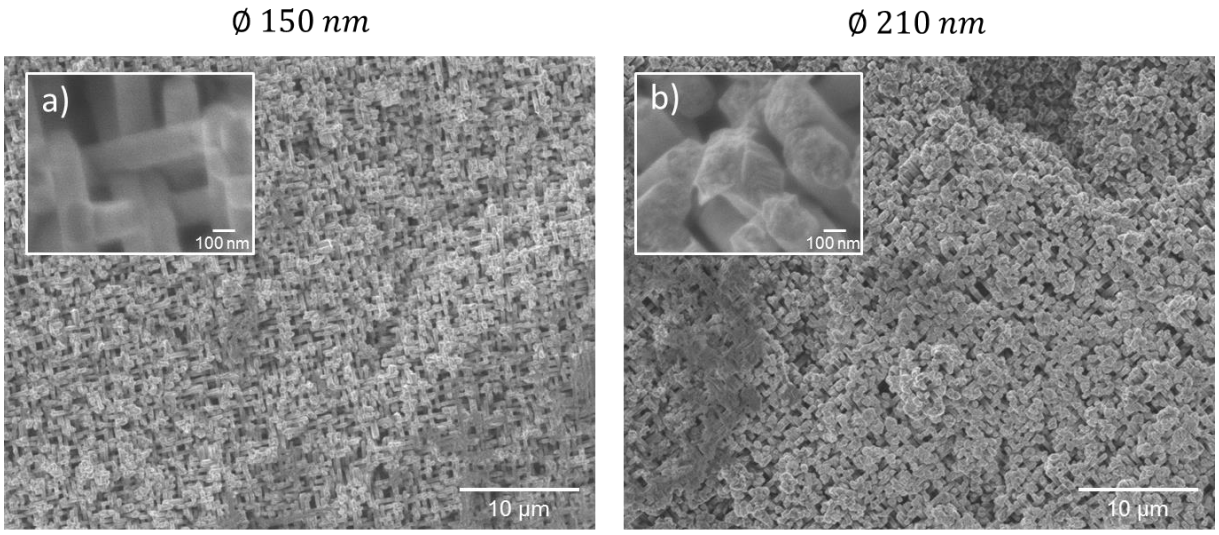

Figure 39: SEM images of nanowire networks with a wire density of $4\times5\times10^8$ cm^{-2} and diameters of a) 150 and b) 210 nm. The wires in (b) possess significant overlapping because of the large diameter.

To obtain networks which have large inter-wire spacing and high stability at the same time, networks were synthesized in membranes which were irradiated with an additional fifth position parallel to the surface normal. The preparation of membranes with combination of tilted and vertical pores is described in Section 3.3. The main advantage of these structures is the increase of the number density of wires without a significant increase of overlapping

effect, which would be more probable in the case of irradiation from only four directions but with higher fluence. Additionally, the vertically oriented pores facilitate the wetting and diffusion of ions inside the membranes resulting in more homogeneous network growth.

SEM images of a network with additional cylindrical wires oriented perpendicular to the substrate are shown in Figure 40. The diameter and number density of these wires are 150 nm and 5×10^{9} cm^{-2}, respectively. The low and slightly higher magnification SEM images (Figure 40 a,b) show homogeneous growth of the network over the complete substrate. Figure 40c shows zoomed-in SEM image and corresponding 3D representation of the network, where the tilted wires of the network are marked in blue, and the red color indicates the vertically aligned wires. The tips of the tilted wires show an oval shape, whereas the tips of the vertically aligned wires have a perfectly circular shape when looking from the top of the network. The high magnification SEM image of the area marked in orange is shown in Figure 40d, which displays junctions between multiple wires. Regions marked in white illustrate that many wires can cross through each other at the same position. Several of the tilted and vertically aligned wires are marked with blue and red circles, respectively. The advantage of this network structure is that the overlap of wires is mainly limited to junctions, and the wires have almost no overlap along their length until the next junction with other wires. This keeps the one dimensionality of the structure, especially for applications where the size of the wire should be comparable to the diffusion path length of the charge carriers in order to minimize the recombination probability, e.g. for photoelectrochemical water splitting. Another high magnification SEM image is shown in Figure 40e, which clearly shows wires with five different orientations (four tilted and one perpendicular to the substrate).

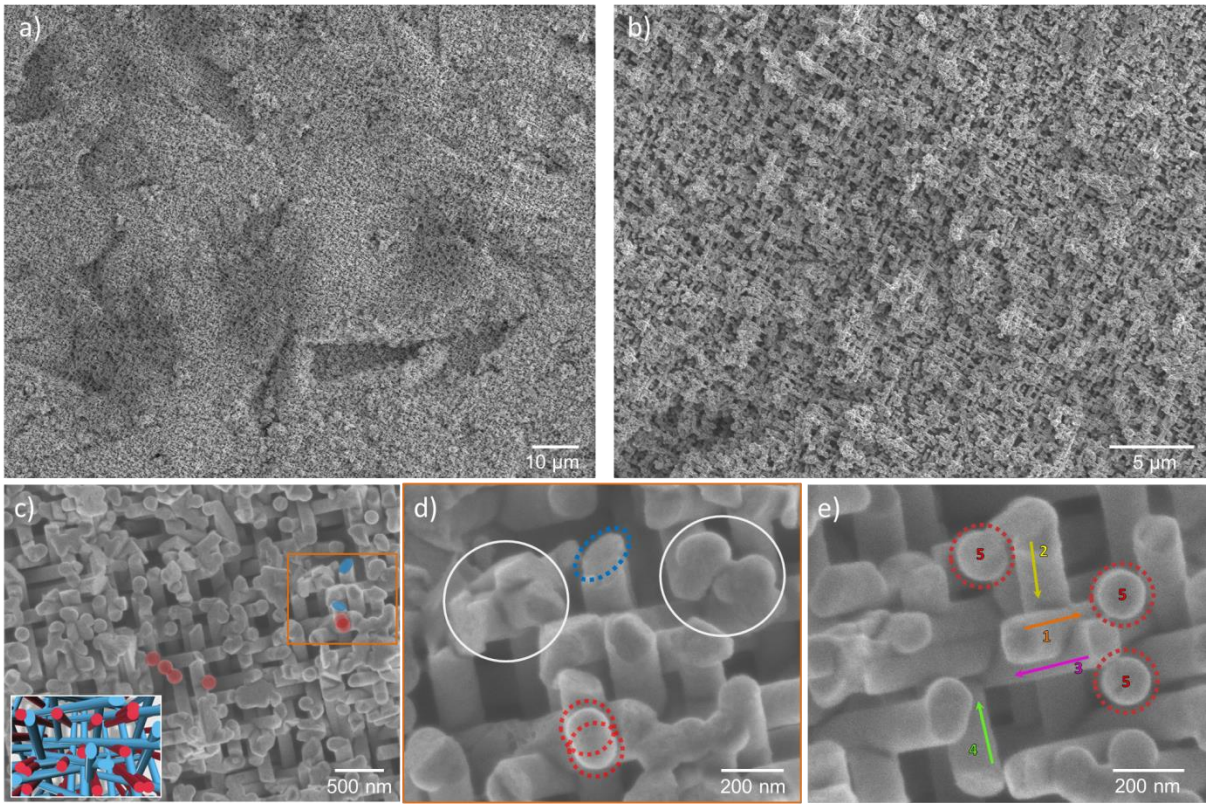

Figure 40: SEM images of nanowire network with a wire diameter and density of 150 nm and 5×10^9 wires/cm^2 "standing" on an array of parallel cylindrical wires in a) low and b-c) higher magnifications. The inset in (c) shows a 3D illustration of the top view of the network with wires tilted (blue) and perpendicular (red) with respect to the substrate; d-e) zoomed-in SEM images of the network showing intersections of several wires and the five orientations of wires.

The flexibility of the ion-track technology provides a wide range of diameters and wire densities, but the selection of diameter and density should be done carefully. Therefore the limits and challenges of fabrication of ZnO nanowires with a high number density were investigated as discussed in the next section.

5. Passivation of ZnO nanowires and nanowire networks with TiO_2 shell

This chapter provides knowledge about the crystallinity and composition of ZnO nanowire networks as well as the TiO_2 shell of ZnO/TiO_2 nanowires and networks coated by atomic layer deposition at different temperatures.

5. ZnO nanowires and nanowire networks with a TiO_2 shell

To protect ZnO nanowires from corrosion and make them more suitable for photoelectrochemical measurements, core/shell structures with a titania (TiO_2) shell were investigated. The TiO_2 layer is expected to protect ZnO from photo(electro)chemical corrosion in aqueous media. Different combinations of ZnO and TiO_2 core/shell structures are known from the literature as photoelectrodes for photoelectrochemical water splitting,[61,132] dye sensitized solar cells[133,134] or biological applications.[135,136] In this chapter, two types of ZnO/TiO_2 core/shell structures are discussed: i) nanowires coated with amorphous titania, and ii) nanowire networks with an anatase-TiO_2 shell.

5.1. ZnO nanowires with amorphous TiO_2 shell

Array of ZnO nanowires with a diameter of ~80 nm was electrochemically deposited in 30 µm PC membrane (10^9 pores/cm^2) by applying -0.8 V vs. Ag/AgCl at 80˚C using 0.1 M $Zn(NO_3)_2 \cdot 6H_2O$. After subsequent dissolution of the polymer matrix, the nanowires were coated with TiO_2 at 110˚C at GSI using a flow-type ALD reactor R-200 Basic from PICOSUN™. As first and second precursors and purging gas TTIP, H_2O and N_2 were used, respectively. One cycle consisted of 5.2 s of TTIP and 0.4 s of H_2O exposure, and 50 s purging with N_2 in between the exposure steps. 960 cycles were applied to deposit a ~10 nm thick layer.[58]

Figure 41 (a) and (b) illustrate schematically an electrodeposited and ALD coated ZnO nanowire. The SEM image in Figure 41c shows several wires on a Au TEM grid. As expected, the wires are continuous and completely filled. In the SEM image inspected by using a low secondary electron detector in transmission mode (Figure 41d), the slight contrast at the edges and along the wires is assigned to the TiO_2 shell. In the corresponding EDX spectrum (Figure 41e) the L and K lines of Zn originate from ZnO. The K lines of Ti result from the TiO_2 shell. The C and Au signals are assigned to the Au TEM grid with lacey carbon film. In addition, Cu L and K lines are detected, which are better visible in the inset in Figure 41e.

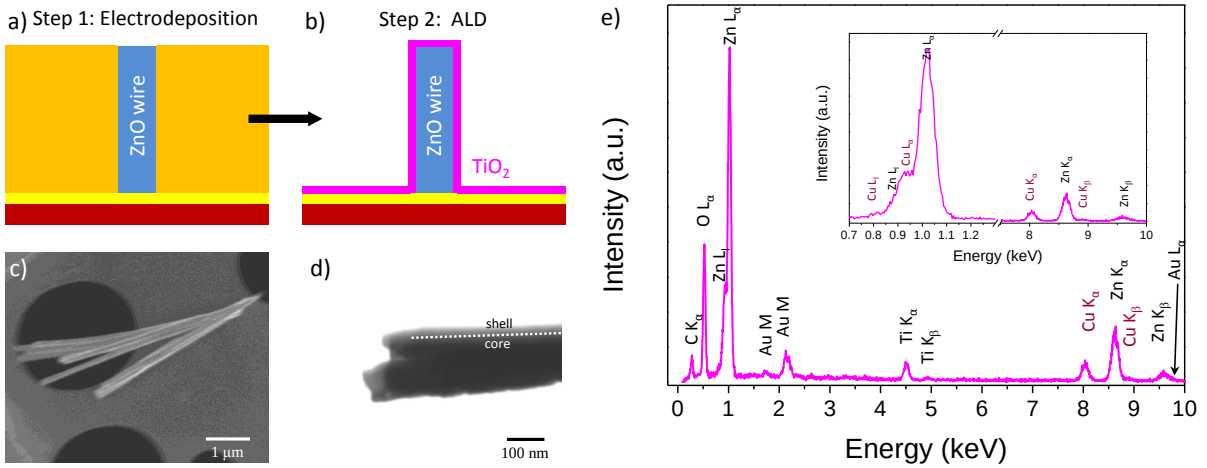

Figure 41: (a-b) Schematic representation of the a) electrodeposition of ZnO in a non-coated membrane, and b) atomic layer deposition of a TiO_2 layer on top of ZnO nanowires after dissolution of the polymer matrix. (c-d) SEM images ZnO/TiO_2 core/shell wires captured with a c) secondary electron detector and d) low secondary electron detector in transmission mode, e) corresponding EDX spectrum of a ZnO/TiO_2 core/shell wires.

To understand where the Cu signal originates from, the nanowires were investigated by using high resolution transmission electron microscopy (HRTEM) with high-angle annular dark-field (HAADF) imaging and electron energy loss spectroscopy (EELS) in collaboration with Dr. Wilfried Sigle at the MPI for Solid State Research in Stuttgart. The HAADF image of a ZnO/TiO_2 nanowire is shown in Figure 42a. The ZnO core and the TiO_2 shell can be distinguished due to the contrast difference. The nanowire possesses a continuously coated homogeneous TiO_2 shell (~7 nm) and some surface voids due to the roughness of the ZnO wire. Figure 42 (b) and (c) present the elemental mapping and the EELS spectrum, respectively. The spectrum image clearly shows the presence of Cu in the wires (blue areas), which is confirmed by the spectrum in Figure 42c. These ZnO wires obviously contain a Cu contamination, most probably arising from the diffusion of Cu from the substrate into the wires. Cu diffusion into ZnO is a known effect which is often used to dope ZnO with Cu [137–139] e.g. for ferromagnetic application of ZnO:Cu systems.[140] Figure 42d shows a low magnification HAADF image of several ZnO/TiO_2 nanowires where areas of a contamination with Cu can be detected due to the color contrast (marked with blue arrows). The inset shows a feature with well-defined edges which suggests that the structure is crystalline. For investigation of the synthesis process of ZnO nanowires and their characterization, the contamination with copper is an undesired effect. Thus, for further ZnO depositions only Au substrates were used (especially for photoelectrochemical measurements).

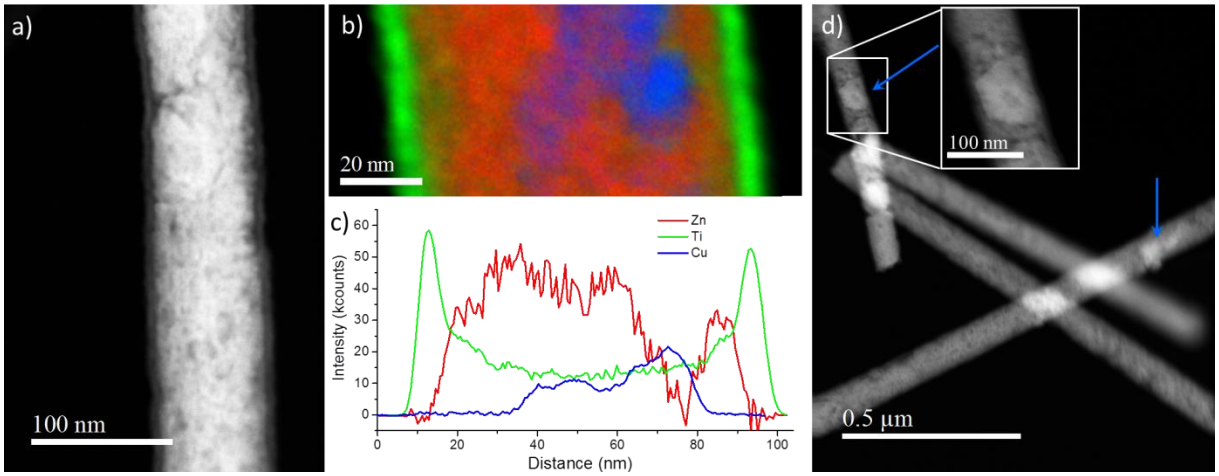

Figure 42: a) HAADF image of ZnO/TiO_2 nanowire with ~80 nm core and ~7 nm shell, b) elemental mapping and c) EELS spectrum of corresponding nanowire showing the presence of Cu in some areas of the wire, d) low magnification HAADF image showing areas on nanowires (marked with blue arrows) with possible Cu contamination. The bright contrast in the areas where the nanowires overlap is assigned to the availability of more material. The inset shows a small crystal with well-defines edges.

To measure the coating thickness more precisely and to investigate the crystalline structure of the core/shell wires, HRTEM was applied. Figure 43a presents a low magnification HRTEM image of several nanowires lying on a Au TEM grid. The corresponding TEM image of the area marked with a yellow frame is shown in Figure 43b. The cores of the wires show clear and continuous fringes corresponding to the (0002) planes of ZnO, according to the measured plane distance being ~0.26 nm. However, in some small areas with well-defined fringes, the measured distance of the planes was smaller, namely ~0.236 nm (Figure 43c), which matches well with the *d*-spacing value of the (111) planes of CuO. This can mean that in the ZnO nanowires the Cu, detected by EELS measurements, exists in an oxide state. HRTEM images of different areas of a ZnO/TiO_2 core/shell nanowire are shown in Figure 43 (d) and (e). The mean thickness of the shell is ~8 nm. In general, the TiO_2 layer looked amorphous, which is expected for low temperature ALD of TiO_2.[141] However, fringes were detected in some areas of the shell (see framed areas in Figure 43 d, e). The white lines show the orientation of the fringes. Two high magnification HRTEM images of areas marked in Figure 43e are shown in (f) and (g). The measured *d*-spacing matched with the (101) planes of anatase TiO_2, which was confirmed by the Fourier transform image (Figure 43h) of the area shown in Figure 43f. So, it can be concluded that the TiO_2 shell ALD-deposited at 110˚C has an amorphous structure, with some areas consisting of fringes corresponding to the anatase phase of titania.

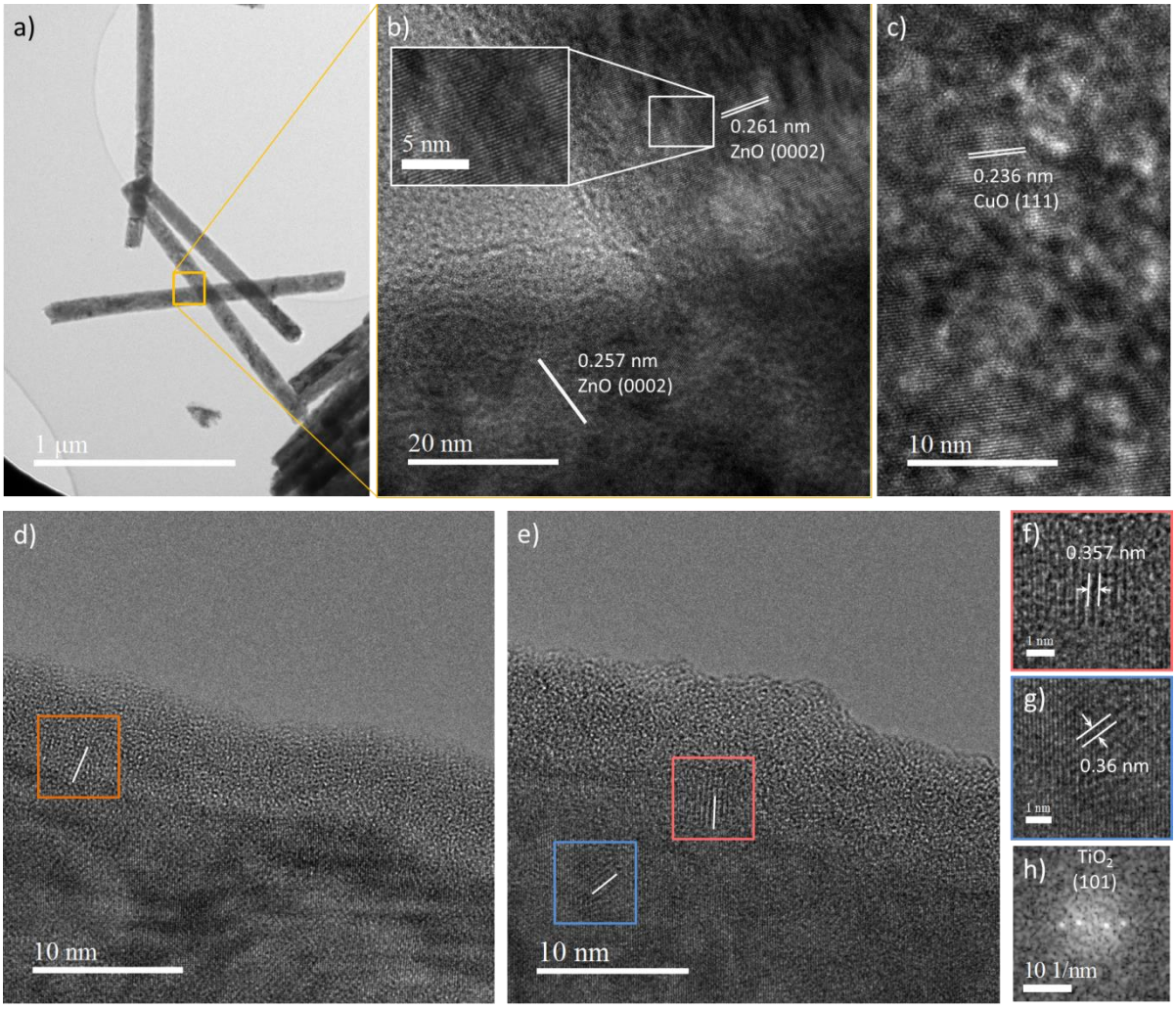

Figure 43: HRTEM images of (a-b) ZnO/TiO_2 core/shell wires in low and high magnification, showing the well-ordered and continuous planes of ZnO (0002) with a *d*-spacing of ~0.26 nm, c) area on the nanowire which consists of well-defined fringes with a plane distance of 0.236 nm corresponding to the (111) plane of monoclinic CuO, (d-e) edge of a core/shell nanowire with ~8 nm thick shell, which has small features showing fringes, (f-g) small features on TiO_2 shell in high magnification, with a measured *d*-spacing of ~0.356 which can be related to anatase TiO_2 (101). h) Fourier transform image corresponding to (f) confirming that the observed planes are (101) of anatase titania.

5.2. ZnO and ZnO/anatase-TiO_2 core/shell nanowire networks

ZnO nanowire networks were electrodeposited in membranes with Au substrates at -1 V vs. Ag/AgCl and 60˚C using 0.1 M $Zn(NO_3)_2 \cdot 6H_2O$. For some series of samples, a thin TiO_2 layer with a thickness of ~20 nm was deposited onto networks (total number density of 8×10^9 cm^{-2}) using ALD. The temperature of the ALD process was increased to 250˚C in order to obtain crystalline TiO_2 for better transport properties. The deposition was carried out by using TTIP as a first precursor with an exposure time of 1.6 s, followed by purging with N_2 for 8 s. The exposure of H_2O as a second precursor was 0.1 s, and the residual molecules were afterwards purged with N_2 for 8 s. According to the calibration value, these parameters result in a deposition of 0.0197 nm TiO_2 per cycle, i.e. to achieve a ~20 nm coating thickness 1000

cycles were applied. To study the influence of the higher temperature in the ALD chamber on the morphology of the ZnO nanowire network, the samples were systematically studied by SEM before and after ALD.

Figure 44 shows SEM images of the same sample before (a-c) and after (d-f) TiO_2 coating in different magnifications. The low magnification images (Figure 44 a,d) give an overview of the homogeneous growth of the network. Higher magnification images (b, e) show a denser matrix for the image after coating, which is related to the ~20 nm TiO_2 layer decreasing the inter-wire space. Images at even higher magnification (Figure 44 c,f) show that the network underwent a morphological modification. Before the ALD process, the wires have tips with sharp edges, looking almost like facets. After coating, the tips look more rounded indicates that the high temperature has a slight influence on the wire morphology. However, it is important to note, that after ALD the wires did not change their cylindrical shape and the network structure with interconnected wires remained intact. The diameter of the wires measured before and after the ALD process were ~150 and ~190 nm, respectively, which matches with the expectation for a ~20 nm thick coating.

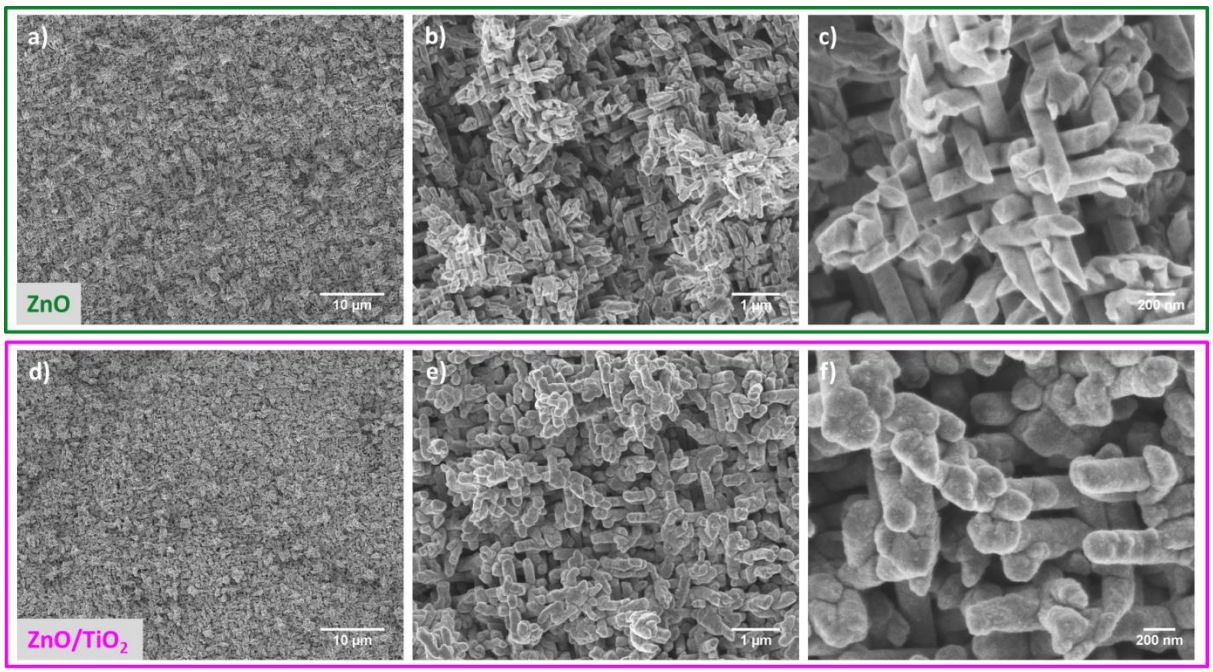

Figure 44: SEM images of the same ZnO nanowire network with a total number density of 8×10^9 cm^{-2} and a diameter of 150 nm before (a-c) and after (d-f) ALD coating at 250˚C with ~20 nm thick TiO_2.

The corresponding EDX spectra of this sample before and after ALD coating are shown in Figure 45. In both cases the characteristic L and K lines of Zn and the L line of O are detected. In the spectrum measured after coating, the K and L lines of Ti are also observed. The Au peaks are assigned to the Au substrate of the network, and the Al signal originates from the SEM sample holder. No other peaks were detected, meaning that there were no impurities in the wires.

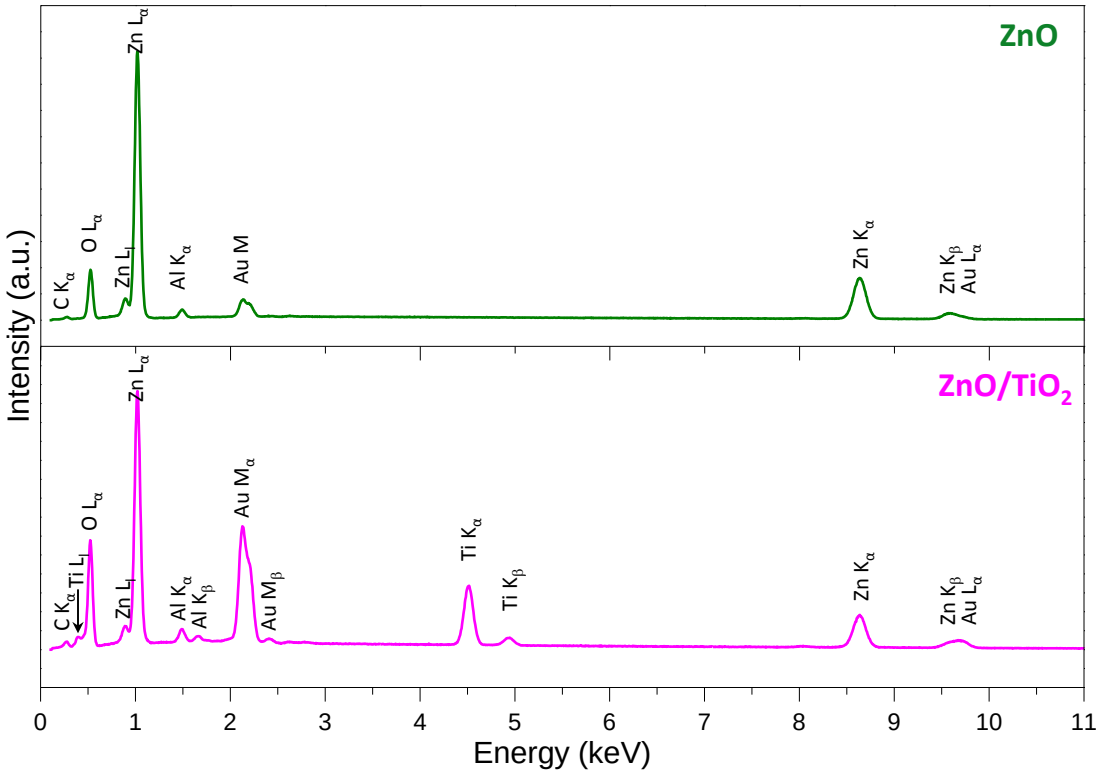

Figure 45: EDX spectra of the same ZnO network before (green) and after (purple) ALD coating with ~20 nm thick TiO_2.

The structural properties of ZnO and ZnO/TiO_2 nanowire networks were investigated first by using XRD. Representative XRD diffractograms (θ - 2θ scan) of non-coated and coated samples are shown in Figure 46. In contrast to the parallel nanowire arrays, the networks exhibit almost all reflections for ZnO indicating that the samples ate probably polycrystalline (blue curve). Information about the texture could not be deduced due to the tilt of the network wires in different directions. The nanowire networks coated with ~20 nm TiO_2 show a reflection at 25.3˚, which corresponds to the (101) plane of anatase titania (JCPDS card Nr. 21-1272). The pattern in black corresponds to the Si reference sample serving as a substrate during the measurement. The 2θ values of ZnO, TiO_2, Au, and Cu from the JCPDS cards are given at the bottom on Figure 46. The Cu signal originates from the supporting layer deposited on a ~8 µm thick Au substrate after the nanowire growth. Therefore no Cu contamination inside the nanowires is expected.

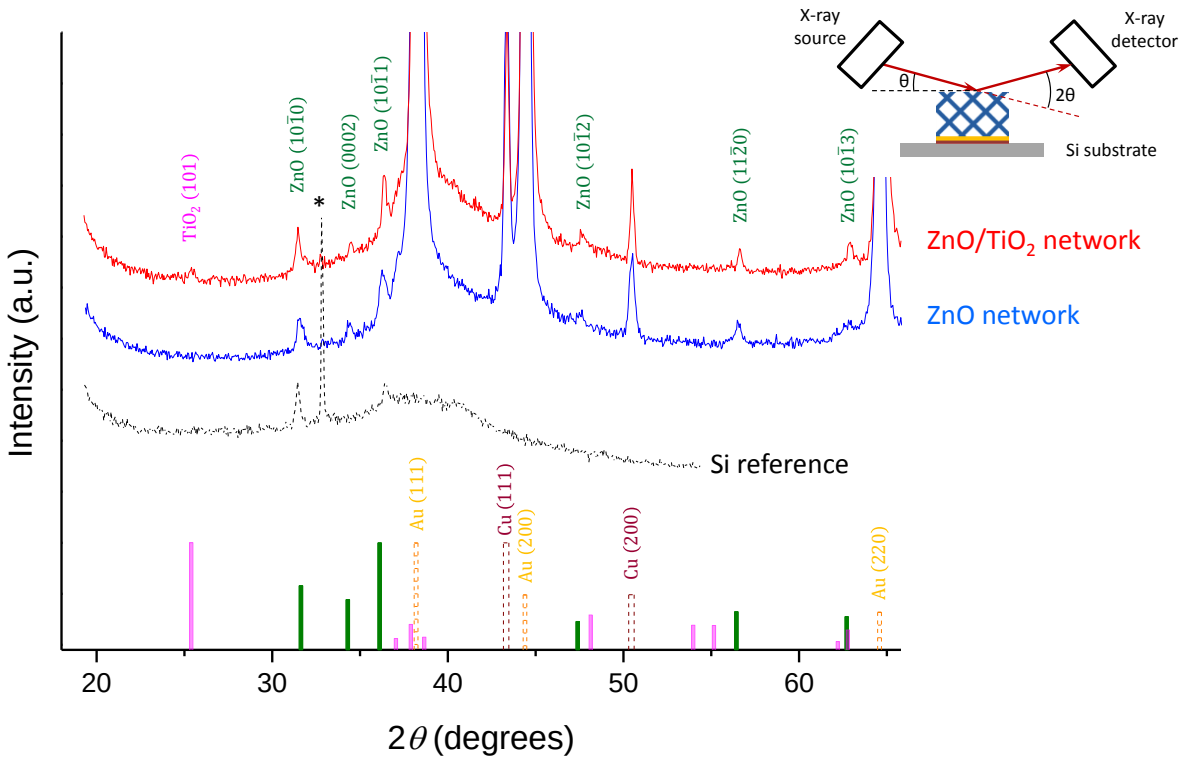

Figure 46: XRD diffractograms of bare (blue) and ~20 nm TiO_2 coated (red) ZnO nanowire networks. The coated samples show a reflection corresponding to (101) planes of anatase TiO_2. The pattern in black is from the Si reference sample which served as a substrate for the measurement. Au and Cu signals originate from the network substrate itself.

Because of the complex structure of nanowire networks, which consist of individual wires having a tilt of 45˚ with respect to the surface normal and the many interconnections between them, more precise techniques were required for further analysis. The crystallinity as well as the morphology and elemental composition of the ZnO and ZnO/TiO_2 wires detached from the networks were further investigated using HRTEM, HAADF, SAED, and EELS. The samples imaged with SEM after transferring them onto TEM grid are presented in Appendix E.

Figure 47a shows the HAADF image of a ZnO nanowire from a nanowire network. Due to the contrast difference, small gray/black areas are noticeable on the wire, which represent surface voids that arose from the roughness of the wires in the network. In Figure 47b a high magnification HAADF image of the same wire is shown. Within this complete area, the wire exhibits continuously ordered layers. The higher magnification images of the areas numbered with 1, 2, and 3 are shown in Figure 47 c), d), and e), respectively. These images reveal the well-defined layers, including in the area of the void (e) and prove the continuous growth of the same planes being ZnO (0002) according to the measured d-spacing of 0.257 nm.

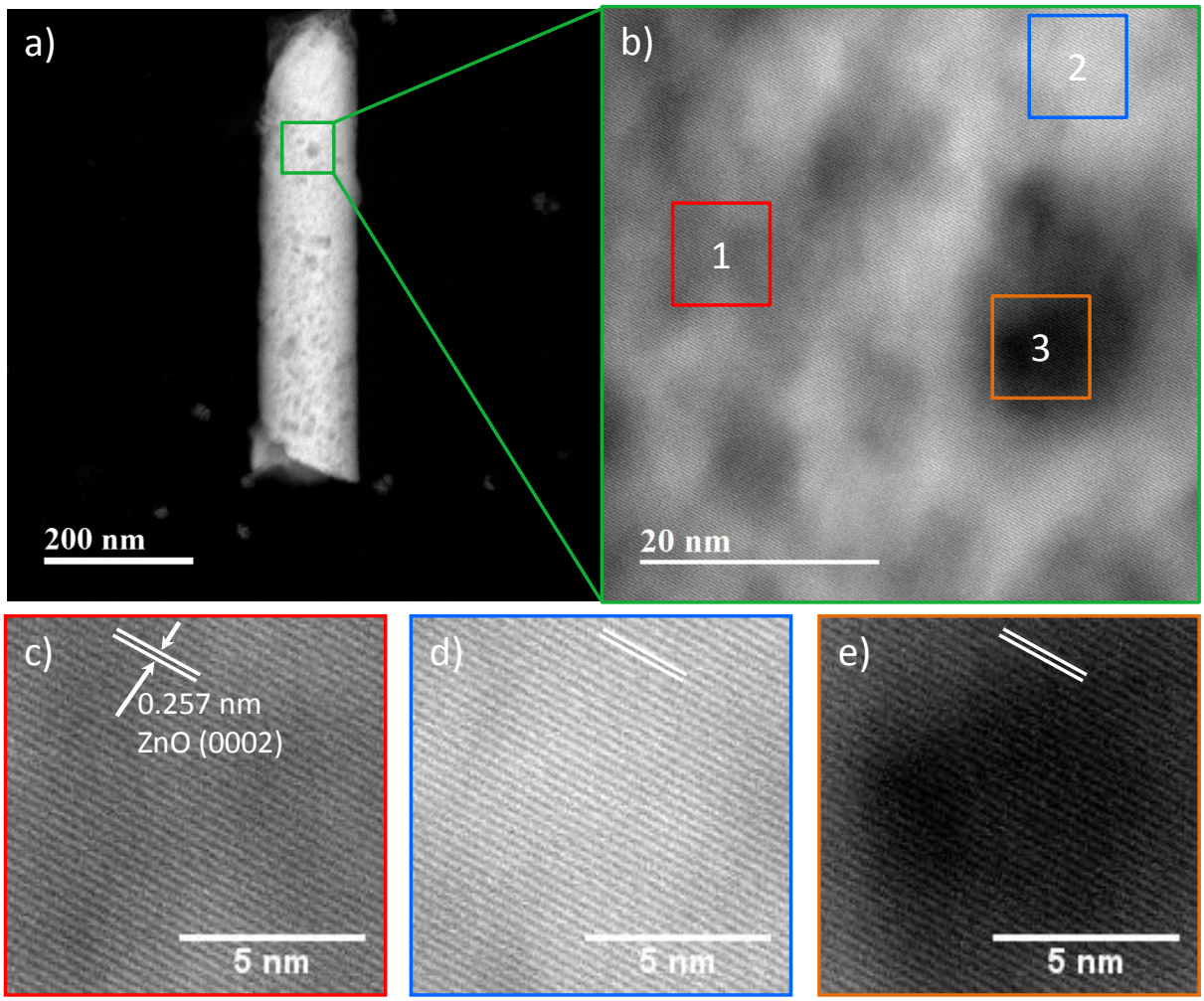

Figure 47: HAADF images of a) non-coated ZnO nanowire with a diameter of 150 nm, dark spots correspond to voids arising from the roughness of the wire; b) the wire shown in (a) in a higher magnification, elucidating the continuously layered structure independent on the voids and the angle between the wire axis and the growth direction, and c, d, e) three areas indicated in (b) in higher magnification, showing similar and well-defined layers.

The results of HRTEM studies on the structural properties of both ZnO and ZnO/TiO_2 wires are presented in Figure 48. The HRTEM image of ZnO (Figure 48a) gives similar information as the HAADF images shown in Figure 47. The measured distance between the planes was 0.26 nm indicating that the observed planes are (0002). The lattice fringes are continuous along the wire (including the edge) without any disorder. The corresponding SAED pattern of the wire is shown in Figure 48b. The wire shows a strong diffraction of (0002) planes of hexagonal ZnO, indicating that the wire has a rather single-crystalline nature in the analyzed area. Network wires coated with nominal ~20 nm TiO_2 also show a crystalline ZnO core and a polycrystalline TiO_2 shell (Figure 48c). It has a texture of (101) planes of the anatase phase according to the measured plane distances being ~0.353 nm. In Figure 48c also twin grains with the same (101) planes can be detected. The measured thickness of the TiO_2 shell was ~19 nm, which is in good agreement with the expected coating thickness of ~20 nm. Fringes of ZnO with (0002) and $(2\bar{1}\bar{1}0)$ planes were also observed for this wire. Figure 48d shows the

SAED pattern of a core/shell nanowire with strong reflections of the ZnO (0002) and $(2\bar{1}\bar{1}0)$ planes and weak reflections of the TiO_2 shell. The inset reveals the Fourier transform image of the TiO_2 shell without an influence from the ZnO core, which was created from the HRTEM image shown in the inset in Figure 48c. The d-spacing measured from the Fourier transform image was 0.352 nm, which matched well with the value measured from HRTEM corresponding to the (101) planes of anatase TiO_2.

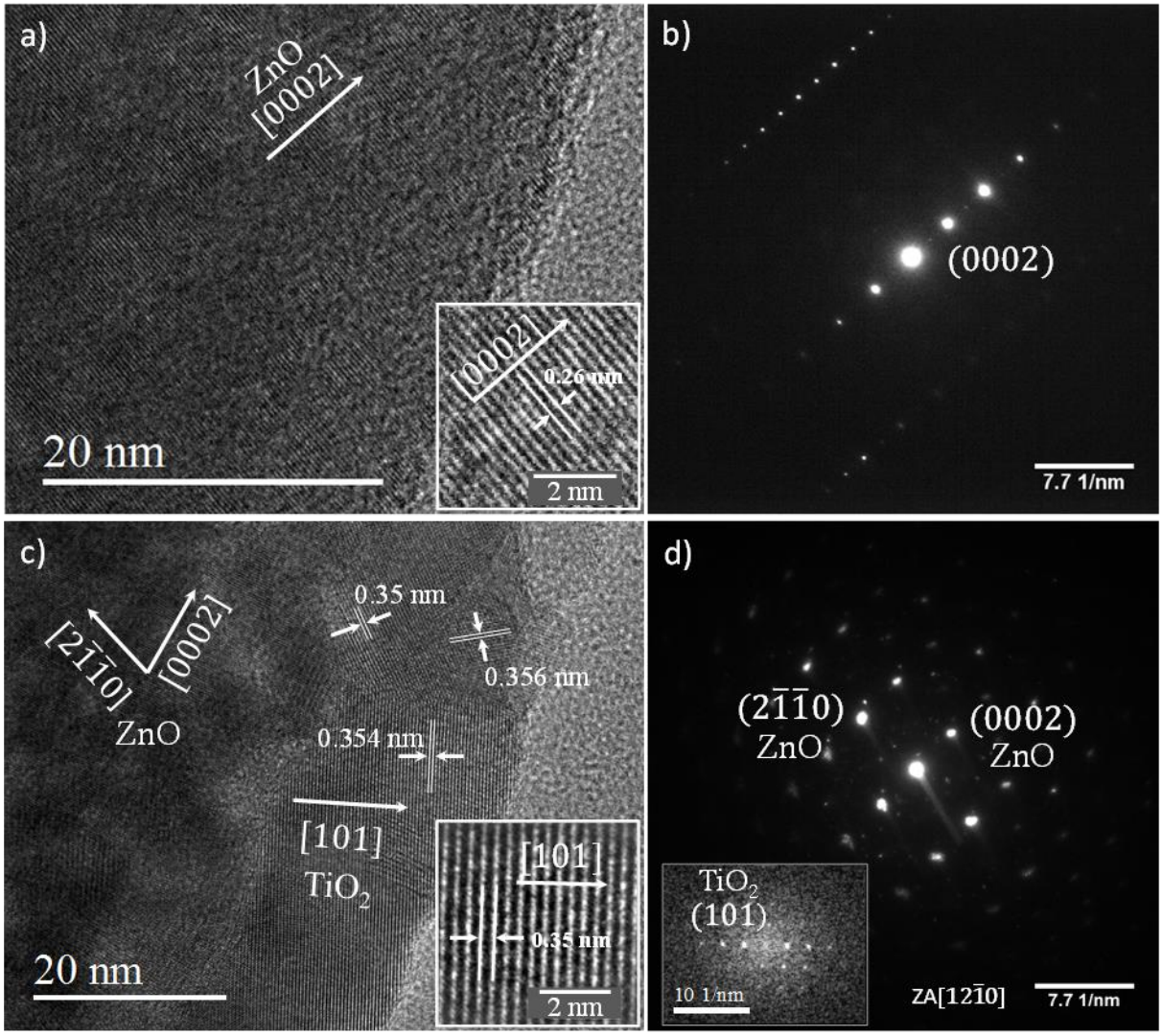

Figure 48: HRTEM images of a) ZnO and c) ZnO/TiO_2 nanowires. The insets show high magnification images with measured *d*-spacings of 0.26 nm (a) and 0.35 nm (c) corresponding to the crystallographic planes of ZnO (0002) and TiO_2 (101), respectively. SAED pattern of c) ZnO and d) ZnO/TiO_2 nanowires with inset in (d) showing the Fourier transform image of the TiO_2 shell.

It was also possible to image a region from the intersection of two wires extracted from a core/shell network. Figure 49a shows the HRTEM image of this area, with an inset of a zoomed-in region presenting well-ordered fringes which belong to ZnO (0002) planes according to the distance between the planes. The corresponding SAED pattern is given in Figure 49b. The bright points arise from the (0002) planes of wurtzite ZnO, while the less intense points (marked with green arrows in the image) are assigned to anatase TiO_2 (101)

planes based on the values of the calculated *d*-spacing. Figure 49 (c) and (d) show a HAADF image of a junction of two wires and the corresponding elemental mapping by EELS, respectively. Both images prove the conformal coating of the ZnO wires with a homogeneous layer of ~20 nm TiO_2. EELS spectrum image is displayed in Figure 49e, along with a chemical composition profile across the wire shown in Figure 49f.

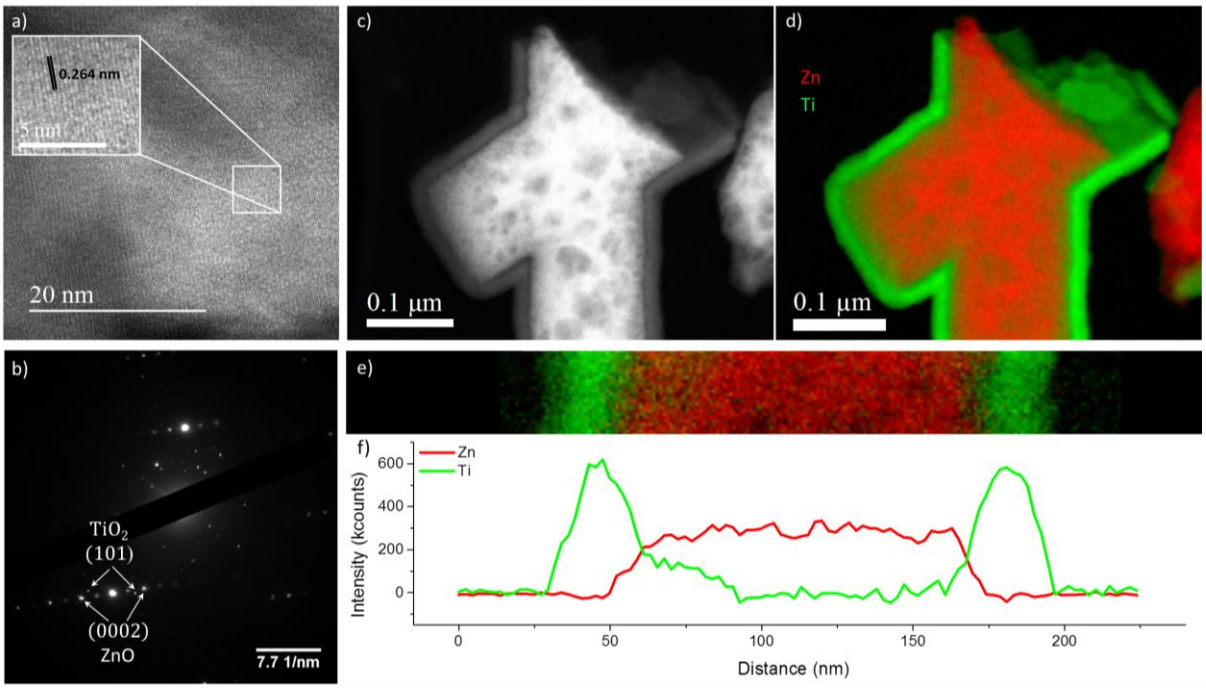

Figure 49: a) HRTEM image of an intersection area of two wires, showing well-defined fringes of wurtzite ZnO with (0002) planes having a *d*-spacing of 0.264 nm, b) the corresponding SAED pattern of the area shown in (a); c) HAADF image of a junction of two wires and d) corresponding elemental mapping by EELS, showing a conformal coating with ~20 nm TiO_2 layer; e) zoomed-in EELS spectrum image and f) corresponding chemical composition profile of the ZnO/TiO_2 core-shell nanowire.

Based on the structural and compositional analysis of the ZnO wires coated with a layer of ~20 nm TiO_2 at 250˚C, it is possible to conclude that the wires of the network consist of a ZnO core preferentially oriented along the [0001] direction. Some fringes with $(2\bar{1}\bar{1}0)$ planes were also observed. The growth at the junctions is complete with continuous planes. The wires are uniformly coated with a homogeneous and polycrystalline TiO_2 layer consisting of twin grains with mainly (101) planes of the anatase phase. While the XRD pattern exhibited various reflections indicating a polycrystalline nature of the wires, TEM analysis revealed highly crystalline sections of wires, which is an important property for efficient transport with minimized recombination of charge carriers. Further investigations are required to determine the gain size and observe the presence grain boundaries.

Bare ZnO and core/shell ZnO/TiO_2 nanowire networks similar to those presented in this section were used as photoanode model systems to test the compatibility of these network structures for photoelectrochemical water splitting, which results are presented in Chapter 6.

6. Photoelectrochemical measurements with TiO_2, ZnO and ZnO/TiO_2 photoanodes

This chapter sheds light on the photoelectrochemical (PEC) measurements performed with bare TiO_2, bare ZnO and core/shell ZnO/TiO_2 nanowire networks and films. The importance of the TiO_2 coating for the enhancement of the photocurrent as well as a protective layer against photoelectrochemical corrosion of the ZnO network is discussed.

6. Photoelectrochemical measurements

Nanowire-based photoelectrodes are of interest due to the one-dimensional shape and geometrical orientation of the wires. These properties are expected to enable an enhanced light absorption due to the extensive light scattering. It is expected that the reduced wire diameter facilitates a rapid transport of the photogenerated charge carriers to the surface of the wire, and the large surface area of the photoelectrode/electrolyte interface leads to faster redox reactions.[120]

ZnO, Au/TiO_2 and ZnO/TiO_2 3D nanowire networks were employed as model systems to study the photoelectrochemical (PEC) performance of such nanowire structures as compared to their film counterparts. The stability of the photoanodes in an aqueous media and under illumination as a function of time was investigated. X-ray photoelectron spectroscopy (XPS) was employed to analyse the chemical composition of the samples and to define their work function (WF) and the valence band (VB) position. These energy values were used for a theoretical study of the band alignment at the Au-ZnO and Au-TiO_2 contacts.

6.1. Description of film and nanowire network photoanodes

Film photoanodes were prepared under similar electrodeposition conditions as for the networks. First, the rough sides of non-irradiated polycarbonate foils were sputtered with ~100 nm Au (Figure 50a) followed by electrodeposition of ~7 µm Au on top (Figure 50b), as described in Section 4.1.1. An additional ~2-3 µm Cu layer was electrodeposited on the Au substrates (Figure 50c) to have them stable after removing the polymer foil. An immersion of the samples in acetone (Karl Roth, 99.9 %) for 1 or 2 hours (Figure 50d) allowed detaching the substrate layer from the polymer by mechanically peeling them off. The substrates, released from the polymer foils, were additionally washed with dichloromethane to ensure that no residual polymer remained on the surface (Figure 55e). Figure 50f shows the schematic representation of the final metallic substrate consisting of a sputtered Au and electrodeposited Au and Cu layers.

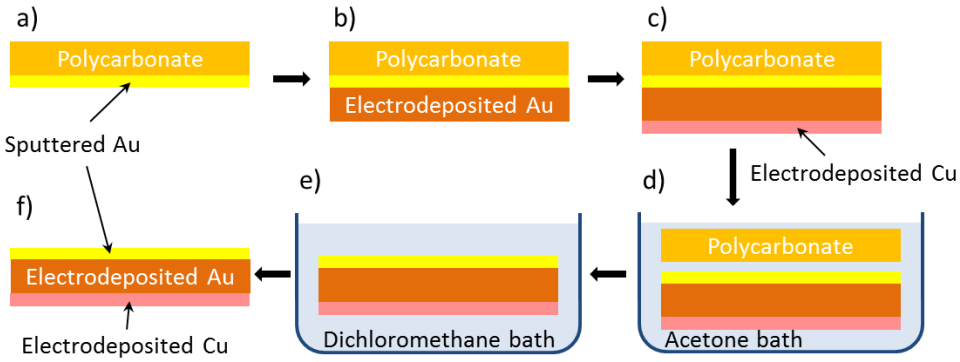

Figure 50: Schematic representation of the steps for the fabrication of a Au film-substrate. a) sputtering of a thin Au layer on the rough side of the polymer foil, b) electrodeposition of a ~7 µm thick Au film on the sputtered gold, c) electrodeposition of an additional ~2-3 µm thick Cu layer, d) detachment of the Au/Cu metallic layer from the polymer foil in an acetone bath, e) cleaning of the

sputtered surface of the metallic layer from polymer residues in a dichloromethane bath, f) final product consisting of layers of a sputtered Au and electrodeposited Au and Cu.

To prepare a TiO_2 thin film, the sputtered side of the Au substrate was coated with ~20 nm thick TiO_2[†] layer by ALD at 250˚C (see Section 5.2).

The electrodeposition of ZnO films on the Au substrates was first performed by applying -1 V vs Ag/AgCl at 60˚C. This resulted in a very poor film growth taking place mainly at the edges of the area exposed to the electrolyte. ZnO films with a better covering were grown by applying 10 cycles of cyclic voltammetry on the sputtered side of the substrates. The potential was swept between 0 and -1.5 V vs. Ag/AgCl with a scan rate of 10 mV/s. This process resulted in the growth of 7-10 µm thick films with a rough topography. Figure 51a shows a low magnification SEM image of the resulting film. Even at these tuned conditions of the electrodeposition, the film did not cover the metallic substrate homogeneously. Holes with µm size down to the bare substrate as well as cracks in the films were observed. The dark spots on the SEM image represent the ZnO-free areas. A higher magnification image of such a spot with hundreds μm^2 in size is shown in Figure 51b. The presence of cracks in the ZnO films is shown in Figure 51c in higher magnification. The width of the cracks reached up to a µm, which should not be crucial for PEC measurements, while the presence of bare Au in the non-covered areas is expected to influence the PEC performance of the ZnO films because of the Au/electrolyte direct contact. This issue was resolved by the conformal coating of a ~20 nm thick TiO_2 layer by ALD over the whole sample, thus obtaining ZnO/TiO_2 photoanodes.

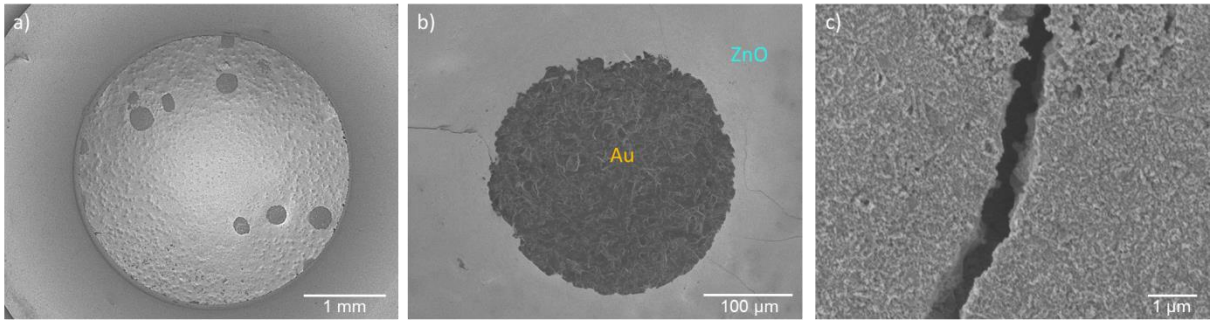

Figure 51: SEM images of a representative ZnO film electrodeposited by applying 10 cycles of cyclic voltammetry in a potential range of 0 and -1.5 V vs. Ag/AgCl at 60˚C in $Zn(NO_3)_2 \cdot 6H_2O$ electrolyte on Au substrate. a) Low magnification image showing the inhomogeneous coverage of the ZnO film on a Au substrate, b) higher magnification image of the film with a non-covered area of the Au substrate in the center with a size of hundreds of μm^2, c) crack on the ZnO film with a gap width up to 1 µm.

The crystallographic properties of ZnO and ZnO/TiO_2 films were studied using XRD. The XRD patterns of the corresponding films are shown in Figure 52. Almost all reflections known from the standard powder diffraction of ZnO were present in the films, meaning that the samples were polycrystalline. No preferred orientation was observed. At the 2θ angle of 25.28˚ a small reflection (see the zoomed-in inset) is noticed for the TiO_2-coated sample,

[†] Here and later in this chapter TiO_2 is always referred to anatase-TiO_2.

which corresponds to the (101) plane of TiO_2 in the anatase phase. The reflections of Au and Cu arise from the substrates.

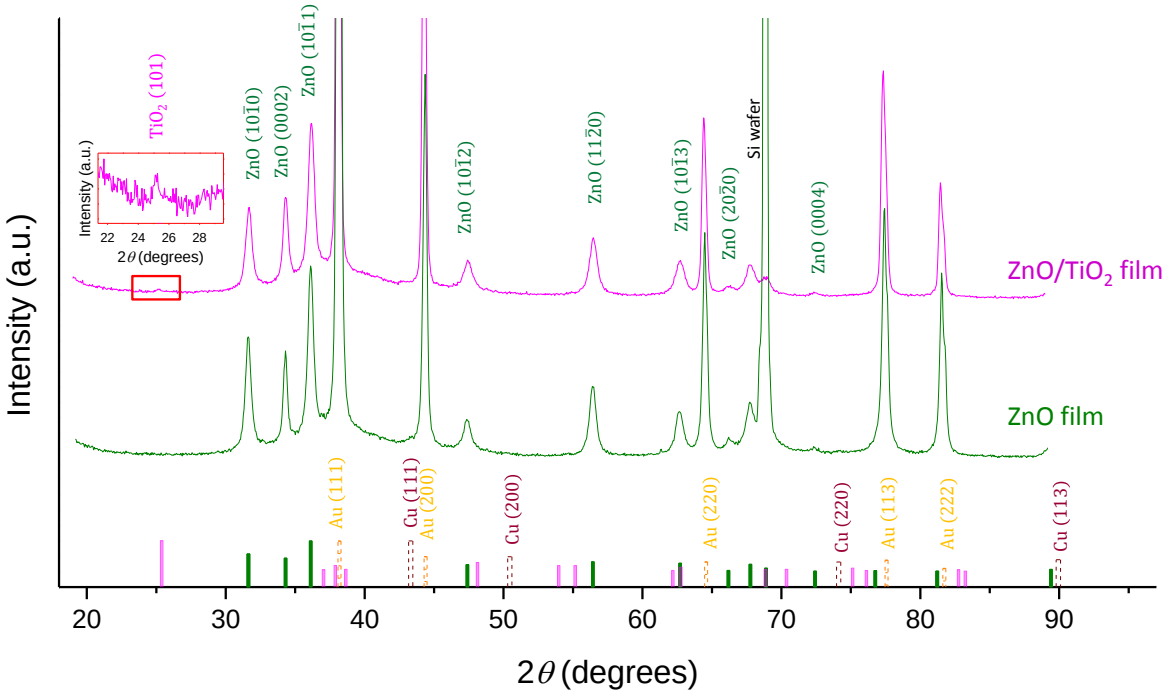

Figure 52: XRD patterns of ZnO (green) and ZnO/TiO_2 (purple) films showing that the ZnO film is polycrystalline, and the TiO_2 coating has an anatase phase.

Three types of network structures were prepared with a total wire density of 8×10^9 cm^{-2} (2×10^9 cm^{-2} from four directions): (i) a pure ZnO nanowire network with a wire diameter of 150 nm and no coating as well as core/shell (ii) Au/TiO_2 and (iii) ZnO/TiO_2 nanowire networks consisting of Au and ZnO core nanowires with a diameter of 150 nm and ALD-coated ~20 nm thick TiO_2 layer.

ZnO nanowire networks with heights of ~25 µm were synthesized as described in Section 4.3. The core-shell Au/TiO_2 nanowire network was prepared by electrodeposition of a Au network and ALD coating of TiO_2 at 250˚C after the polymer dissolution. Electrodeposition conditions and SEM analysis of these Au nanowire network are presented in Appendix F. The sample showed inhomogeneous growth: it was well grown at the edges, while the middle of the sample had rather thin network, where also the Au substrate was detectable. Since the electrodeposition of Au in networks was not established before, and since the main focus of this thesis is the synthesis of ZnO networks, no further efforts were put in the improvement of the homogeneity of the Au networks. This obtained network with a TiO_2 layer was used for PEC measurements.

6.2. Photoelectrochemical performance of nanowire networks vs. films

The schematic representations of the ZnO, Au/TiO_2 and ZnO/TiO_2 film and nanowire network photoanodes, described in previous sections, are shown in Figure 53.

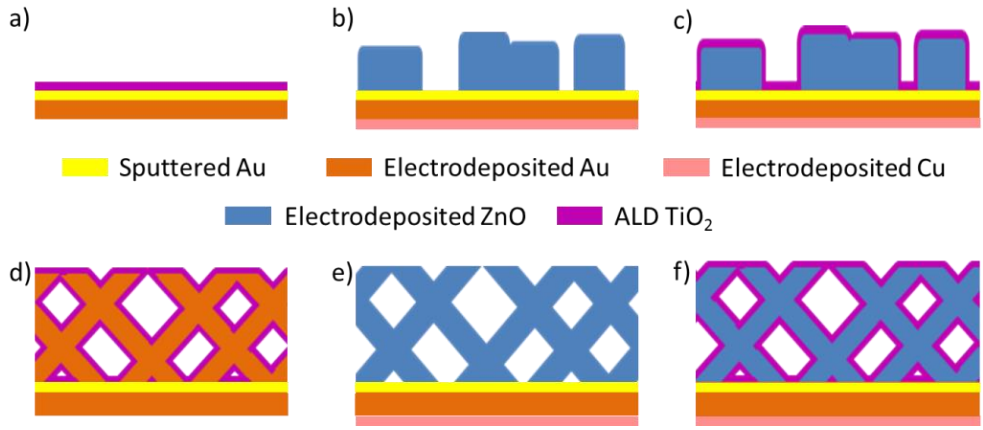

Figure 53: Schematic representation of the cross sections of the photoanodes with metallic substrates: a) ~20 nm thick TiO_2 film, b, c) 7-10 µm high ZnO films without (b) and with (c) ~20 nm TiO_2 coating, d) Au/TiO_2 core/shell network with a Au core diameter of 150 nm and a TiO_2 shell thickness of ~20 nm, e) ZnO nanowire network with a wire diameter of 150 nm and a height of ~25 µm, and f) ZnO/TiO_2 network with a height of ~25 µm, 150 nm ZnO wires and ~20 nm TiO_2 shell.

For the PEC measurements the light source was an AM 1.5 simulated light corresponding to 1 sun. The electrolyte was a 0.1 M K_2SO_4 with a pH 5.6. The complete setup for the measurement is described in Section 2.5. The photoresponse of the network photoanodes was investigated and compared to their film counterparts. First, linear sweep voltammetry (LSV) was sequentially performed in the dark and under continuous illumination, in a voltage range from -0.55 to 1 V vs. Ag/AgCl with a scan rate of 10 mV/s. After two scans each in the dark and under illumination, one more LSV scan was performed in the same potential range using chopped illumination (10 s dark, 10 s light) in order to analyze the photoresponse of the system to the chopped light. Because large surface area electrodes produce a much higher double-layer capacitance, a slower scan rate under chopped illumination is required in order to minimize the error introduced by capacitance effect. Therefore, the scan rate was decreased to 5 mV/s for the chopped LSV measurements. Additionally, several chronoamperograms (CA) were measured at a fixed potential of 0.62 V vs. Ag/AgCl using chopped illumination (30 s dark, 30 s light) to test the photo(electro)chemical corrosion and the lifetime of the nanowire networks as photoanodes. The CA curves were recorded up to 3 h under chopped illumination by switching the light on and off every 30 s. For ease of comparison with the values reported in literature, the potential range for LSV curves was also converted to the reversible hydrogen electrode (RHE) according to the Nernst equation, as explained in Section 1.4, while also keeping the scale of the potential vs. Ag/AgCl (sat. KCl) as measured.

Figure 54 shows the current densities as a function of applied potential under chopped light for all films (dashed lines) and nanowire networks (solid lines). Figure 54a presents the comparison of the current density for ~20 nm TiO_2 film (on a Au film) and network (on Au network with a nanowire diameter of 150 nm). It is noteworthy that the photocurrent density of the sample with the network structure is relatively higher than that of the film. In particular, the photocurrent density values (with dark current subtraction) around the potential of 0.7 V

vs. Ag/AgCl (equivalent to 1.23 V vs. RHE for pH 5.6) are 0.01 and 0.023 mA/cm^2 for film and network, respectively (see the inset of Figure 54a). These results revealed that even the non-homogeneously grown network produces twice more photocurrent than a film. Since the thickness and crystallinity of the TiO_2 layer is identical for both samples, it can be concluded that the difference in light-induced current is related to the geometry of the photoanodes, i.e. the nanostructured electrode with the same light-exposed area as the film but with a higher active surface area (electrode/electrolyte interface) yields a higher photocurrent. Besides the enhanced area for the redox reactions, also the light absorption might also benefit from the nanowire network geometry. The incident light scattered from the wire surface can be trapped in the network and then be absorbed by another wire creating electron-hole pairs as long as the energy of the photon is larger than the band gap. Although the photocurrent densities are still modest, these results support the concept of the photocurrent enhancement by means of high aspect ratio structures based on one-dimensional nanowires.

LSVs performed on bare ZnO film (7-10 µm thick) and nanowire network (~25 µm high, wire diameter of 150 nm) are shown in Figure 54b. Although the height of the network sample is almost two times higher than the thickness of the film, the current density recorded for the ZnO network sample is much higher than that of the ZnO film. The photocurrent density values (after dark current subtraction) around the potential of 0.7 V vs. Ag/AgCl are 0.024 and 0.088 mA/cm^2 for film and network, respectively (see the inset of Figure 54b), meaning that the 1D nanowire-based and relatively thick network generates ~3.5 times more photocurrent than the film.

These results indicate another advantage of nanowire-based photoelectrodes. The reduced path length of the minority charge carriers to the surface of the nanowires facilitate efficient charge carrier transport with minimized electron-hole recombination. Since the electron-hole pairs are usually generated close to the surface of the photoelectrode, the dimensions of the structures should be comparable to the inverse of the absorption coefficient of the selected material. In particular, ZnO films thicker than ~100 nm suffer from fast recombination of the charge carriers.[142] In contrast, large 3D nanowire networks consisting of thin 1D nanowires possess the advantages of one-dimensionality. In particular, their dimensions comparable to the light absorption depth and the charge carrier diffusion length should result in the increased photocurrent and the minimized recombination processes while transporting the charge carriers to the wire surface.

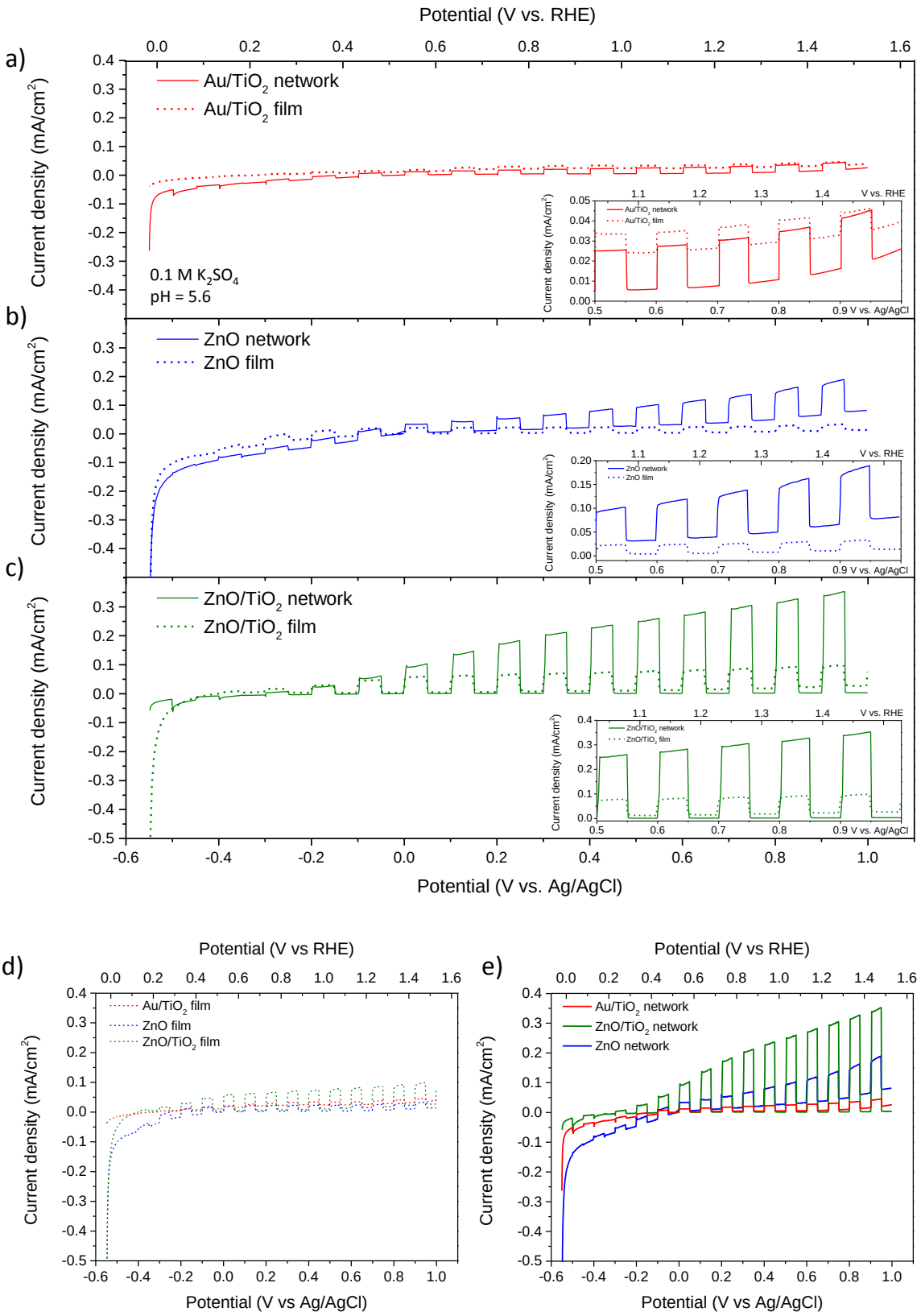

Figure 54: (a-c) Characteristic LSV curves of films (dotted) and networks (solid) of a) Au/TiO_2, b) ZnO, and c) ZnO/TiO_2, measured in 0.1 M K_2SO_4 (pH 5.6) under AM1.5G illumination with a scan rate of 5 mV/s. (d, e) The comparison of the LSV curves for the d) films and e) networks shows the same trend of photocurrent density being the lowest for the bare TiO_2-based and the highest for the ZnO/TiO_2-based photoanodes.

Among the mentioned advantages, the ZnO network has also disadvantages which are the photo(electro)chemical instability of ZnO in aqueous media leading to the high dark currents (Figure 54b), which is inevitable issue. This challenge was circumvented by using ZnO/TiO_2 core/shell structures. Figure 54c shows the LSV curves of a ZnO/TiO_2 film (7 - 10 µm thick) and network (~25 µm high, ZnO wire diameter of 150 nm) photoanodes. For both the network and the film the dark current decreased, and also the light-induced current increased significantly compared to the bare ZnO samples. The photocurrent density value for the network around the potential of 0.7 V vs. Ag/AgCl is 0.3 mA/cm^2 (inset in Figure 54c) which is ~4.5 times higher than for the film electrode (0.065 mA/cm^2).

Since the dimensions of the uncoated (Figure 54b) and TiO_2-coated (Figure 54c) ZnO films and networks are identical, the increased photocurrent must be related to the coating itself and/or the ZnO-TiO_2 interface. Possibly, the built-in electric field at the interface between the ZnO and TiO_2 plays a role. An appropriate band alignment between those two materials should facilitate the efficient charge separation and lead to a minimized recombination rate. It was also shown by Fan *et al.*,[143] that the resistance for the charge transfer from ZnO-based nanowires to the electrolyte is lower in the presence of a TiO_2 shell. The photocurrent increase can be also related to the additional light absorption in the coating layer.

Figure 54 (d) and (e) show the LSV comparison of TiO_2, ZnO and ZnO/TiO_2 films and networks respectively. In both cases, the same trend of increasing photocurrent density is observed. The bare TiO_2-based film and network showed the lowest photocurrent densities, while the highest photocurrent densities were observed for the core/shell ZnO/TiO_2 samples. This trend was also obtained for other similar sets of samples (not shown here), indicating good reproducibility of the data.

For almost all LSV measurements shown in Figure 54, a high cathodic current is recorded at the most negative potential, from where the sweeping of the potential started. To investigate the reason of this increased negative current, LSVs were performed on three different working electrodes without any photoactive material. Figure 55a shows the characteristic LSV curves for a Au rod and a bare Au film (similar to the substrates of the photoanodes from Figure 54) as well as a fluorine doped tin oxide (FTO) substrate. All electrodes measured under the same conditions as for the photoanodes mentioned above. An increased cathodic current upon the application of the initial potential (-0.55 V vs. Ag/AgCl) is observed for all three cases. This effect could be related to the rearrangement of the double layer formed at the interface between the working electrode and the solution. This high cathodic current is observed for each sample independent of the initially applied potential. Figure 55b shows a cyclic voltammogram (CV) of the Au film working electrode, for which the scan was started at -0.55 V vs. Ag/AgCl followed by two additional scan cycles. The initial increase of the cathodic current is not observed for the second and third cycles of the continuous CV scan. Moreover, the current decreased getting close to 0 mA after the first scan. This graph shows that the

observed high negative currents originate from the electrochemical processes taking place on the electrode/electrolyte interface and are not related to hydrogen evolution. Additionally, the small reduction peak observed on the CV curve at ~0.18 V vs. Ag/AgCl is assigned to the adsorption of the SO_4^{2-} ions from the electrolyte onto the Au electrode surface.

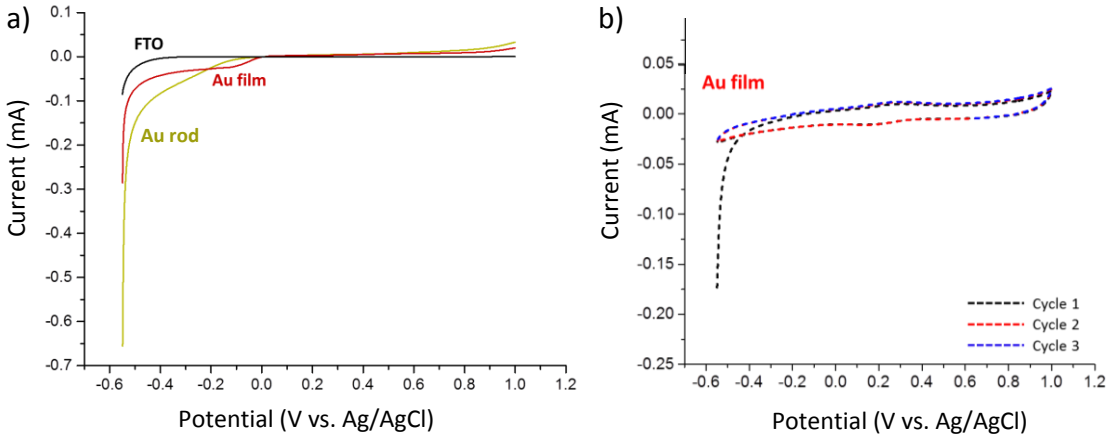

Figure 55: a) Characteristic LSV curves of three working electrodes: Au rod (yellow), Au film (red), and a FTO (black), and b) CV curves of the Au film. All curves were measured in 0.1 M K_2SO_4 (pH 5.6) by sweeping the potential between -0.55 and 1 V vs. Ag/AgCl with a scan rate of 5 mV/s in dark.

The contribution of the TiO_2 layer to the photo(electro)chemical stability of the ZnO in aqueous media was investigated as a function of time by applying a constant potential of 0.62 V vs. Ag/AgCl. The chronoamperometric curves were recorded under chopped illumination (30 s dark, 30 s light). Figure 56a shows the photocurrent measured for the bare ZnO film. A very low photocurrent density was observed from the beginning on, which decreased with time and remained the lowest among four measured samples. The insets show two zoomed-in ranges of the *I-t* curve, evidencing the decrease of the photogenerated current by a factor of 2 within 2 h. This decrease can be related to the photo(electro)chemical corrosion of ZnO, which results in partly decomposition of the photoanode material.

Figure 56b shows the *I-t* curves measured for the ZnO nanowire network photoanode. The initial photocurrent density is higher but unstable. After one hour the photocurrent density was almost two times higher than that of the bare ZnO film, but dark current for this sample increased significantly. In total, the photocurrent decreased by a factor of 4 as compared to the current at the first 10 min of the measurement. This rapid corrosion might originate from access of the electrolyte deep in the network towards the bottom, thus corroding the sample not only on the surface, like in the case of the film, but also attacking the wires from all possible sides. Because of a technical problem with the shutter of the lamp, this sample was only measured for 1.5 h.

The chronoamperometric curve measured for the ZnO/TiO_2 film is shown in Figure 56c. The photocurrent density decreased also by a factor of approximately 2 within 2 hours (see inset in Figure 56c). However, the current density values, being 0.04 and 0.022 mA/cm^2 after 1 and 3 h, respectively, are ~6 times higher than those of the bare ZnO film.

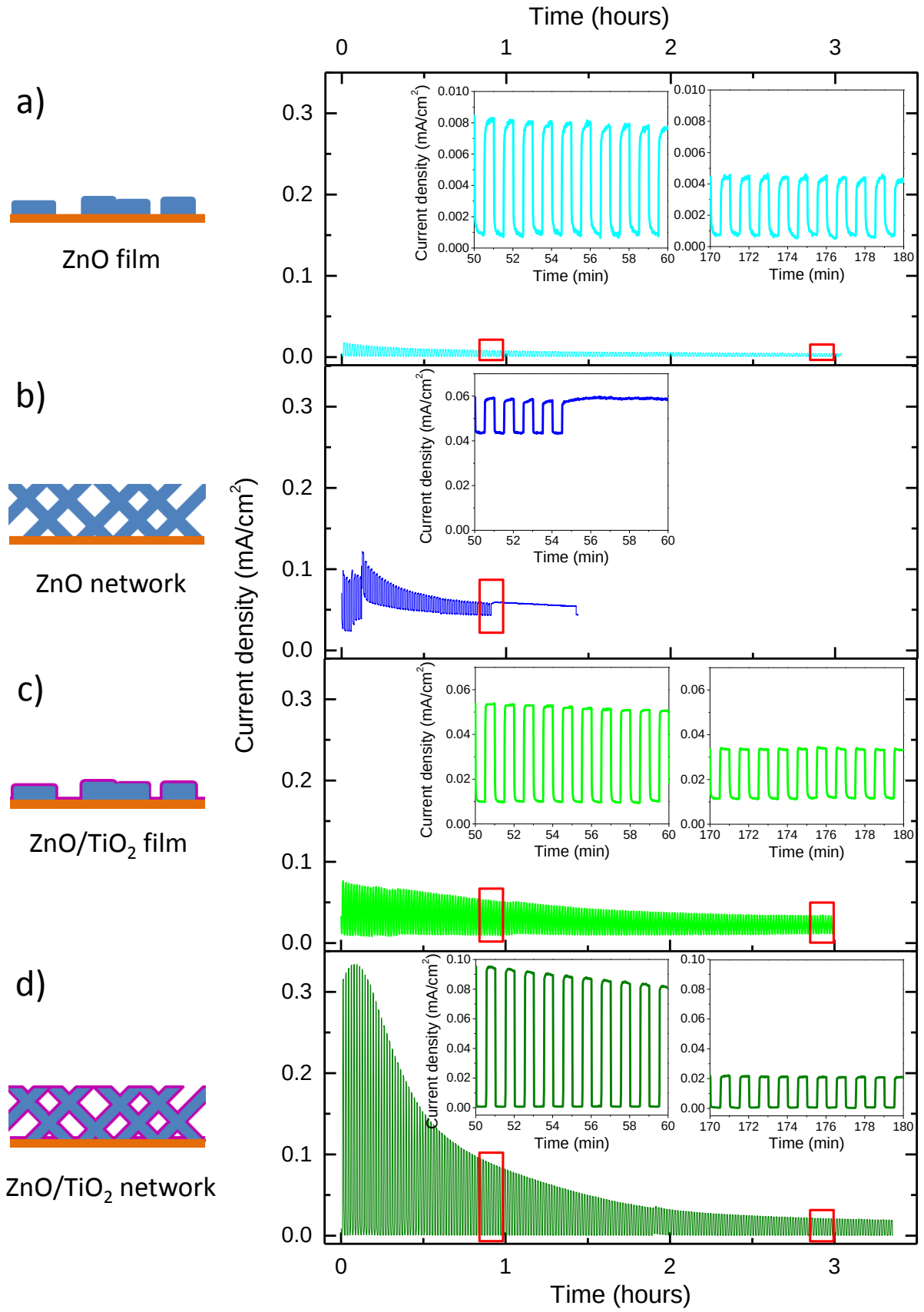

Figure 56: Chronoamperometric (CA) curves of a-b) ZnO and c-d) ZnO/TiO_2 films (a, c) and networks (b, d) measured in 0.1 M K_2SO_4 (pH 5.6) under chopped AM1.5G illumination at 0.62 V vs. Ag/AgCl. The insets represent the zoomed-in ranges of the CA curves after 1 h (left) and 3 h (right).

Finally, Figure 56d reveals that the ZnO/TiO_2 network performs the highest photocurrent both at the beginning of the measurement (~0.33 mA/cm^2) and after 1 h (0.1 mA/cm^2). However, the photocurrent density decreases rapidly with time, and after 3 h of measurement it reaches the value of ~0.02 mA/cm^2, which is comparable to the value for the ZnO/TiO_2 film. The reason for this effect is yet not clearly understood, even though similar behavior was observed for other ZnO/TiO_2 network samples prepared with similar parameters (not shown). A possible explanation is the damaging of the initially homogeneous TiO_2 coating layer, e.g. by breakage of nanowires because of the O_2 bubbles. This would result in the access of the electrolyte to the ZnO core and cause its decomposition, thus reducing the generated photocurrent. However, further measurements are required for more conclusive explanations, e.g. by coupling the PEC cell with a gas chromatography measurement, which would quantitatively characterize the O_2 generation and correlate its relation to the photocurrent density behavior as a function of time.

To investigate the degradation of the measured photoanodes, the surface of the samples was inspected by SEM before and after the PEC measurements (Figure 57). The bare ZnO and ZnO/TiO_2 films do not exhibit obvious changes in the morphology before and after the measurements (Figure 57a,c). Since the thickness of the films was not measured after PEC measurements, is not known at this point whether there was a significant corrosion/decomposition of the ZnO in the electrolyte that could affect the height of the films. Compared to the film photoanodes, the network samples underwent visible changes, which were more significant for the bare ZnO network (Figure 57b). The diameter of the wires in this network decreased from 150 to 120 nm after PEC measurements, and the surface of the wires became very rough, which is an obvious consequence of a corrosion process. Furthermore, in some areas of the network the wires turned into flake-like structures with dimensions in the micrometer range, which might be a result of a recrystallization of ZnO on the surface in the presence of Zn^{2+} and OH^- ions. Besides the decrease in diameter, the height of this network decreased from ~25 to ~10-15 µm, which can be a consequence of the corrosion as well as of shape transformation. Figure 57d shows the SEM images of the ZnO/TiO_2 network before and after the measurements. This system sustained its initial geometry and morphology after PEC measurement, although empty TiO_2 nanotubes were observed in several small areas of the sample (bottom-right image), which is probably related to the decrease of the photocurrent density as shown in Figure 56d. However, since neither the diameter of the wires nor the height of the network changed, it can be assumed that the rest of the wires retained their core/shell shape.

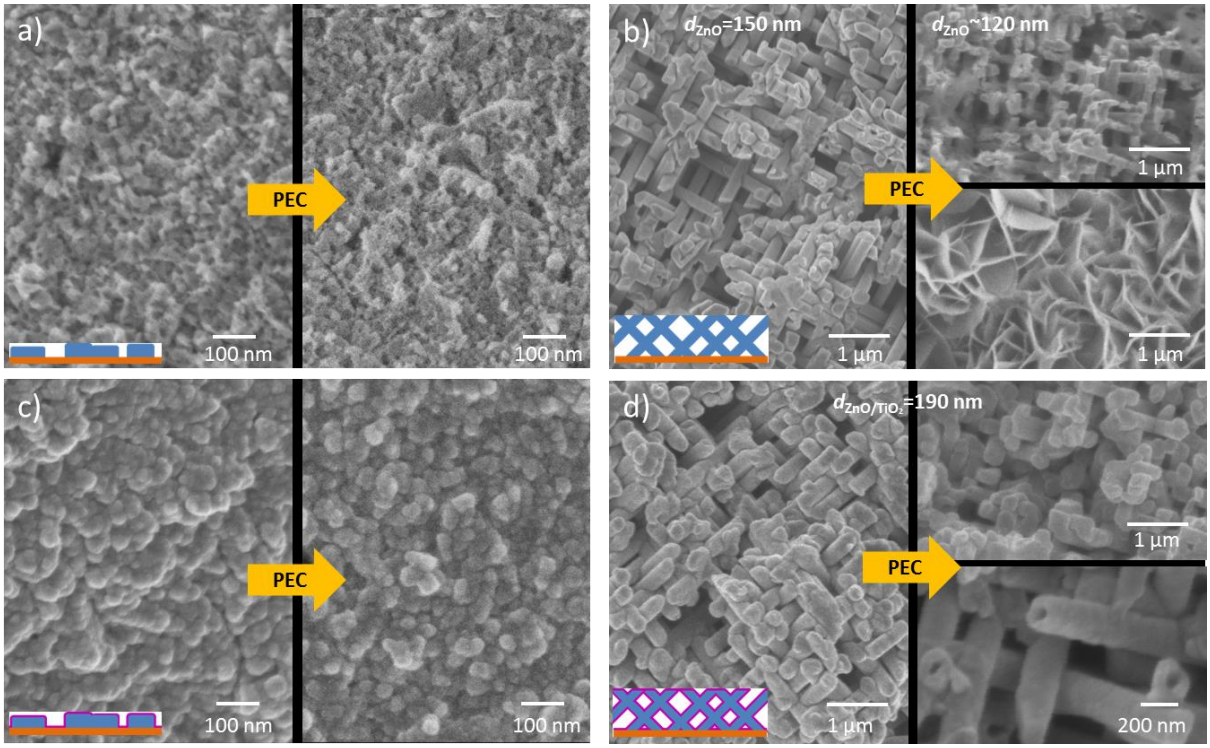

Figure 57: SEM images of a-b) ZnO and c-d) ZnO/TiO_2 film (a, c) and network (b, d) photoanodes before and after photoelectrochemical measurements shown in Figures 54 and 56.

Further investigations are required in order to answer the remaining open questions concerning the PEC performance of the ZnO/TiO_2 nanowire network-based photoanodes. However, the results shown in this thesis reveal that these nanowire-based 3D assemblies ate very promising for further studies as high aspect ratio systems with reduced recombination rate, enhanced light absorption and photogenerated current, especially in the case of novel materials for PEC water splitting and/or as composite/tandem structures.

6.3. XPS analysis of ZnO and ZnO/TiO_2 nanowire photoanodes

For XPS analysis two types of nanowire networks were prepared: (i) a bare ZnO nanowire network consisting of wires with a total density of 8×10^9 cm^{-2} and a diameter of 115 nm, and (ii) a core/shell ZnO/TiO_2 nanowire network with a nanowire density of 3×10^9 cm^{-2} and a ZnO diameter of 190 nm, ALD-coated with 10 nm TiO_2 layer. The reason for the different number density and diameter of the wires was the non-availability of membranes with identical parameters during the experiment preparation. However, the amount of wires is assumed to not influence the characteristic results of the XPS analysis. A 20 nm TiO_2 film on a Au substrate served as reference for ALD coated TiO_2.

XPS was employed to characterize the surface chemistry of photoanodes before and after PEC measurements. It enables the identification of possible surface contaminations that can influence the redox reactions and the PEC performance. In addition of the work function and the valence band position of the TiO_2, ZnO and ZnO/TiO_2 in contact with a Au substrate are deduced. These energy values allow for the determination of the band alignment between

those interfaces, which helps to theoretically explain some of the physical processes taking place in the photoanodes.

ZnO and ZnO/TiO_2 networks were analyzed by XPS in the Surface Science group of Prof. Dr. Wolfram Jaegermann at the Technical University of Darmstadt before and after PEC measurements. The latter were performed the same day to avoid any surface contamination from the environment during their. The TiO_2 coated Au film was also characterized before PEC measurements as a reference for a pure TiO_2 system.

Figure 58 provides an overview of the XPS spectra for all three samples. The survey spectra of the bare ZnO (a) and core/shell ZnO/TiO_2 (b) networks revealed the expected main elements (Ti, Zn, O) on the surface. In addition to these elements, carbon was identified before the PEC measurement. The amount of carbon is higher for the ZnO networks in comparison to the ZnO/TiO_2 networks and the Au coated TiO_2 film. This higher amount of carbon is probably arising from the polymer leftovers on the networks after the dissolution process of the polycarbonate membrane in which the nanowire networks were grown. Since both networks underwent the same cleaning process, the lower intensity of the C peak for ZnO/TiO_2 network in relation to the ZnO network could indicate that the ALD process at a high temperature (250°C) partly removes the polymer residues. It is noteworthy that the intensity of the C peak decreased for both network samples after the PEC measurements. Additional contamination by the presence of a Cl peak was observed only after the measurements. The spectrum of the ~20 nm thick TiO_2 layer on a Au film before the PEC measurement presents a relatively clean surface (Figure 58c). In addition to the core level and Auger peaks of the Ti and O elements, only a very small peak of carbon is observed. This carbon peak is probably related to the adventitious carbon coming from the atmosphere.

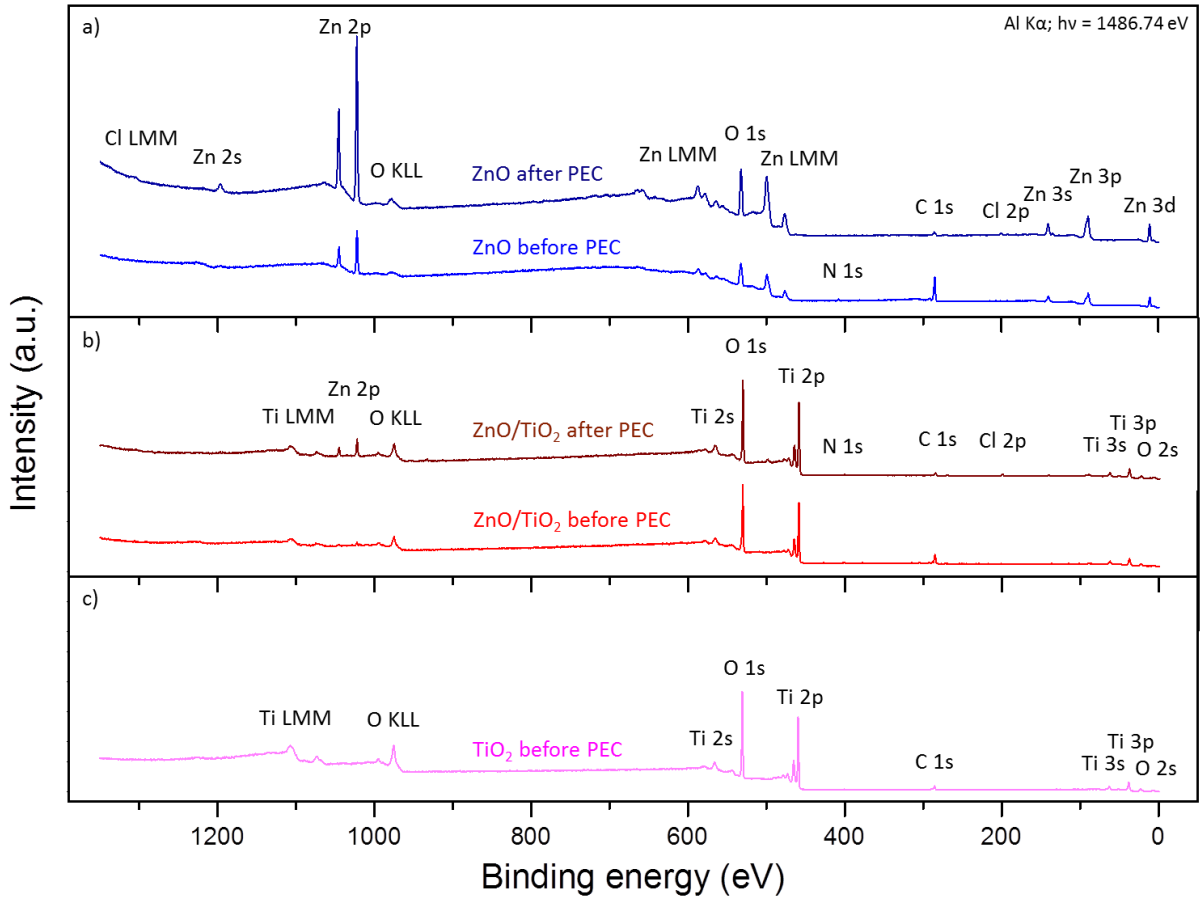

Figure 58: XP survey spectra of the a) ZnO/TiO_2 and b) ZnO nanowire network photoanodes before and after PEC measurements, and c) TiO_2 film before PEC measurement.

The core level spectra of all detected elements are separately shown in Figure 59. The two peaks observed in the Zn 2*p* spectra of the bare ZnO network, which are positioned at binding energies of 1045.15 and 1022.05 eV are ascribed to the Zn $2p_{1/2}$ and $2p_{3/2}$ doublet pair, respectively. Very low Zn 2*p* signals positioned at the binding energies of 1045.74 and 1022.64 eV are observed for the ZnO/TiO_2 network. Before the PEC measurements these peaks are more prominent for the bare ZnO network sample compared to the ZnO/TiO_2 core/shell network which is related to the nominal 10 nm TiO_2 layer coating on it. The presence of several peaks in the C 1*s* core level spectra in the region between 282 and 294 eV for both networks indicate that different chemical carbon species are present on these surfaces. The higher amount of carbon is located at 285 eV, and is assigned to adventitious aliphatic carbon and/or C-H, C-C bondings from the residual polycarbonate of the template. The most intense carbon peak is observed for the ZnO network sample. The shoulder at higher binding energies to the main peak at 286 eV is attributed to C-N bonds. The two other features at 289.5 and 291.4 eV for the ZnO network, and 290.9 and 292.7 eV for the ZnO/TiO_2 network might originate from the presence of polymeric units with C-O bonds from carboxyl and carbonate species from the polycarbonate membrane, respectively. Interestingly, after the PEC measurement the intensity of the Zn 2*p* peaks significantly increased for the bare ZnO network, whereas a strong decrease of the C peaks occurred at the

same time. These observations indicate that the polymer residues are almost completely removed from the surface after the PEC measurements. A slight increase of the Zn 2*p* lines is also observed for the ZnO/TiO_2 networks sample. Moreover, the intensities of the Ti *2p* peaks corresponding to $2p_{1/2}$ and $2p_{3/2}$ photoelectron lines positioned at 465 and 459.2 eV also increased after the PEC measurement. No shift was observed toward pure Ti lines (expected at 460 and 454 eV for $2p_{1/2}$ and $2p_{3/2}$, respectively) which indicate that no corrosion occurred in the TiO_2 film. The Ti $2p_{1/2}$ and $2p_{3/2}$ peaks of the pure TiO_2 layer are also presented in Figure 65, and perfectly match with those of ZnO/TiO_2 network. As expected, no Ti signal was recorded for the bare ZnO network.

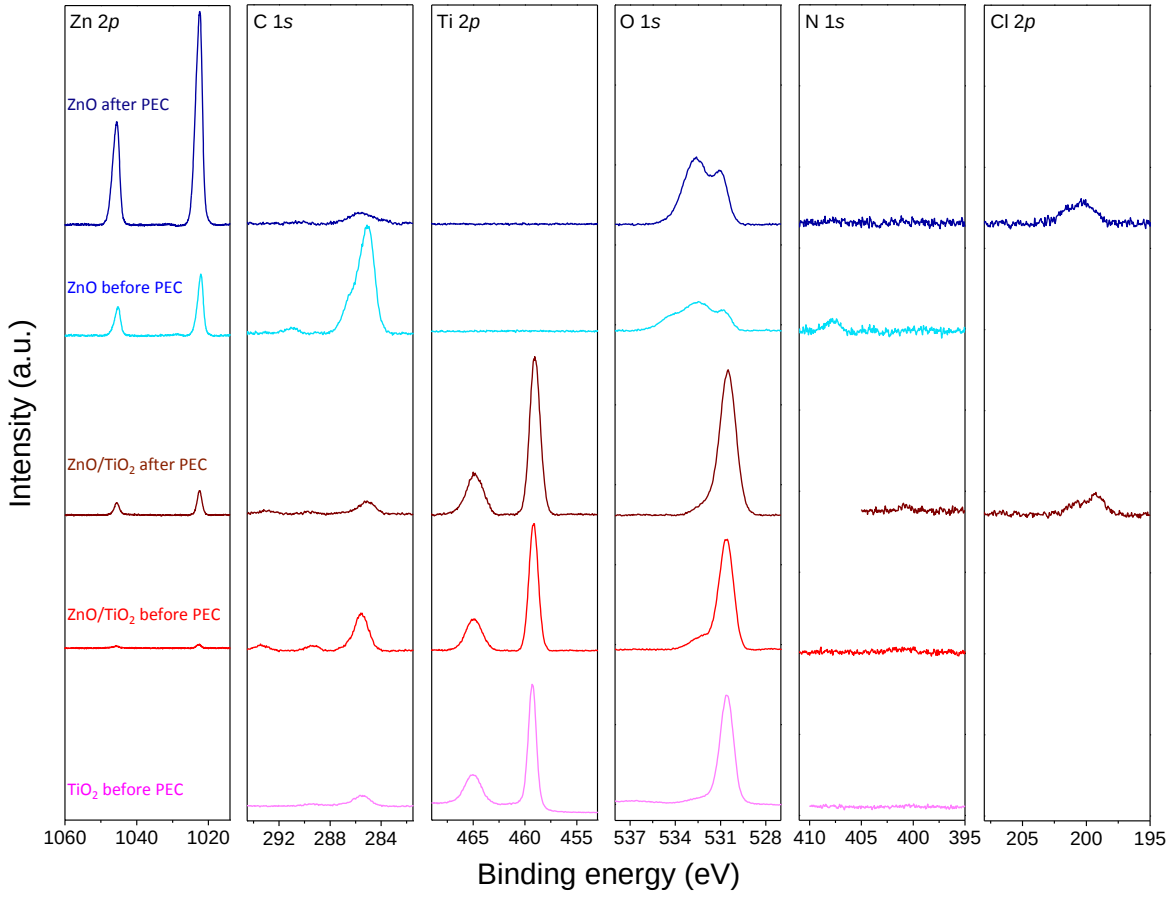

Figure 59: Core level photoelectron spectra of ZnO nanowire network in blue and royal before and after PEC measurements, respectively, ZnO/TiO_2 nanowire networks in red and wine correspondingly before and after PEC measurements, and TiO_2 film in pink before PEC measurement.

The O 1*s* lines at 531 and 530.5 eV, measured for pure ZnO and TiO_2-coated samples, respectively, correspond to metal oxides. The peaks and shoulders at the region of ~532.4 eV most probably originate from hydroxides, while the peak at 534.38 eV observed only for the ZnO network before PEC measurement can be related to polycarbonates. Alternatively, it can be also assigned to nitrates as N was observed for this sample before PEC measurement at 407.7 eV. The N 1*s* core level revealed also another peak at 399 eV corresponding to N-H bondings. These contaminations with nitrogen probably originate from the nitrate based electrolyte used for the electrodeposition of the ZnO nanowire networks. A small peak of N

1*s* core level is observed also for ZnO/TiO_2 network, which becomes slightly more prominent after the PEC measurement. Since the bare TiO_2 film was free of any nitrogen contamination, the N 1*s* signal present for the ZnO/TiO_2 network supports its origin from the nitrate based solution for ZnO electrodeposition. After the PEC measurements Cl $2p_{3/2}$ and $2p_{1/2}$ lines were also observed for the ZnO/TiO_2 sample at 199.22 and 200.8 eV, respectively, and at 200.21 and 201.47 eV for the ZnO network. Since the Cl peaks were not observed on the survey curves before the PEC measurements, the reason for Cl contamination can be assigned to the immersion of the Ag/AgCl reference electrode into the PEC cell without sufficient rinsing of the KCl in which the electrode was stored.

The quantitative analysis of the elements observed in ZnO and ZnO/TiO_2 network samples is shown in Table 1. The numbers represent the atomic concentration in %. Since contaminations from C, N, and Cl species are present on the surface of the networks, these experiments should be repeated with fresh and cleaner samples to get more precise chemical analysis of the Zn, Ti and O concentrations.

Table 1: Atomic concentrations (%) of the elements observed on the surface of ZnO and ZnO/TiO_2 networks by XPS before and after PEC measurements.

Element / Network sample	Zn	C	Ti	O	N	Cl
ZnO (before PEC)	9.3	56.7	-	32.5	1.5	-
ZnO (after PEC)	35.4	9.3	-	53.1	0.3	1.9
ZnO/TiO_2 (before PEC)	0.6	23.5	23.1	52.4	0.6	-
ZnO/TiO_2 (after PEC)	3.6	8.1	26.9	59.7	0.3	1.4

In addition to the chemical compound analysis by XPS, the secondary electron cut-off and valence band regions were recorded to determine the work function (WF) and the valence band maximum (VBM), respectively. The results are shown in Figure 60. The valence band onset is located at 3.15 and 3.2 eV for the ZnO nanowire network and TiO_2 film, respectively. Their work functions (WF) before the PEC measurement were found to be 4.35 and 4.05 eV, respectively. The optical band gaps (measured by UV-Vis) of ZnO nanowires and ALD coated TiO_2 layer were estimated to be 3.28 and 3.3 eV, respectively. Considering the values measured for the valence band onset of both samples, highly n-doped materials were obtained by the prepared methods.

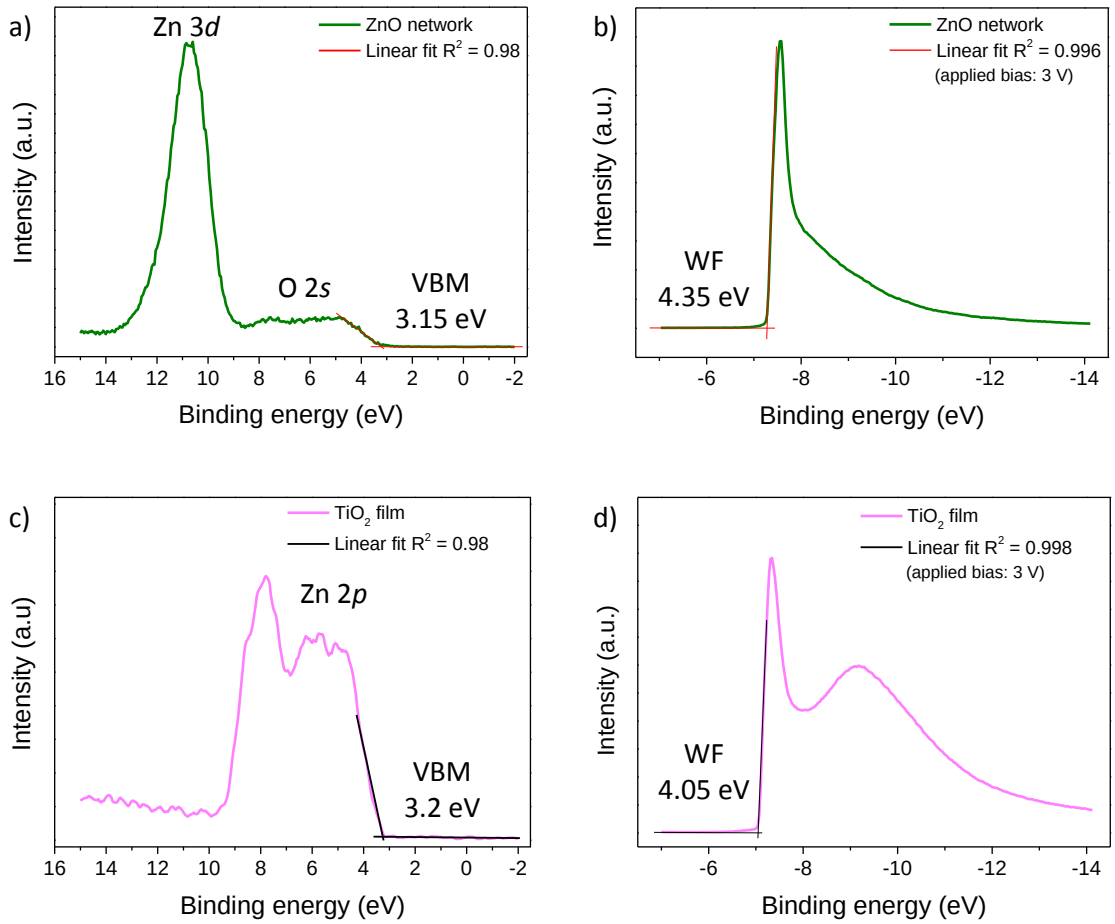

Figure 60: Valence band spectra of a ZnO nanowire network (a) and a TiO_2 film (c) showing the valence band maximum (VBM) at 3.15 and 3.2 eV for ZnO and TiO_2, respectively, as well as their secondary electron cut-off (b and d) from which the respective work functions (WF) of a ZnO and TiO_2 were found to be 4.35 and 4.05 eV. For the secondary electron cut-off, a voltage bias of -3V is applied.

It should be mentioned, that although the XPS of the ZnO-based sample was measured on a nanowire network system, the band gap value of ZnO was defined from a UV-Vis measurement of nanowires from a nanowire array (not from the same network) since the preparation of the network samples for the UV-Vis measurement is much more challenging. However, the values for both the ZnO and TiO_2 mentioned above are in a very good agreement with those reported in literature.[109,110] Based on the band gap, valence band maximum and work function values of ZnO and TiO_2 (determined in this thesis), the schematics of the band alignment with a Au contact are presented in Figure 61. For the polycrystalline Au substrates a work function of 5.1 eV was estimated.[146] Both the ZnO and TiO_2 samples create a Schottky contact with the Au substrate. The Schottky barrier at the Au-ZnO contact is found to be slightly smaller than that of the Au-TiO_2 system. A Schottky barrier of 0.88 eV and band bending of 0.75 eV are determined for the Au-ZnO sample, while the Au-TiO_2 contact reveals a barrier of 1.15 eV and band bending of 1.05 eV. If the depletion region at the metal-semiconductor interface is sufficiently thin (2-5 nm) the electrons will

tunnel rather than transport over the Schottky barrier thus preventing recombination and resulting in a higher detectable current.

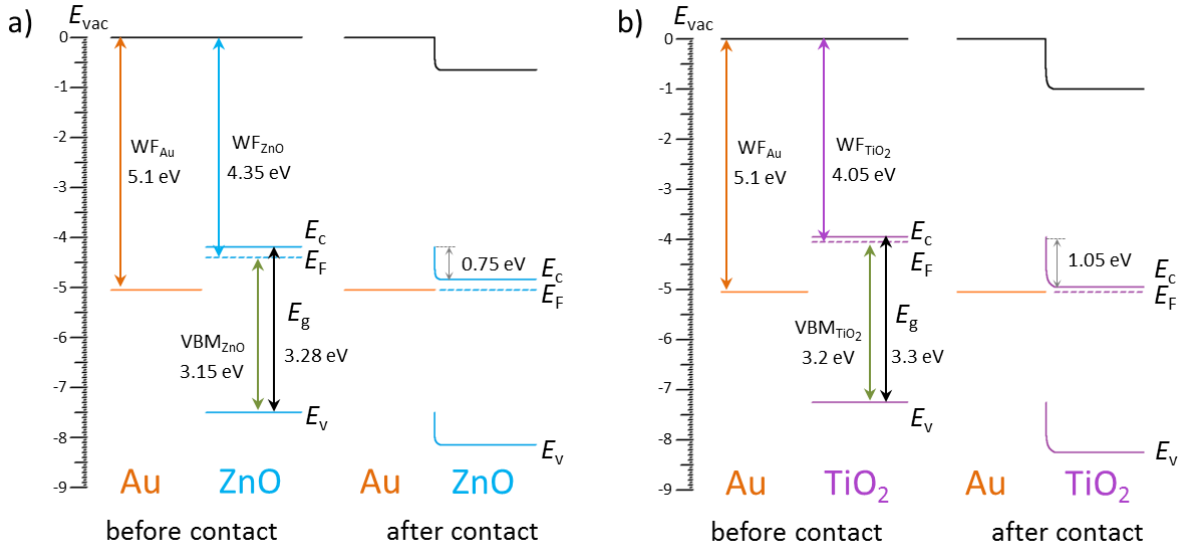

Figure 61: Schematics of the band alignment of a) a Au-ZnO and b) a Au-TiO_2 systems before and after contact (theoretical estimation).

However, it is important to mention that the schematics shown in Figure 61 are only theoretical estimation. To build the band of the semiconductor-metal interface, the semiconductor should be measured before and after the metal deposition on its surface, which will provide a more precise determination of the band-bending at the interface.

In conclusion, XPS was successfully applied to characterize the surface of ZnO and ZnO/TiO_2 nanowire networks before and after PEC measurements. The spectra taken at the secondary electron cut-off and valance band regions allowed for estimating the band alignment of the Au-ZnO and Au-TiO_2 contacts. Unfortunately, a significant surface contamination with carbon was observed due to incomplete dissolution of the polycarbonate membrane. The cleaning process plays a crucial role and needs to be improved when aiming at analyzing the Zn, O and Ti concentrations in these networks.

Summary and Outlook

In this thesis ion-track technology in combination with electrochemical deposition was employed to grow ZnO-based nanowire arrays. 3D networks of interconnected wires were developed in order to obtain mechanically stable structures with high surface area which are promising for device implementation in the fields of energy conversion and storage, sensorics and electronics.

By applying various templates and deposition conditions ZnO cylindrical nanowires with tailored aspect ratio, morphology and crystallographic properties were synthesized. Nanowires with diameters between 45 and 250 nm are successfully grown using a $Zn(NO_3)_2 \cdot 6H_2O$ solution at 80˚C. Arrays with a wire length of 7-10 µm and diameters between 150 and 250 nm were stable and self-supporting. In contrast, the nanowires with diameters below 150 nm and length above 20 µm show pronounced bending. Nanowires electrodeposited inside identical templates under the same applied potential and temperature exhibit smooth surface when a low concentration of the electrolyte was used. X-ray diffraction (XRD) patterns revealed a hexagonal wurtzite structure for all analyzed nanowires. The influence of the electrodeposition potential on the crystallographic properties of the nanowires with fixed diameter (250 nm) was studied by growing nanowire arrays at potentials between -0.5 and -0.8 V vs. Ag/AgCl. The texture coefficients (TC) of $(10\bar{1}0)$ planes deduced from XRD diffractograms slightly increase for higher potentials. An exception is -0.8 V vs. Ag/AgCl; at this value the texture changes and TC $(11\bar{2}0)$ becomes more dominating compared to the wires grown at lower potentials. In another series, nanowires with diameters between 45 and 160 nm were fabricated at a fixed potential of -1 V vs. Ag/AgCl. The arrays of nanowires with diameters below 85 nm show no preferred orientation, and those with a diameter of 85 nm exhibit a slight $(11\bar{2}0)$ texture. In contrast, the nanowires with a larger diameter (~160 nm) show a $(10\bar{1}0)$ texture. Although the TCs have moderate values, these studies evidence that both, diameter of the nanopores and applied potential, influence the crystallographic properties of the electrodeposited ZnO nanowires.

Conical ZnO nanowires were grown potentiostatically using a 0.1 M $Zn(NO_3)_2 \cdot 6H_2O$ electrolyte at 80˚C and an applied potential of -0.8 V vs. Ag/AgCl. Two growth approaches were used: base-to-tip and tip-to-base. In both cases XRD diffractograms reveal a polycrystalline structure with no preferred orientation. The wires grown from the large base of the membrane pores (diameter of ~2.5 µm) to the small tips (diameters between 70 and 120 nm) have a smooth surface and a tubular shape along the first ~15 µm from the base, which weakens their mechanical stability. The tip-to-base growth under the same electrodeposition conditions results in nanocones with a more complex shape consisting of arbitrarily positioned grains and nanowalls leading to a rough surface and easy breaking of the cones. Due to the large base, the conical shape of the wires is promising for arrays regarding enhanced mechanical stability. However, the deposition of ZnO conical nanowire arrays

raises new questions about the growth mechanism and requires further investigation.

Mechanically stable 3D ZnO nanowire networks were grown in templates with interconnected nanochannels. Optimal conditions for electrodeposition of homogeneous nanowire networks are found to be 0.1 M $Zn(NO_3)_2 \cdot 6H_2O$ electrolyte at 60˚C and potentials of -1.4 V and -1 V vs. Ag/AgCl for samples with Cu and Au substrates, respectively. Homogeneous filling is obtained for structures grown in membranes irradiated from five directions (four under 45˚ and one parallel to the surface normal). Applying an irradiation mask with limited irradiation area prevents the leakage of the electrolyte during electrodeposition which additionally facilitates the homogeneous growth of the networks. SEM analysis showed that the nanowires in the networks possess smooth surfaces and faceted tips. High resolution transmission electron microscopy (HRTEM) and high-angle annular dark-field imaging (HAADF) performed on segments of nanowires extracted from the networks reveals well-ordered and continuous (0002) and $(10\bar{1}0)$ planes up to a µm range. XRD analysis shows a polycrystalline pattern with five more reflection peaks for the complete network. Since the pores in the network are tilted with respect to the surface normal and the wires grow in several directions, it is challenging to draw a final conclusion about the crystallinity and texture based on their XRD patterns. Different measurement methods (e.g. tilting or rotating the samples) on tilted wires having only one direction would clarify this open question.

Core/shell ZnO/TiO_2 nanowires arrays and nanowire networks were prepared by coating the samples with thin TiO_2 layers by atomic layer deposition (ALD) at 110 and 250˚C, respectively. Electron energy loss spectroscopy (EELS), HRTEM and HAADF studies confirm the conformal and homogeneous coating of the wires. The coating at 110˚C results in amorphous TiO_2 shells, while the ALD process at 250˚C leads to a crystalline TiO_2 layer with anatase phase consisting of mainly (101) planes.

Pure ZnO and core/shell ZnO/TiO_2 3D nanowire networks were used as photoelectrode model systems for photoelectrochemical water splitting. All nanowire network systems exhibit increased light-induced photocurrents compared to their film counterparts. The highest photocurrent (~0.3 mA/cm^2) was recorded for the ZnO/TiO_2 core/shell nanowire network. The built-in field formed at the ZnO/TiO_2 interface facilitates the photogenerated charge separation, and the presence of the TiO_2 shell may provide a lower resistance for the charge transfer from nanowires to the electrolyte. SEM analysis of the network surfaces before and after long-term chronoamperometric measurements show a good photo(electro)chemical stability (no surface modifications) for ZnO photoelectrodes coated with ~20 nm TiO_2. In contrast, the uncoated networks undergo pronounced modifications, including the reduction of the nanowire diameter, surface roughness and recrystallization of the wires in a new geometry. These results highlight the important role of the TiO_2 coating for photocurrent enhancement and corrosion protection.

In order to get a better insight into the surface corrosion effects, X-ray photoelectron spectroscopy (XPS) was employed to TiO_2, ZnO, and ZnO/TiO_2 photoanodes. The results showed that the TiO_2 coating was free of contamination, while the surface of the ZnO nanowires in the networks initially exhibited impurities of carbon and nitrogen. The latter elements are assigned to residues from the polymer matrix and nitrate-based electrolyte for electrodeposition, respectively. Both the carbon and nitrogen signals vanished after the photoelectrochemical measurements, indicating that the contamination was only on the surface which can be avoided by optimizing the cleaning process during sample preparation. The work function and valence band position of the ZnO and TiO_2 samples (grown on Au substrates) deduced from XPS measurements were used in order to theoretically estimate the Schottky barrier height formed at the ZnO-Au and TiO_2-Au contacts. It was proposed that a thin depletion region is formed in these systems and thereby tunneling process occurs readily.

In conclusion, this thesis provides important and new information about template-assisted electrodeposition of ZnO nanowires, in particular regarding tuneable parameters and properties such as number density, aspect ratio, morphology and crystallinity.

For applications of ZnO nanowires in piezoelectrics, electronics, sensors, photovoltaic devices and photoelectrodes, highly crystalline nanowires are required. To increase the texture of cylindrical nanowires, a wider range of electrodeposition potentials and diameters compared to this work should be investigated. Particularly, for piezoelectric devices the conical geometry of the wires is of great interest because the piezoelectric properties change depending on the nanowire diameter. However, the synthesis of conical nanowires presented in this thesis is in its early stage and requires further studies to improve the filling inside the conically-shaped pores. To deposit continuous and solid cones, pulsed electrodeposition should be tested. Membranes with conical nanopores combined with a network at the base can be used to enhance the mechanical stability of the conical ZnO nanowire arrays. Such membranes have been already introduced in this work. Due to the high surface area, the decreased path length of the charge carriers to the wire surface and the enhanced light absorption, nanowire-based 3D network structures, as presented here, are very promising as photoelectrodes for photoelectrochemical water splitting. The increased light-induced photocurrents for ZnO and ZnO/TiO_2 networks compared to their film counterparts show that these 3D nanoarchitectures are of great interest for further investigation provided that materials more suitable for water splitting application are used. The nanowire diameter and height of the networks should be optimized depending on the light-absorption range for a given material. Finally, it would be very interesting to use these nanowire networks for gas sensors. However, as the sensing properties are strongly influenced by surface impurities, a more efficient procedure of the membrane dissolution from electrodeposited networks has to be established.

Appendices

A: Etching rates of network based membranes

Figure A1 shows the etching rate values vs. time for membranes which were irradiated with Au heavy ions (11.1 MeV/u, nominal fluence of 5×10^{8} cm^{-2}) and etched in 6M NaOH at 50˚C. A reference sample was used to calculate the number of pores per area which resulted in a pore number density of 3.1×10^{9} cm^{-2}.

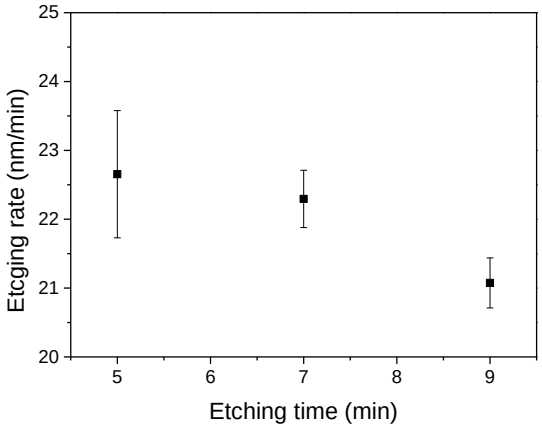

Figure A1: Etching rate vs. time dependence of the network based membranes with an ion-track nominal density of ~5×10^{8} cm^{-2}.

B: ZnO nanotube networks by electrochemical deposition

During the optimization of the electrodeposition parameters for the ZnO nanowire networks, a growth of ZnO nanotube networks was observed. Two independent parameters influenced the tubular growth: the large diameter of the pores and the increased concentration of $Zn(NO_3)_2\cdot6H_2O$ electrolyte. In one case, the deposition was carried out using 0.1 M electrolyte in pores with a diameter of 300 nm. In the other case, the structures were grown from 1 M $Zn(NO_3)_2\cdot6H_2O$ in 200 nm pores. The density of the pores was 2×10^{9} cm^{-2} in total. For both cases, a potential of -1.4 V vs. Ag/AgCl at 60˚C was applied.

Figure B1a shows a low magnification SEM image of a sample grown in pores with a diameter of 300 nm, where two areas can be distinguished that are separated with a white dashed line. The area on the left seems to consist of nanowires, while the structure on the right consists of a network of nanotubes. A high magnification image of an area similar to the one marked with the green square is shown in Figure B1b. The surface looks smooth for the majority of the wires, while the tips have a roughness. However, the shape of the tips infers that the wires within this area are solid. Another high magnification image of the same sample is shown in Figure B1c. It is obvious, that the network consists of hollow ZnO nanotubes. This result is in agreement with observation of Sima *et. al*. [46] that ZnO can be grown as tubes in large pores at low temperatures (< 100˚C).

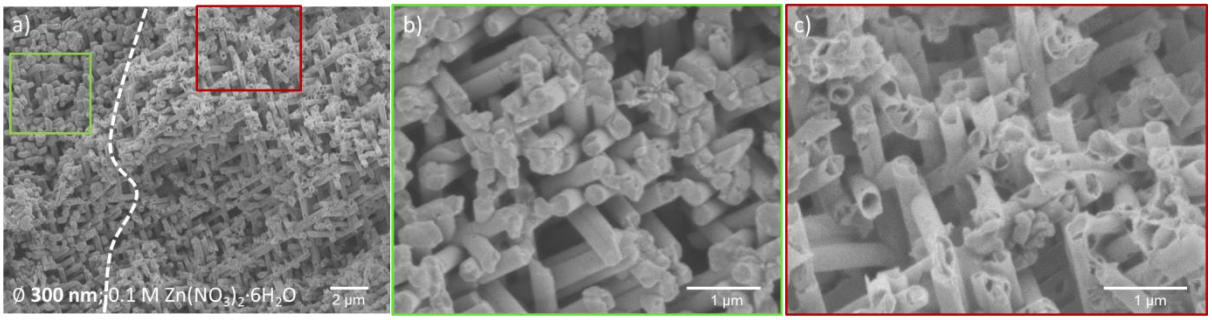

Figure B1: a-c) SEM images of ZnO network synthesized in a membrane with a pore-density of 2×10^9 cm^{-2} and diameter of 300 nm. The electrodeposition was carried out -1.4 V vs. Ag/AgCl and 60˚C from 0.1 M $Zn(NO_3)_2\cdot6H_2O$ electrolyte. The network consists of both nanowires (b) and nanotubes (c).

Another approach to obtain ZnO nanotube network was the increase of the electrolyte concentration to 1 M, with the expectation that the fast growth rate will result in a tubular structure. This assumption was confirmed with the deposition of ZnO in a membrane with 200 nm pores. Figure B2 (a) and (b) show SEM images of these nanotube networks in low and high magnification. The tubes are mainly continuous and homogeneous, although on some of the tubes cracks or small holes can be observed. The EDX spectrum shown in Figure B2c proves that the nanotubes consist of Zn and O. The increased concentration of the electrolyte obviously does not lead to the deposition of pure Zn.

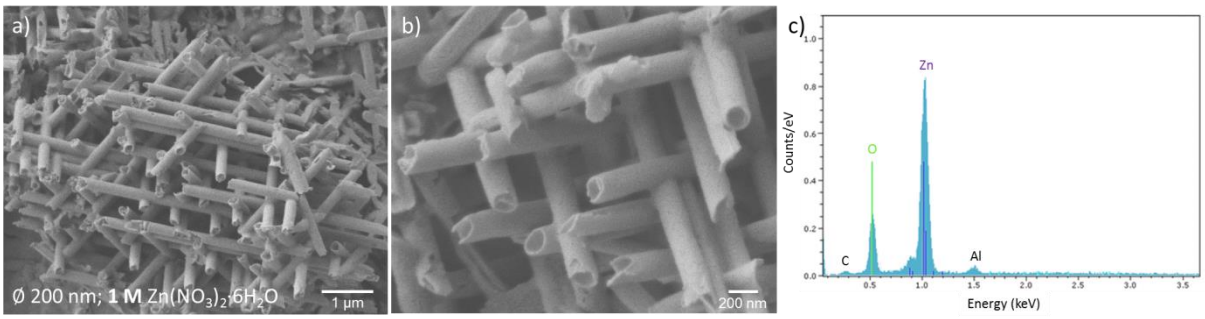

Figure B2: a,b) SEM images of ZnO nanotube network synthesized in membranes with a pore-density of 2×10^9 cm^{-2} and diameter of 200 nm. The electrodeposition was carried out at -1.4 V vs. Ag/AgCl and 60˚C from 1 M $Zn(NO_3)_2\cdot6H_2O$ electrolyte. c) EDX spectrum of the nanotube network, which confirms that the wires consist of zinc oxide and not of pure metallic zinc.

These results are a starting basis for further investigation of ZnO nanotube networks with increased surface area, e.g. for gas sensors. Systematic studies are required to establish a reproducible growth, get knowledge about the crystallinity, and understand how the wall thickness of the tubes can be controlled during electrodeposition.

C: TiO_2 nanotube networks by atomic layer deposition

Atomic layer deposition (ALD) is a straightforward method to synthesize nanotubes of controlled wall thickness. In collaboration with Anne Spende (Materials Research Department at GSI) and the group of Prof. Dr. Kornelius Nielsch (Univesität Hamburg) 30 µm membranes with network channels (nominal density of 4×10^9 cm^{-2}, diameter of ~230 nm)

were coated with a ~10 nm TiO_2 at the University of Hamburg. The deposition was carried out at 95˚C with cycles consisting of (i) a pulse of titanium tetraisopropoxide (TTIP, $C_{12}H_{28}O_4Ti$) as first precursor, (ii) consecutive purging with N_2 to remove the leftover molecules, (iii) a pulse of H_2O as second precursor, and (iv) consecutive purging with N_2. These four steps represent one deposition cycle and result in the deposition of a conformal coating of a monolayer of TiO_2. By varying the number of the cycles, the thickness of the tube walls can be precisely tuned. The growth rate under the mentioned ALD conditions was 0.04 nm/cycle. More details can be found in [58]. To visualize the nanotube network, a Cu back -electrode was electrodeposited on one side of the membrane after the ALD coating, and the polymer matrix was removed by dissolution in CH_2Cl_2. Figure C1 shows SEM images of the TiO_2 nanotube network in a) very low, b) high, and c) very high magnifications. The conformal coating of ALD resulted in a continuous and stable TiO_2 network with a total size of ~2.5 cm in diameter. The higher magnification images (b, c) show that the structure consists of interconnected tubes with homogeneous walls.

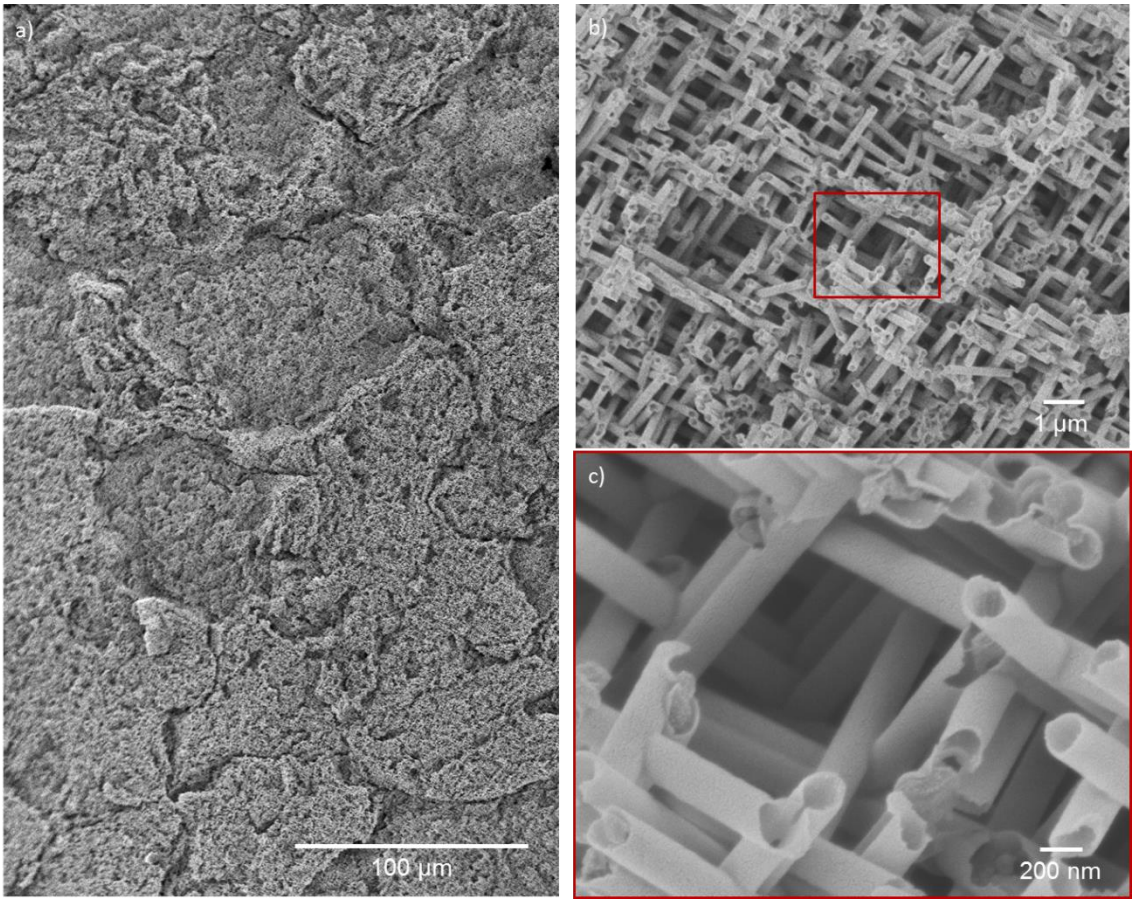

Figure C1: SEM images of TiO_2 nanotube network synthesized by atomic layer deposition in network membrane with a pore-density of 4×10^9 cm^{-2} and a diameter of ~230 nm. The images show a) a stable and continuous network b) with perfect interconnections and c) homogeneous 10 nm thick tube walls.

D: Si nanowire networks

Amorphous Si nanowire networks were synthesized in membranes with network channels (number density of 4×10^9 cm^{-2}, diameter of 150 nm) in collaboration with Dr. Jeremy Mallet from UFR Sciences Exactes et Naturelles Lab. de Recherche en Nanosciences in Reims (France). The deposition of the Si networks was carried out from an electrolyte based on $SiCl_4$ and a 1-butyl-1-methylpyrrolidinium bis(trifluoromethylsulfonyl)imide ($[Py_{1,4}]TFSI$) ionic liquid at a temperature of 70˚C.

Figure D1 shows the SEM images of the grown Si networks after the dissolution of the polymer matrix. Figure D1a shows the top view of the network revealing a homogeneous growth of the network. Figure D1b shows the cross section of the Si nanowire network under a tilt.

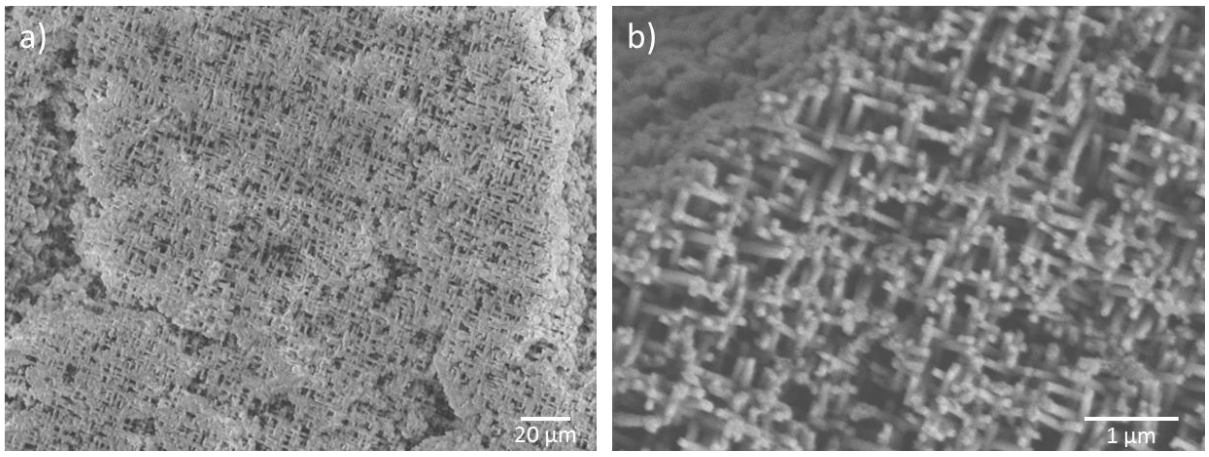

Figure D1: SEM images of a) a top view of the Si nanowire network with a wire number density of 4×10^9 cm^{-2} and a diameter of 150 nm, b) cross sections of the network under a tilt.

The EDX spectrum of the corresponding network is shown in Figure D2. The Si and O signals originate from the nanowire network, the Au and Cu are assigned to the sputtered and electrodeposited back-electrode. A small signal of Cl is detectable which is assigned to a residual contamination from the $SiCl_4$ electrolyte. The C and Al peaks correspond to leftover polymer from the membrane and the sample holder, respectively.

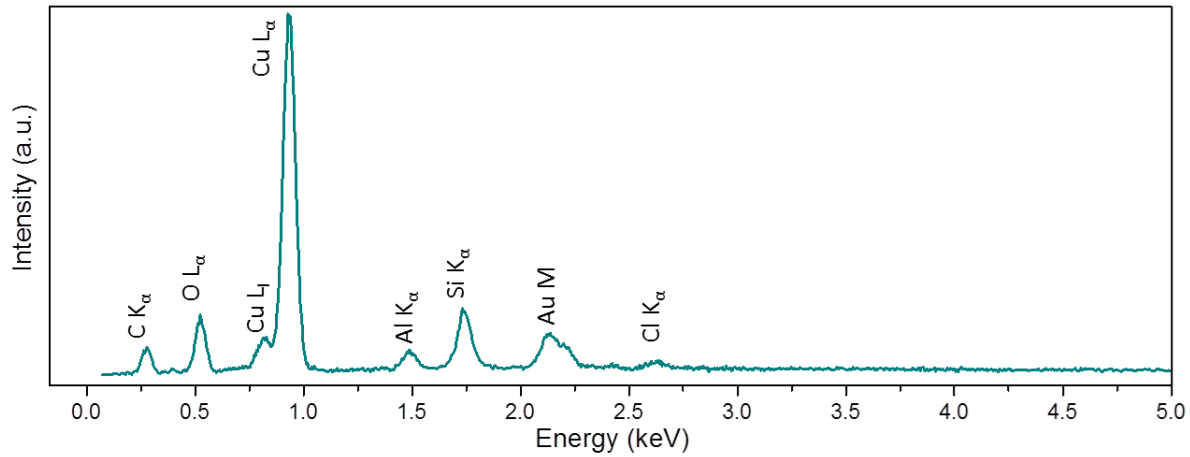

Figure D2: EDX spectrum of a Si nanowire network grown from a $SiCl_4$ - and $[Py_{1,4}]TFSI$ ionic liquid-based electrolyte at 70˚C.

First photoelectrochemical measurements of these amorphous Si nanowire network showed small anodic currents in a range of a few tens of $\mu A/cm^2$ upon illumination of the samples. This means that the as prepared Si network has slight n-type conductivity. However, for a better performance these nanowire networks must be annealed to obtain better crystallinity. Si exhibits advanced optical properties and high absorption in visible region of sunlight which combined with the nanowire network geometry makes it more attractive for future studies for photoelectrochemical water splitting.

E: Sample preparation for TEM measurements

Figure E1 shows SEM images of the Au-TEM grid with pieces of ZnO/TiO_2 nanowires extracted from the networks. Since the wires were transferred onto the TEM grid by rubbing the TEM grid over the sample, the lacey-carbon film is damaged in some parts (Figure E1a, dark cells). However, there are enough non-damaged areas with either single or multiple wires. In Figure E1 (b) and (c) the white dots on the carbon layer are the wires. SEM images in higher magnification are shown in Figure E1 (d) and (e). The white arrows indicate intersecting wires which would allow for analysis of the coating homogeneity by TEM.

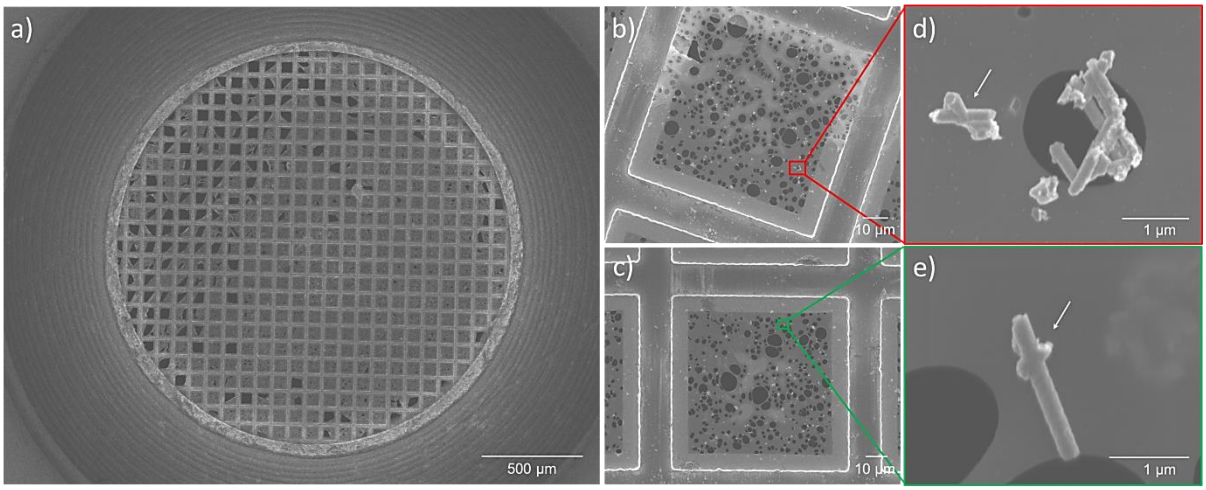

Figure E1: SEM images of a) a Au-TEM grid after the ZnO nanowires were transferred onto it; b, c)

patches of the grid full with wires, here looking as small white dots; d, e) nanowires on lacey-carbon layer of the TEM grid in higher magnification, where the arrows indicate wires which are still interconnected after breaking the wires from the network.

F: Au nanowire networks

Au nanowire network was electrodeposited using a gold sulphite electrolyte at 60˚C by applying -0.7 V vs. Ag/AgCl. A two-electrode setup was used, where a Au rod served as anode, and the membrane with a nanochannel network and a metallic substrate was the cathode.

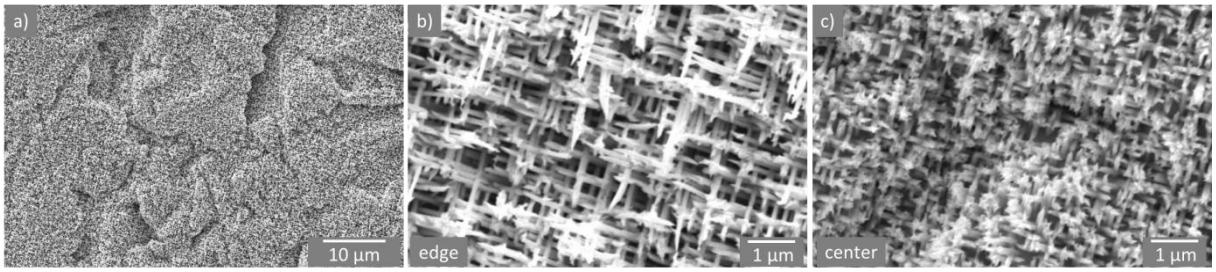

Figure F1: a) A low magnification SEM image of a Au nanowire network synthesized in a membrane with a pore total density of 8×10^9 cm^{-2} and a diameter of 150 nm, using a gold sulphite bath at 60˚C by potentiostatic growth at -0.7 V vs. Ag/AgCl, and b-c) high magnification SEM images of the Au network showing a favorable growth at the edges (b) and a thin network layer in the center of the sample (c).

G: PEC measurements of ZnO/TiO_2 network with tuned wire diameters

To optimize the nanowire diameter in the ZnO nanowire networks for photoelectrochemical measurements, series of networks with wire diameters of 115, 150 and 190 nm were synthesized and coated with ~4, ~10 and ~20 nm anatase-TiO_2 layers. For series of samples coated with ~4 nm TiO_2, the photocurrent was increasing with the increase of the diameter (Figure G1). The reason can be related to the higher texture of the ZnO nanowires with a larger diameter, and hence, a better transport of the charge carriers in those wires. However, the chronoamperometric measurements showed that the ~4 nm TiO_2 coating does not completely protect the ZnO core from corrosion during a long term measurements (Figure E2, red curve). In contrast to this, the nanowire networks coated with 20 nm TiO_2 showed a better photo(electro)chemical stability, but the photocurrent decreased for the thick wires because of decreasing space between the wires in the network (Figure E2, violet curve). A modest photocurrent and sufficient stability was obtained for nanowire networks with a wire diameter of 150 nm and ~10 nm TiO_2 layer. With these optimization experiments the limit of minimum coating thickness for a moderate stability against photo(electro)chemical corrosion was found to be ~10 nm. In future, these experiments must be repeated for wires with a wider range of

diameters and coating thicknesses, and for the explanation of the phenomena happening in the samples a simplified Au/TiO_2 core/shell nanowires and networks should be employed.

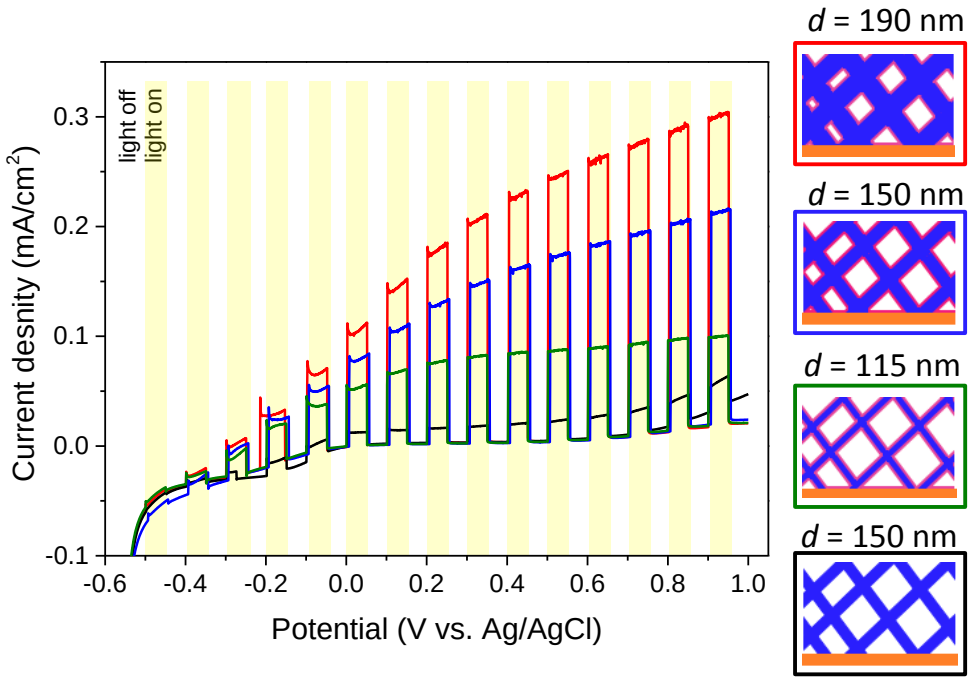

Figure G1: Characteristic linear sweep voltammetry of ZnO and ZnO/TiO_2 (ALD, 4 nm) photoanodes under a chopped illumination (AM 1.5) with a scan rate of 10 mV/s in 0.1 M K_2SO_4.

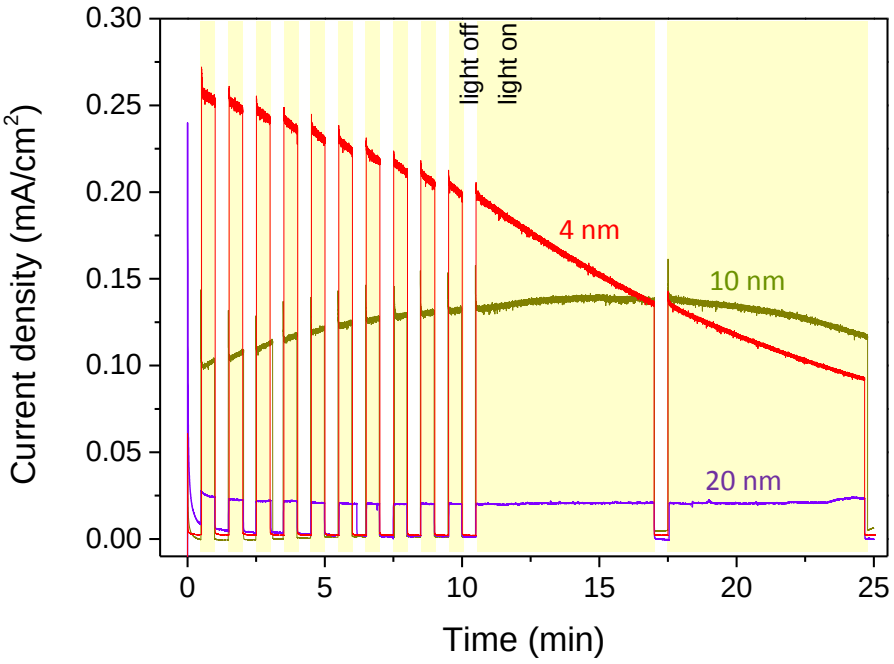

Figure G2: Chronoamperometric curves of core/shell ZnO/TiO_2 photoanodes with a ZnO core diameter of 190 nm under a chopped illumination (AM 1.5) and applied potential of 0.62 V vs Ag/AgCl in 0.1 M K_2SO_4. The red, dark yellow and violet curves correspond to the samples coated with ~4, ~10 and ~20 nm TiO_2, respectively.

References

1. Neubrech, F. *et al.* Resonances of individual metal nanowires in the infrared. *Appl. Phys. Lett.* **89,** 253104 (2006).
2. Huang, M. H. Room-Temperature Ultraviolet Nanowire Nanolasers. *Science (80-.).* **292,** 1897–1899 (2001).
3. Bergin, S. M. *et al.* The effect of nanowire length and diameter on the properties of transparent, conducting nanowire films. *Nanoscale* **4,** 1996 (2012).
4. Stichtenoth, D. *et al.* Optical size effects in ultrathin ZnO nanowires. *Nanotechnology* **18,** 435701 (2007).
5. Ng, H. T. *et al.* Optical properties of single-crystalline ZnO nanowires on m-sapphire. *Appl. Phys. Lett.* **82,** 2023 (2003).
6. Yang, P. *et al.* Controlled Growth of ZnO Nanowires and Their Optical Properties. *Adv. Funct. Mater.* **12,** 323 (2002).
7. Zhang, Z., Sun, X., Dresselhaus, M. S., Ying, J. Y. & Heremans, J. Electronic transport properties of single-crystal bismuth nanowire arrays. *Phys. Rev. B* **61,** 4850–4861 (2000).
8. Cornelius, T. W., Toimil-Molares, M. E., Neumann, R. & Karim, S. Finite-size effects in the electrical transport properties of single bismuth nanowires. *J. Appl. Phys.* **100,** 114307 (2006).
9. Durkan, C. & Welland, M. E. Size effects in the electrical resistivity of polycrystalline nanowires. *Phys. Rev. B* **61,** 14215–14218 (2000).
10. Huang, Q., Lilley, C. M., Bode, M. & Divan, R. Surface and size effects on the electrical properties of Cu nanowires. *J. Appl. Phys.* **104,** 023709 (2008).
11. Liu, Q. F., Gao, C. X., Xiao, J. J. & Xue, D. S. Size effects on magnetic properties in Fe 0.68 Ni 0.32 alloy nanowire arrays. *J. Magn. Magn. Mater.* **260,** 151–155 (2003).
12. Zhou, P. H. & Xue, D. S. Finite-size effect on magnetic properties in Prussian blue nanowire arrays. *J. Appl. Phys.* **96,** 610 (2004).
13. Wu, C., Yin, P., Zhu, X., OuYang, C. & Xie, Y. Synthesis of Hematite (α-Fe 2 O 3) Nanorods: Diameter-Size and Shape Effects on Their Applications in Magnetism, Lithium Ion Battery, and Gas Sensors. *J. Phys. Chem. B* **110,** 17806–17812 (2006).
14. Ren, Y., Liu, Q. F., Li, S. L., Wang, J. B. & Han, X. H. The effect of structure on magnetic properties of Co nanowire arrays. *J. Magn. Magn. Mater.* **321,** 226–230 (2009).
15. Katz, D. *et al.* Size-Dependent Tunneling and Optical Spectroscopy of CdSe Quantum Rods. *Phys. Rev. Lett.* **89,** 086801 (2002).
16. Ma, D. D. D. Small-Diameter Silicon Nanowire Surfaces. *Science (80-.).* **299,** 1874–1877 (2003).
17. Zhao, X., Wei, C. M., Yang, L. & Chou, M. Y. Quantum Confinement and Electronic Properties of Silicon Nanowires. *Phys. Rev. Lett.* **92,** 236805 (2004).
18. Toimil Molares, M. E., Balogh, A. G., Cornelius, T. W., Neumann, R. & Trautmann, C. Fragmentation of nanowires driven by Rayleigh instability. *Appl. Phys. Lett.* **85,** 5337 (2004).
19. Ponomareva, I., Srivastava, D. & Menon, M. Thermal Conductivity in Thin Silicon Nanowires: Phonon Confinement Effect. *Nano Lett.* **7,** 1155–1159 (2007).
20. Li, D. *et al.* Thermal conductivity of individual silicon nanowires. *Appl. Phys. Lett.* **83,** 2934 (2003).
21. Janotti, A. & Van de Walle, C. G. Fundamentals of zinc oxide as a semiconductor. *Reports Prog. Phys.* **72,** 126501 (2009).
22. Coleman, V. & Jagadish, C. in *Zinc Oxide Bulk, Thin Films and Nanostructures* 1–20 (Elsevier, 2006). doi:10.1016/B978-008044722-3/50001-4

23. Wang, Z. L. Zinc oxide nanostructures: growth, properties and applications. *J. Phys. Condens. Matter* **16,** R829–R858 (2004).

24. Bie, L.-J., Yan, X.-N., Yin, J., Duan, Y.-Q. & Yuan, Z.-H. Nanopillar ZnO gas sensor for hydrogen and ethanol. *Sensors Actuators B Chem.* **126,** 604–608 (2007).

25. Hsueh, T.-J., Hsu, C.-L., Chang, S.-J. & Chen, I.-C. Laterally grown ZnO nanowire ethanol gas sensors. *Sensors Actuators B Chem.* **126,** 473–477 (2007).

26. Wang, Z. L. & Song, J. Piezoelectric nanogenerators based on zinc oxide nanowire arrays. *Science* **312,** 242–6 (2006).

27. Xu, S. & Wang, Z. L. One-dimensional ZnO nanostructures: Solution growth and functional properties. *Nano Res.* **4,** 1013–1098 (2011).

28. Peng, Q. & Qin, Y. *Nanowires - Implementations and Applications*. (InTech, 2011). doi:10.5772/1025

29. Liu, M., Nam, C. Y., Black, C. T., Kamcev, J. & Zhang, L. Enhancing Water splitting activity and chemical stability of zinc oxide nanowire photoanodes with ultrathin titania shells. *J. Phys. Chem. C* **117,** 13396–13402 (2013).

30. Zhong, M., Ma, Y., Oleynikov, P., Domen, K. & Delaunay, J.-J. A conductive ZnO–ZnGaON nanowire-array-on-a-film photoanode for stable and efficient sunlight water splitting. *Energy Environ. Sci.* **7,** 1693 (2014).

31. Xia, Y. *et al.* One-Dimensional Nanostructures: Synthesis, Characterization, and Applications. *Adv. Mater.* **15,** 353–389 (2003).

32. Soci, C. *et al.* ZnO Nanowire UV Photodetectors with High Internal Gain. *Nano Lett.* **7,** 1003–1009 (2007).

33. Chen, M.-T. *et al.* Near UV LEDs made with in situ doped p-n homojunction ZnO nanowire arrays. *Nano Lett.* **10,** 4387–93 (2010).

34. Taheri, A., Saramad, S. & Setayeshi, S. ZnO nanowires in polycarbonate membrane as a high resolution X-ray detector (a Geant4 simulation). *Nucl. Instruments Methods Phys. Res. Sect. A Accel. Spectrometers, Detect. Assoc. Equip.* **716,** 15–22 (2013).

35. Ra, H.-W., Choi, K.-S., Kim, J.-H., Hahn, Y.-B. & Im, Y.-H. Fabrication of ZnO nanowires using nanoscale spacer lithography for gas sensors. *Small* **4,** 1105–9 (2008).

36. Weintraub, B., Deng, Y. & Wang, Z. L. Position-Controlled Seedless Growth of ZnO Nanorod Arrays on a Polymer Substrate via Wet Chemical Synthesis. *J. Phys. Chem. C* **111,** 10162–10165 (2007).

37. Lakshmi, B. B., Patrissi, C. J. & Martin, C. R. Sol−Gel Template Synthesis of Semiconductor Oxide Micro- and Nanostructures. *Chem. Mater.* **9,** 2544–2550 (1997).

38. Lee, W., Jeong, M.-C. & Myoung, J.-M. Catalyst-free growth of ZnO nanowires by metal-organic chemical vapour deposition (MOCVD) and thermal evaporation. *Acta Mater.* **52,** 3949–3957 (2004).

39. Khajavi, M. R., Blackwood, D. J., Cabanero, G. & Tena-Zaera, R. New insight into growth mechanism of ZnO nanowires electrodeposited from nitrate-based solutions. *Electrochim. Acta* **69,** 181–189 (2012).

40. Schönenberger, C. *et al.* Template Synthesis of Nanowires in Porous Polycarbonate Membranes: Electrochemistry and Morphology. *J. Phys. Chem. B* **101,** 5497–5505 (1997).

41. Hulteen, J. C. & Martin, C. R. A general template-based method for the preparation of nanomaterials. *J. Mater. Chem.* **7,** 1075–1087 (1997).

42. Possin, G. E. A Method for Forming Very Small Diameter Wires. *Rev. Sci. Instrum.* **41,** 772 (1970).

43. Toimil-Molares, M. E. Characterization and properties of micro- and nanowires of controlled

size, composition, and geometry fabricated by electrodeposition and ion-track technology. *Beilstein J. Nanotechnol.* **3,** 860–83 (2012).

44. Maria, B. *et al.* Single-Crystalline Copper Nanowires Produced Track Membranes **. **13,** 2001 (2001).

45. Pan, H. *et al.* Growth of single-crystalline Ni and Co nanowires via electrochemical deposition and their magnetic properties. *J. Phys. Chem. B* **109,** 3094–8 (2005).

46. Sima, M., Enculescu, I. & Vasile, E. Growth of ZnO micro and nanowires using the template method. *J. Optoelectron. Adv. Mater.* **8,** 825–828 (2006).

47. Ramirez, D., Pauporte, T., Gomez, H. & Lincot, D. Electrochemical growth of ZnO nanowires inside nanoporous alumina templates. A comparison with metallic Zn nanowires growth. *Phys. Status Solidi* **205,** 2371–2375 (2008).

48. V. Manzano, C. *et al.* ZnO Morphology Control by Pulsed Electrodeposition. *J. Phys. Chem. C* **117,** 1502–1508 (2013).

49. Zhou, J. *et al.* Three-Dimensional Tungsten Oxide Nanowire Networks. *Adv. Mater.* **17,** 2107–2110 (2005).

50. Ponzoni, A. *et al.* Ultrasensitive and highly selective gas sensors using three-dimensional tungsten oxide nanowire networks. *Appl. Phys. Lett.* **88,** 203101 (2006).

51. Gao, P. X., Lao, C. S., Hughes, W. L. & Wang, Z. L. Three-dimensional interconnected nanowire networks of ZnO. *Chem. Phys. Lett.* **408,** 174–178 (2005).

52. Wang, D. *et al.* A General Route to Macroscopic Hierarchical 3D Nanowire Networks. *Angew. Chemie Int. Ed.* **43,** 6169–6173 (2004).

53. Martín, J., Martín-González, M., Francisco Fernández, J. & Caballero-Calero, O. Ordered three-dimensional interconnected nanoarchitectures in anodic porous alumina. *Nat. Commun.* **5,** 5130 (2014).

54. Rauber, M. *et al.* Highly-Ordered Supportless Three-Dimensional Nanowire Networks with Tunable Complexity and Interwire Connectivity for Device Integration. *Nano Lett.* **11,** 2304–2310 (2011).

55. Movsesyan, L., Schubert, I., Yeranyan, L., Trautmann, C. & Eugenia Toimil-Molares, M. Influence of electrodeposition parameters on the structure and morphology of ZnO nanowire arrays and networks synthesized in etched ion-track membranes. *Semicond. Sci. Technol.* **31,** 014006 (2016).

56. Wagner, M. F. P., Völklein, F., Reith, H., Trautmann, C. & Toimil-Molares, M. E. Fabrication and thermoelectrical characterization of three-dimensional nanowire networks. *Phys. status solidi* **213,** 610–619 (2016).

57. Muench, F. *et al.* Self-Supporting Metal Nanotube Networks Obtained by Highly Conformal Electroless Plating. *Chempluschem* **80,** 1448–1456 (2015).

58. Spende, A. Surface modification of etched ion-track polymer membranes by atomic layer deposition. (Doctoral thesis, TU Darmstadt, 2016).

59. Muench, F. *et al.* Electrodeposition and electroless plating of hierarchical metal superstructures composed of 1D nano- and microscale building blocks. *Electrochim. Acta* **202,** 47–54 (2016).

60. van de Krol, R., Liang, Y. & Schoonman, J. Solar hydrogen production with nanostructured metal oxides. *J. Mater. Chem.* **18,** 2311 (2008).

61. Liu, M., Nam, C.-Y., Black, C. T., Kamcev, J. & Zhang, L. Enhancing Water Splitting Activity and Chemical Stability of Zinc Oxide Nanowire Photoanodes with Ultrathin Titania Shells. *J. Phys. Chem. C* **117,** 13396–13402 (2013).

62. Shi, J., Hara, Y., Sun, C., Anderson, M. A. & Wang, X. 3D High-Density Hierarchical Nanowire Architecture for High Performance Photoelectrochemical Electrodes 3D High-Density Hierarchical Nanowire Architecture for High Performance Photoelectrochemical

Electrodes. 3413–3419 (2011).

63. Wang, Y. C. *et al.* Fully Solar-Powered Photoelectrochemical Conversion for Simultaneous Energy Storage and Chemical Sensing. *Nano Lett.* **14,** 3668–3673 (2014).

64. Vignolini, S. *et al.* A 3D optical metamaterial made by self-assembly. *Adv. Mater.* **24,** 23–27 (2012).

65. Galisteo-López, J. F. *et al.* Self-Assembled Photonic Structures. *Adv. Mater.* **23,** 30–69 (2011).

66. Alenezi, M. R., Henley, S. J., Emerson, N. G. & Silva, S. R. P. From 1D and 2D ZnO nanostructures to 3D hierarchical structures with enhanced gas sensing properties. *Nanoscale* **6,** 235–47 (2014).

67. Liu, R., Duay, J. & Lee, S. B. Heterogeneous nanostructured electrode materials for electrochemical energy storage. *Chem. Commun.* **47,** 1384–404 (2011).

68. Duay, J., Gillette, E., Hu, J. & Lee, S. B. Controlled electrochemical deposition and transformation of hetero-nanoarchitectured electrodes for energy storage. *Phys. Chem. Chem. Phys.* **15,** 7976 (2013).

69. Wei, D. *et al.* A nanostructured electrochromic supercapacitor. *Nano Lett.* **12,** 1857–1862 (2012).

70. De Angelis, F. *et al.* 3D hollow nanostructures as building blocks for multifunctional plasmonics. *Nano Lett.* **13,** 3553–8 (2013).

71. Javey, A., Nam, S., Friedman, R. S., Yan, H. & Lieber, C. M. Layer-by-layer assembly of nanowires for three-dimensional, multifunctional electronics. *Nano Lett.* **7,** 773–7 (2007).

72. Fleischer, R. L., Price, P. B. & Walker, R. M. *Nuclear Tracks in Solids*. (Univ. of California Press, Berkeley, CA, 1975).

73. M. Nastasi, J. Mayer, J. K. H. Ion - solid interactions: Fundamentals and applications. *Cambridge Univ. Press* 1996 (1996).

74. Sun, Y. *et al.* Swift heavy ion induced amorphisation and chemical modification in polycarbonate. *Nucl. Instruments Methods Phys. Res. Sect. B Beam Interact. with Mater. Atoms* **209,** 188–193 (2003).

75. Dehaye, F., Balanzat, E., Ferain, E. & Legras, R. Chemical modifications induced in bisphenol A polycarbonate by swift heavy ions. *Nucl. Instruments Methods Phys. Res. Sect. B Beam Interact. with Mater. Atoms* **209,** 103–112 (2003).

76. Trautmann, C., Brüchle, W., Spohr, R., Vetter, J. & Angert, N. Pore geometry of etched ion tracks in polyimide. *Nucl. Instruments Methods Phys. Res. Sect. B Beam Interact. with Mater. Atoms* **111,** 70–74 (1996).

77. Trautmann, C., Bouffard, S. & Spohr, R. Etching threshold for ion tracks in polyimide. *Nucl. Instruments Methods Phys. Res. Sect. B Beam Interact. with Mater. Atoms* **116,** 429–433 (1996).

78. Spohr, R. *Ion tracks and microtechnology*. (Friedr. Vieweg & Sohn Verlagsgesellschaft, 1990).

79. Ferain, E. & Legras, R. Heavy ion tracks in polycarbonate. Comparison with a heavy ion irradiated model compound (diphenyl carbonate). *Nucl. Instruments Methods Phys. Res. Sect. B Beam Interact. with Mater. Atoms* **82,** 539–548 (1993).

80. Cornelius, T. W. *et al.* Nanopores in track-etched polymer membranes characterized by small-angle x-ray scattering. *Nanotechnology* **21,** 155702 (2010).

81. Movsesyan, L. & Olbromska, B. Influence of The UV Exposure Time on The Fabrication of Etched Membranes. *GSI Summer Student Progr. Rep. B.* (2010).

82. Maijenburg, A. W. *et al.* Electrodeposition of micropatterned Ni|Pt multilayers and segmented Ni|Pt|Ni nanowires. *Electrochim. Acta* **81,** 123–128 (2012).

83. Schubert, I., Burr, L., Trautmann, C. & Toimil-Molares, M. E. Growth and morphological

analysis of segmented AuAg alloy nanowires created by pulsed electrodeposition in ion-track etched membranes. *Beilstein J. Nanotechnol.* **6,** 1272–1280 (2015).

84. Burr, L., Schubert, I., Sigle, W., Trautmann, C. & Toimil-Molares, M. E. Surface Enrichment in Au-Ag Alloy Nanowires and Investigation of the Dealloying Process. *J. Phys. Chem. C* **119,** 20949–20956 (2015).

85. Paunovic, M. & Schlesinger, M. Fundamentals of Electrochemical Deposition. *John Wiley Sons, Inc.*

86. Bates, R. G. & Macaskill, J. B. Standard potential of the silver-silver chloride electrode. *Pure Appl. Chem.* **50,** 1701–1706 (1978).

87. I. U. Schuchert, M. E. Toimil Molares, D. Dobrev, J. Vetter, R. Neumann, M. M. Electrochemical Copper Deposition in Etched Ion Track Membranes. *J. Electrochem. Soc.* **150,** C189–C194 (2003).

88. Xu, S., Lao, C., Weintraub, B. & Wang, Z. L. Density-controlled growth of aligned ZnO nanowire arrays by seedless chemical approach on smooth surfaces. *J. Mater. Res.* **23,** 2072–2077 (2011).

89. Vernardou, D. *et al.* pH effect on the morphology of ZnO nanostructures grown with aqueous chemical growth. *Thin Solid Films* **515,** 8764–8767 (2007).

90. Wahab, R., Kim, Y.-S. & Shin, H.-S. Synthesis, Characterization and Effect of pH Variation on Zinc Oxide Nanostructures. *Mater. Trans.* **50,** 2092–2097 (2009).

91. Lee, Y. *et al.* Tunable Arrays of ZnO Nanorods and Nanoneedles via Seed Layer and Solution Chemistry & DESIGN 2008. (2008).

92. Dodson, E. M. & Savage, J. A. Vapour growth of single-crystal zinc oxide. *J. Mater. Sci.* **3,** 19–25 (1968).

93. Helbig, R. Über die züchtung von grösseren reinen und dotierten ZnO-kristallen aus der gasphase. *J. Cryst. Growth* **15,** 25–31 (1972).

94. Klingshirn, C. F., Meyer, B. K., Waag, A., Hoffmann, A. & Geurts, J. *Zinc Oxide*. *Springer Series in Materials Science* **120,** (Springer Berlin Heidelberg, 2010).

95. Ivanov, I. & Pollman, J. First surface electronic structure of a wurtzite-type semiconductor the polar and nonpolar surfaces of ZnO. *Solid State Commun.* **36,** 361–364 (1980).

96. Laudise, R. A. & Ballman, A. A. HYDROTHERMAL SYNTHESIS OF ZINC OXIDE AND ZINC SULFIDE 1. *J. Phys. Chem.* **64,** 688–691 (1960).

97. Rössler, U. Energy Bands of Hexagonal II-VI Semiconductors. *Phys. Rev.* **184,** 733–738 (1969).

98. Chelikowsky, J. R. An oxygen pseudopotential: Application to the electronic structure of ZnO. *Solid State Commun.* **22,** 351–354 (1977).

99. Zwicker, G. & Jacobi, K. Experimental band structure of ZnO. *Solid State Commun.* **54,** 701–704 (1985).

100. Girard, R. T. *et al.* Electronic structure of ZnO(0001) studied by angle-resolved photoelectron spectroscopy. *Surf. Sci.* **373,** 409–417 (1997).

101. Look, D. C. *et al.* Electrical properties of bulk ZnO. *Solid State Commun.* **105,** 399–401 (1998).

102. Tsukazaki, A. *et al.* Quantum Hall Effect in Polar Oxide Heterostructures. *Science (80-.).* **315,** 1388–1391 (2007).

103. Meyer, J. *et al.* Indium-free transparent organic light emitting diodes with Al doped ZnO electrodes grown by atomic layer and pulsed laser deposition. *Appl. Phys. Lett.* **93,** 073308 (2008).

104. Yang, Z., Look, D. C. & Liu, J. L. Ga-related photoluminescence lines in Ga-doped ZnO

grown by plasma-assisted molecular-beam epitaxy. *Appl. Phys. Lett.* **94,** 072101 (2009).

105. Look, D. C., Claflin, B. & Smith, H. E. Origin of conductive surface layer in annealed ZnO. *Appl. Phys. Lett.* **92,** 122108 (2008).

106. Vaithianathan, V., Moon, J. H., Chang, C.-H., Asokan, K. & Kim, S. S. Electronic Structure of P-Doped ZnO Films with p-Type Conductivity. *J. Nanosci. Nanotechnol.* **6,** 3422–3425 (2006).

107. Chavillon, B. *et al.* P-Type Nitrogen-Doped ZnO Nanoparticles Stable under Ambient Conditions. *J. Am. Chem. Soc.* **134,** 464–470 (2012).

108. Wang, Z., Yue, Y. & Cao, Y. Preparation and properties of nitrogen doped p-type zinc oxide films by reactive magnetron sputtering. *Vacuum* **101,** 313–316 (2014).

109. Fujishima, a & Honda, K. Electrochemical photolysis of water at a semiconductor electrode. *Nature* **238,** 37–38 (1972).

110. Abdi, F. F. *et al.* Efficient solar water splitting by enhanced charge separation in a bismuth vanadate-silicon tandem photoelectrode. *Nat. Commun.* **4,** 2195 (2013).

111. Bornoz, P. *et al.* A bismuth vanadate-cuprous oxide tandem cell for overall solar water splitting. *J. Phys. Chem. C* **118,** 16959–16966 (2014).

112. Yang, J., Wang, D., Han, H. & Li, C. Roles of cocatalysts in photocatalysis and photoelectrocatalysis. *Acc. Chem. Res.* **46,** 1900–1909 (2013).

113. Walter, M. G. *et al.* Solar Water Splitting Cells. *Chem. Rev.* **110,** 6446–6473 (2010).

114. Kudo, A. & Miseki, Y. Heterogeneous photocatalyst materials for water splitting. *Chem. Soc. Rev.* **38,** 253–278 (2009).

115. Hwang, Y. J., Boukai, A. & Yang, P. High Density n-Si/n-TiO 2 Core/Shell Nanowire Arrays with Enhanced Photoactivity. *Nano Lett.* **9,** 410–415 (2009).

116. Hong, S. J., Lee, S., Jang, J. S. & Lee, J. S. Heterojunction BiVO4/WO3 electrodes for enhanced photoactivity of water oxidation. *Energy Environ. Sci.* **4,** 1781 (2011).

117. Luo, J. *et al.* Cu 2 O Nanowire Photocathodes for Efficient and Durable Solar Water Splitting. *Nano Lett.* **16,** 1848–1857 (2016).

118. Lewerenz, H.-J. & Peter, L. *Photoelectrochemical Water Splitting*. (Royal Society of Chemistry, 2013). doi:10.1039/9781849737739

119. Grätzel, M. Photoelectrochemical cells. *Nature* **414,** 338–344 (2001).

120. Schoonman, J. & Krol, R. Van De. Nanostructured Materials for Solar Hydrogen Production *. *U.P.B. Sci. Bull* **73,** 31–44 (2011).

121. Kayes, B. M., Atwater, H. A. & Lewis, N. S. Comparison of the device physics principles of planar and radial p-n junction nanorod solar cells. *J. Appl. Phys.* **97,** 114302 (2005).

122. Hochbaum, A. I. & Yang, P. Semiconductor Nanowires for Energy Conversion. *Chem. Rev.* **110,** 527–546 (2010).

123. Lopatiuk, O., Chernyak, L., Osinsky, A., Xie, J. Q. & Chow, P. P. Electron-beam-induced current and cathodoluminescence studies of thermally activated increase for carrier diffusion length and lifetime in n-type ZnO. *Appl. Phys. Lett.* **87,** 162103 (2005).

124. Bjoerksten, U., Moser, J. & Graetzel, M. Photoelectrochemical Studies on Nanocrystalline Hematite Films. *Chem. Mater.* **6,** 858–863 (1994).

125. Kislov, N. *et al.* Photocatalytic Degradation of Methyl Orange over Single Crystalline ZnO: Orientation Dependence of Photoactivity and Photostability of ZnO. *Langmuir* **25,** 3310–3315 (2009).

126. Inoue, T., Fujishima, A. & Honda, K. Competitive redox reactions at the ZnO semiconductor photoelectrode. *Bull. Chem. Soc. Jpn.* **52,** 3217–3220 (1979).

127. Bonch-Bruevich, V. L. & Kalashnikov, S. G. Fizika Poluprovodnikov (Semiconductor

Physics). (Nauka, Moscow, 1977).

128. Burr, L. Ion-track technology based synthesis and characterization of gold and gold alloys nanowires and nanocones. (Doctoral thesis, TU Darmstadt, 2016).

129. Ferain, E. & Legras, R. Track-etched membrane: dynamics of pore formation. *Nucl. Inst. Methods Phys. Res. B* **84,** 331–336 (1994).

130. Manzano, C. V., Alegre, D., Caballero-Calero, O., Alén, B. & Martín-González, M. S. Synthesis and luminescence properties of electrodeposited ZnO films. *J. Appl. Phys.* **110,** 043538 (2011).

131. Maas, M. G., Rodijk, E. J. B., Wouter Maijenburg, a., Blank, D. H. a. & ten Elshof, J. E. Microstructure development in zinc oxide nanowires and iron oxohydroxide nanotubes by cathodic electrodeposition in nanopores. *J. Mater. Res.* **26,** 2261–2267 (2011).

132. Kayaci, F. *et al.* Selective isolation of the electron or hole in photocatalysis: ZnO–TiO2 and TiO2–ZnO core–shell structured heterojunction nanofibers via electrospinning and atomic layer deposition. *Nanoscale* **6,** 5735 (2014).

133. Law, M. *et al.* ZnO−Al 2 O 3 and ZnO−TiO 2 Core−Shell Nanowire Dye-Sensitized Solar Cells. *J. Phys. Chem. B* **110,** 22652–22663 (2006).

134. Irannejad, A. *et al.* Effect of the TiO2 shell thickness on the dye-sensitized solar cells with ZnO–TiO2 core–shell nanorod electrodes. *Electrochim. Acta* **58,** 19–24 (2011).

135. Fu, S., Lim, C. S., Kwek, L. C. & Chia, T. C. ZnO / TiO 2 Core-Shell Quantum Dots Application for Colorectal Cancer Fluorescence Image. *Pharm. Eng.* 377–380 (2006).

136. Wang, J. X. *et al.* Zinc oxide nanocomb biosensor for glucose detection. *Appl. Phys. Lett.* **88,** 233106 (2006).

137. Yılmaz, S. *et al.* Effects of Cu diffusion-doping on structural, optical, and magnetic properties of ZnO nanorod arrays grown by vapor phase transport method. *J. Appl. Phys.* **111,** 013903 (2012).

138. Allabergenov, B. *et al.* Microstructural analysis and optical characteristics of Cu-doped ZnO thin films prepared by DC magnetron sputtering. *J. Cryst. Growth* **401,** 573–576 (2014).

139. Herklotz, F., Lavrov, E. V. & Weber, J. On diffusion of Cu in ZnO. *Phys. B Condens. Matter* **404,** 4807–4809 (2009).

140. Hu, L., Zhu, L., He, H., Zhang, L. & Ye, Z. Acceptor defect-participating magnetic exchange in ZnO : Cu nanocrystalline film: defect structure evolution, Cu–N synergetic role and magnetic control. *J. Mater. Chem. C* **3,** 1330–1346 (2015).

141. Aarik, J., Aidla, A., Uustare, T., Ritala, M. & Leskelä, M. Titanium isopropoxide as a precursor for atomic layer deposition: characterization of titanium dioxide growth process. *Appl. Surf. Sci.* **161,** 385–395 (2000).

142. Schwarz, C., Chernyak, L. & Flitsiyan, E. Cathodoluminescence Studies of Electron Injection Effects in Wide-Band-Gap Semiconductors. 3–31

143. Fan, J. *et al.* Solution-growth and optoelectronic performance of ZnO : Cl/TiO 2 and ZnO : Cl/Zn x TiO y /TiO 2 core–shell nanowires with tunable shell thickness. *J. Phys. D. Appl. Phys.* **45,** 415301 (2012).

144. Zhao, L. *et al.* Structure and Photocatalysis of TiO2/ZnO Double-Layer Film Prepared by Pulsed Laser Deposition. *Mater. Trans.* **53,** 463–468 (2012).

145. Cheng, C. *et al.* Enhanced photocatalytic performance of TiO2-ZnO hybrid nanostructures. *Sci. Rep.* **4,** 4181 (2014).

146. LaRue, J. L. *et al.* The work function of submonolayer cesium-covered gold: a photoelectron spectroscopy study. *J. Chem. Phys.* **129,** 024709 (2008).

Acknowledgments

"Gratitude is not only the greatest of virtues, but the parent of all others."

Cicero

This thesis would not have been possible without the great support and help of my supervisors, colleagues, collaborators, friends and my dear family.

First and foremost, I would like to express my deepest gratitude to my supervisor, Prof. Dr. Christina Trautmann. Thank you for giving me an opportunity to work at the Materials Research department of GSI and gain precious experience in experimental science. I am also very thankful to my scientific adviser, Dr. Maria Eugenia Toimil-Molares. Many thanks for helping me to get the scholarship to conduct my PhD studies in Germany. I highly appreciate the aid and guidance of both of you throughout all the stages of my studies and your instant feedback to my questions and thesis when it was urgent. Next to your scientific assistance, giving a freedom to make decisions, networking and realization of ideas is highly appreciated. Your assistance and encouragement to attend so many conferences are priceless. I am also infinitely grateful to both of you for your care, moral support, and inspiration every time I was in great need of them.

I would like to thank Prof. Dr. Wolfram Jaegermann, Prof. Dr. Wolfgang Ensinger and Prof. Dr. Christian Hess who expressed kindness and readiness to be members of my PhD committee. Special thanks go to Prof. Dr. Wolfram Jaegermann and PD Dr. Bernhard Kaiser for their helpful discussions and advice on the photoelectrochemical measurements during HGS-HIRe graduate school meetings. Also many thanks for providing me with the opportunity to perform XPS and PEC measurements in your labs.

I express my sincere appreciation to Dr. A. Wouter Maijenburg and Dr. Florent Yang for their splendid help with PEC and XPS measurements and valuable discussions. I gained a huge bag of knowledge from you both and I hope very much to have more chances to work and share my experience with you.

The chance I got to perform my first PEC measurements in the University of Twente is also highly appreciated. I wish to thank Prof. Dr. Guido Mul for the chance to work in his group for one week, Dr. A. Wouter Maijenburg for being the "bridge" between Darmstadt and Twente, and finally Lidy Harryvan for taking care of the bureaucracy for my stay in the Netherlands. Hartelijk dank!

My special gratitude goes to Dr. Wilfried Sigle from Max Planck Institute for Solid State Research in Stuttgart for HRTEM, HAADF and EELS measurements. Thanks for your quick

feedback and helpful hints on analyses of the data. I would also like to thank Dr. Joachim Brötz for helping me with XRD measurements at the TU Darmstadt.

I am very much indebted to Janina Krieg, the best officemate and the most unique person I know. Thanks a lot for helping me to adapt to the new lifestyle in Germany, be more self-confident in communicating in German, and see things from different perspectives. It was also my pleasure to share the fumehood in the chemistry lab with you and to have long-lasting scientific discussions from all fields of physics. Shortly said, *there are no words* to express how thankful I am to you (you know what I mean, right? ☺).

Je ne parle *pas* français, but I will not miss the chance to thank my very good friend and colleague Dr. Loïc Burr. I had the luck to know you for the whole period of my PhD. Thanks for sharing your experience and ideas about electrodeposition, synthesis of nanocones, and many other topics. I am certainly grateful to you for introducing me to the French delicious cuisine. Merci!

I am also thankful to Anne Spende with whom I had interesting discussions about ALD. Thanks a lot for taking such a good care of the ALD machine and sharing your experience with me.

Also, many thanks to Dr. A. Wouter Maijenburg, Dr. Florent Yang, Janina Krieg, Anne Spende and Michael Wagner who gave me valuable suggestions for improvement of my thesis. Sincere thanks to Dr. Marco Cassinelli, with the help of your trust in me, moral support and encouragements I was able to deal with any complicated situation, I am really grateful to you!

"Healthy and muscular" thanks to Anton Romanenko and Dr. Christian Hubert for involving me in a more sportive and healthier lifestyle. "*Life has its ups and downs…We call them squats*" ☺. Thank you and also Katharina Kupka for introducing the experiments at the M-branch to me during the nightshifts.

I would also like to thank Dimitri Khaghani with whom I worked on a joint project and had interesting scientific, as well as political discussions.

Many thanks to all my colleagues from the Materials Research group of the GSI for providing the nice working atmosphere, friendly communication and readiness to help any time. I would like to thank especially all those who shared with me the beam-time shifts at X0-hall, especially during the long and tiring night shifts.

I wish to thank the students who worked on projects related to my work: Lilit Yeranyan, Noel Goethals and Merin Jissy Joseph. It was my pleasure to share entertaining activities with Raquel Thomas, Leandro Gutierrez, Peter Katrik, Vladimir Lavrik, Olena Lenchuk, Gonzalo Perez Mitta, and Yaiza Montana Gonzalez. Special thanks to my friends from Armenia who

did not stop believing in me and always encouraged me to move on with more self-confidence. Շնորհակալ եմ իմ բոլոր ընկերներին, ովքեր շարունակաբար իմ մեջ ուժ ու հավատ էին ներշնչում և միշտ քաջալերում էին շարժվել առաջ ու ոչ մի դեպքում չհանձնվել:

Very special thanks go to my German teachers, Fr. Miskaryan *jan* and Jutta. Dank der Fähigkeit Deutsch zu sprechen, habe ich mich an Deutschland und die Menschen leicht angepasst. Vielen Dank, meine liebe Lehrerinnen!

I express my sincere gratitude to Beilstein Institute for the Advancement of Chemical Sciences (Frankfurt) for financial and educational support. Additionally, I would like to thank HGS-HIRe graduate school for the financial support to attend inland and international conferences, as well as for very useful soft-skill courses. The instructions by Emma Ford and Dr. Steve Hutchinson are highly valued. The support from DFG FOR 1583 and DFG SPP 1613 projects providing me with financial means to complete my thesis is assessed.

Last but not least, I want to thank my family for their continuous inspiration, love and care, which always help me to overcome the obstacles I face in my life. Իմ թանակագին ընտանիք, շատ շնորհակալ եմ, որ միշտ ամուր կանգնած եք իմ կողքին: Ձեր սիրով ու հոգատարությամբ ինձ միշտ ոգեշնչում եք, օգնում հաղթահարել իմ առջև խոյացած ցանկացած արգելք: Մամ ջան, անչափ երախտապարտ եմ, որ միշտ իմ մասին մտածում ես ու հոգ ես տանում: Քո՝ հոգեպես կողքիս լինելը հատկապես վերջին 7 ամիսների ընթացքում ինձ համար անասելի մեծ աջակցություն էր: Պապ ջան, շնորհակալ եմ, որ միշտ հավատացել ես ու շարունակում ես հավատալ իմ ուժերին: Ինչպես դու ես ասում ՛՛մենք դա կարող ենք՛՛: Շնորհակալ եմ ոգեշնչելու համար: Աշխարհի ամենալավ քուրիկներ, Ալինա և Աննա, ձեր վայրկենական աջակցությունը և խորհուրդները ցանկացած հարցում ինձ միշտ ուղղորդում են դեպի ճիշտ ընտրություն: Ձեր նման ավագ քույրեր ունենալը մեծ պարգև է, շնորհակալ եմ ինձ ճիշտ օրինակ ծառայելու համար:

Curriculum Vitae - Liana Movsesyan

Education

2012 - 2016 **Technische Universität Darmstadt**, Darmstadt, Germany
GSI Helmholtz Center for Heavy Ion Research, Darmstadt, Germany
Dissertation
Topic: "Template-assisted growth and characterization of ZnO-based nanowire arrays and 3D networks"
Research Supervisor: Prof. Dr. Christina Trautmann
Research Mentor: Dr. Maria Eugenia Toimil-Molares
External Supervisor: Prof. Dr. Wolfram Jaegermann

2010 - 2012 **Yerevan State University**, Yerevan, Armenia
Master degree of Physics: Physics of Semiconductors and Microelectronics
Diploma with honors
Topic: "Investigation of Si-Ge-C quantum dots-nanopits nucleation mechanism"
Research Supervisor: Prof. Dr. Karen Gambaryan

2006 - 2010 **Yerevan State University**, Yerevan, Armenia
Bachelor degree of Physics: Physics of Semiconductors and Microelectronics
Diploma with honors
Topic: "Nucleation of $Si_{1-x}Ge_x$ quantum dots and island-pits pairs on Si(100) substrate"
Research Supervisor: Prof. Dr. Karen Gambaryan

2004 - 2006 **"Ohanyan" High School-college**, Yerevan, Armenia
Emphasis: Physics, Mathematics
Certificate with honors

1996 - 2004 "**N102" secondary school**, Yerevan, Armenia
Certificate with honors

Awards

2015 **Giersch-excellence-grant 2015**, Stiftung Giersch in cooperation with HGS-HIRe graduate school, Germany

2012 - 2015 **Doctoral Scholarship**, Beilstein Institute for the Advancement of Chemical Sciences, Gemrany

2012 **NIM Student Research Award,** Nanosystem Initiative Munich, Germany

2009 - 2012	**Nominal Scholarship** named after Yuri Bakhshyan, Yerevan State University, Armenia
2007 - 2012	**Excellence Scholarship** of Yerevan State University, Yerevan State University, Armenia

Published works

2015	**L. Movsesyan**, I. Schubert, L. Yeranyan, C. Trautmann, M.E. Toimil-Molares, "Influence of electrodeposition parameters on the structure and morphology of ZnO nanowire arrays and networks synthesized in etched ion-track membranes", *Semicond. Sci. Technol*., 31(1), 2015, 14006.
	L. Movsesyan, A.W. Maijenburg, G. Mul, W. Sigle, C. Trautmann, M.E. Toimil-Molares, "Synthesis and application of ZnO nanowire-based 3D networks for enhanced phototelectrochemical water splitting", *GSI Scientific report 2015*.
	A. Ivanova, M.C. Fravventura, D. Fattakhova-Rohlfing, J. Rathousky, **L. Movsesyan**, P. Ganter, T.J. Savenije, T. Bein, "Nanocellulose-templated porous titania scaffolds incorporating presynthesized titania nanocrystals", *Chem. Mater.*, 27(18), 2015, 6205-6212.
2014	A.W. Maijenburg, **L. Movsesyan**, C. Trautmann, M.E. Toimil-Molares, "Metal-organic frameworks shaped into one-dimensional nanostructures via templated electrodeposition", *GSI Scientific report 2014*, DOI:10.15120/GR-2015-1-APPA-MML-MR-18.
2012	**L. Movsesyan** and B. Olbromska, "Influence of the UV exposure time on the fabrication of etched membranes", *GSI Summer Student Program Report Book*, 2010.
2010	K. Gambaryan, V. Aroutiounian, A. Simonyan, **L. Movsesyan**, "Growth features at competing nucleation of quantum dots and nanopits in Si-Ge-C ternary system", *Journal of Contemporary Physics*, 47(4), 2012, 173-180.

Contributions to conferences and workshops

2016	**Oral presentation:** *Three-dimensional ZnO and p-Cu_2O nanowire networks for efficient photoelectrochemical water splitting*; IPS-21, Sankt Petersburg, Russia
2015	**Oral presentation:** *Three-dimensional ZnO nanowire networks fabricated by electrodeposition in etched ion-track membranes as model systems for photoelectrochemical applications*; EDNANO11, Balatonfüred, Hungary

Oral presentation: *Three-dimensional ZnO/TiO_2 core/shell nanowire networks fabricated by ion-track technology*; Ionenstrahlen und Nanostrukturen, Heidelberg, Germany

Poster presentation: *Synthesis and characterization of ZnO/TiO_2 nanostructured photo-electrodes by electrodeposition in etched ion-track templates*; SHIM 2015, Darmstadt, Germany (co-organizer)

Oral presentation: *Three dimensional semiconductor nanowire networks for integration into solar energy devices*; eMRS Spring Meeting 2015, Symposium A, Lille, France

Oral presentation: *Photo-electrochemical characterization of functional ZnO/TiO_2 core-shell nanowire networks electrodeposited in etched ion-track membranes*; eMRS Spring Meeting 2015, Symposium A, Lille, France

2014 **Oral presentation:** *Electrodeposition of ZnO nanowires in etched ion-track membranes and their integration into 3D assemblies for photovoltaic and optoelectronic devices*; MSE 2014, Darmstadt, Germany

Poster presentation: *Zinc oxide nanowires and 3D nanowire networks fabricated by ion-track technology and electrodeposition*; SNI2014, Bonn, Germany

Poster presentation: *ZnO 3D nanowire networks fabricated by ion-track technology and electrodeposition*; CECAM2014, Bremen, Germany

Poster presentation: *Fabrication of ZnO semiconductor nanowire arrays and 3D networks by electrodeposition in etched ion track templates*; MRS Spring Meeting and Exhibit 2014, San Francisco, USA

Oral presentation: *Fabrication of ZnO semiconductor nanowire arrays and 3D networks by electrodeposition in etched ion track templates*; EDNANO10, Oberwessel, Germany (co-organizer)

2013 **Poster presentation:** *Size and density tuning of 3D nanowire networks fabricated by electrodeposition*; Solar Fuel 13, Granada, Spain

Research and supervision

2013 - 2016 **Supervision** of an internship and bachelor thesis, "Photo-electrochemical water splitting and XPS analysis of ZnO and ZnO/TiO_2 nanowire networks with different height and density", GSI and Technische Hochschule Mittelhessen, Germany

Supervision of an internship student, "Optimization of etched ion-track membranes for electrodeposition of ZnO nanowire networks", GSI and TU Darmstadt, Germany

Supervision of a summer student, GSI summer student program 2014, "Characterization of ZnO nanowires fabricated in etched ion-track membranes by electrochemical deposition", GSI, Germany

Supervision of an internship student, "Synthesis of Cu and n-Cu_2O nanowires in etched ion-track membranes", GSI and TU Darmstadt, Germany

2012 **5th International Summer Research Program, NIM,** Munich, Germany

Topic: "Biotemplated mesoporous titania films for photovoltaic applications"

Research Mentor: Dr. Alesja Ivanova

2010 **GSI International Summer Student Program 2010**, Darmstadt, Germany

Topic: "Influence of the UV exposure time on the fabrication of etched membranes"

Research Mentor: Dr. Maria Eugenia Toimil-Molares

2010 **"Electronic Design and Testing" training**, YSU - Virage Logic Corporation, Yerevan, Armenia

“Science as Art” gallery